Scattering and Dissociation of Simple Molecules at Surfaces

Dissertation
zur Erlangung des Grades
eines Doktors der Naturwissenschaft

vorgelegt von
Karsten Brüning

Universität Osnabrück

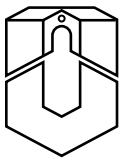

Osnabrück, Juni 2000

Contents

Introduction

Dissociation dynamics of molecules at surfaces play a crucial role in a variety of fields such as heterogeneous catalysis, environmental chemistry, modification of materials, and erosion of space vehicles. Not only in surface physics, but also for fusion research, the interaction of charged and neutral particles with condensed matter is of interest [1].

For the investigations of this work, simple molecules are used to explore the mechanisms of dissociation during the scattering off metal surfaces. Apart from the noble gas atoms which sometimes are also called molecules, the simplest molecule is without any doubt the diatomic hydrogen – the only molecule which can still be described exactly in quantum mechanics. Despite of the simplicity of its structure in gas phase, its interaction with metal surfaces is already as complex as for heavier molecules containing more electrons. Nevertheless, hydrogen systems have received considerable attention in the last decades not least because it is one of the most important reactant or product molecule in the field of heterogeneous catalysis.

A second representative of 'simple molecules' is the most available one in the atmosphere of the earth, namely nitrogen. An outstanding property of N_2, making it an interesting candidate for this work, is its chemical inactivity in surface processes as occurring in adsorption or scattering experiments.

The use of grazing scattering at kinetic energies in the keV range enables us to model the process of particle-surface interaction in the low energy region, which is important for examining physical and chemical problems such as adsorption, heterogenous catalysis, etc. At small glancing angles, the range of 'perpendicular energies' (the energy which is associated with the perpendicular component of the projectile velocity) below 10 eV is achieved, being typical for the activation of chemical reactions on a surface. This approach is predestined for simple molecules such as hydrogen and nitrogen, since the usual technique of supersonic nozzles is applicable only for obtaining heavy hyperthermal molecules [2].

For molecules with translational energies in the range of 10^2 to 10^4 eV, different dissociation mechanisms have been proposed [3], e.g. dissociation following resonant neutralization of their positively charged ions into antibonding molecular states and purely impulsive dissociation by momentum transfer.
In contrast to molecules such as H_2 or O_2, charge transfer processes during the interaction of N_2 with metal surfaces are of minor importance for the dissociation process [4, 5, 6]; even though to a small extent electronical excitation due to violent collisions with surface atoms is possible [7].

It is well known that the orientation of the molecule during the interaction with the surface is of considerable importance for several types of interaction processes at hyperthermal energies [8, 9] as well as in the keV regime [10].
Furthermore, it has been found that the fragmentation of grazing scattered molecules strongly depends on the azimuthal orientation of the surface with respect to the particle beam [11, 12, 13].
Recent investigations on H_2^+ and N_2^+ scattered off the (111)- and (110)-faces of palladium under grazing incidence show in this context that for scattering along a high-indexed azimuthal direction, mainly vibrational excitation occurs, whereas for low-index incidence, the rotational excitation is the predominant reason for dissociation [11, 14].

This thesis represents an extensive study of the dissociative scattering of N_2 and H_2 molecules from palladium, silver, and platinum surfaces. The chosen (110)-surfaces of these face centered cubic (fcc) crystals provide semichannels of different structure and width; thus it is expected to find a clear dependence on the azimuthal scattering angle.

The aim of this work is to contribute to the understanding of the fundamental but still controversially discussed physical processes taking place in the course of scattering from surfaces. The experimental part of this study is based on energy and azimuth dependent time-of-flight measurements. The energetic distribution of the scattering products is analyzed in order to reveal information about the mechanism(s) of dissociation. In this connection, clear differences in the scattering of nitrogen and hydrogen are expected.

Using molecular dynamics calculations, the interaction in the scattering process is simulated by following in the footsteps of previous investigations [11, 15, 16]. The direct comparison of experimental and simulational results will provide a conclusive insight into the processes taking place at the surface.

Still an open question in the field of molecule-surface interactions is the role of mutual screening of the molecular constituents through the free metal electron gas in the dissociation process. Due to its nonadiabatic character for systems with fast moving

molecules, the term *dynamic* screening [17, 18] is justified. This work intends to examine in how far the dissociation is affected due to the dissolution of the intramolecular bond [19].

Chapter 1

Theory

This chapter introduces the theoretical background which is necessary for the understanding of the present work on the interaction between molecules and surfaces. In particular, regarding the current state of knowledge, the basic mechanic and electronic processes occurring near the surface are explained. In the course of this thesis, these fundamentals will be useful and are thus collectively presented here.

1.1 The Scattering Process

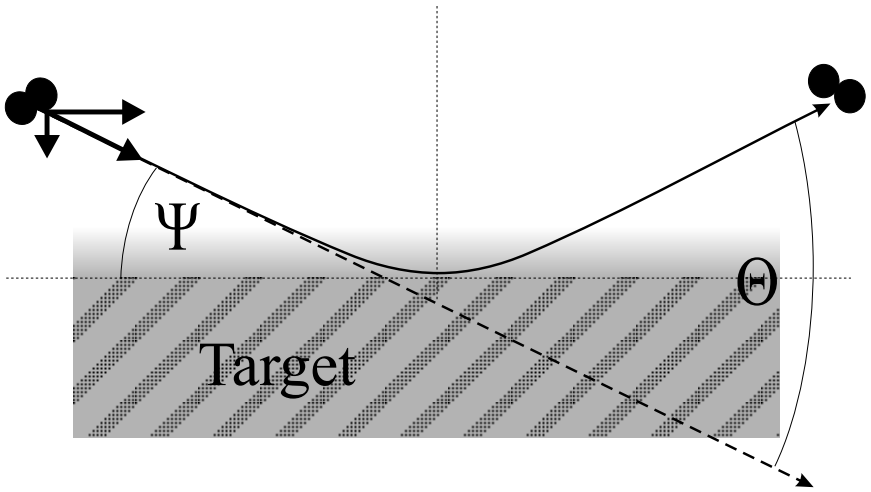

Figure 1.1: Scattering geometry. The molecular particle is scattered under grazing incidence (glancing angle $\Psi = \Theta/2$). While 'diving' into the electron sea of the target surface, it is subject to various interaction processes of both, elastic and inelastic nature.

Atomic and molecular ion scattering from metallic surfaces is affected by elastic as well as inelastic interaction processes. The elastic interaction is quite easy to understand, since the underlying physics can be treated in a classical way: all particles which are

involved obey Newton's laws and the conservation of energy and momentum. Several analytical methods – some of them also used in this work – are based on these elastic effects. As applications, surely Ion Scattering Spectroscopy (ISS) [20, 21, 22], Ion Desorption Spectrometry (IDS) [23, 24], and Impact Collision Ion Scattering Spectroscopy (ICISS) [25] have to be mentioned, and, last but not least, the preparation of the samples itself by sputtering (see Section 2.3).
All these methods involve atomic ions. However, the main interest in this work is the scattering of simple diatomic molecules, namely hydrogen and nitrogen. In this case, energy is not only transferred from the impinging projectile to surface atoms, but also to a certain extend from the molecule's center-of-mass (C.O.M.) system into its internal degrees of freedom. As a result, the molecules are vibrationally and/or rotationally excited – or even dissociated. Thus the mechanical interaction between a molecule (or, to be more precisely: its constituents) and the target can be one dissociation channel. In this work, the scattering geometry is chosen to provide grazing incidence, i.e., the total scattering angles range from $0° \ldots 10°$. Hence, even for hyperthermal energies ranging from $200 \ldots 4000$ eV, the kinetic energy $E_\perp$ which is associated with the perpendicular component of the velocity, $E_\perp = E_0 \sin^2 \Psi$ (E_0 is the initial kinetic energy of the molecule and Ψ the glancing angle of incidence), is not sufficient for an instantaneous decay. Nevertheless, assuming a realistic atomic corrugation of the target surface, energy may also be transferred from the parallel component.

More complicated than elastic interactions are the electronic processes which occur during the molecular ion-surface interaction. These include charge exchange processes such as the initial neutralization, as well as subsequent re-ionization processes, excitation of electron-hole pairs, and screening effects due to delocalized metal electrons. These electronic effects can cause dissociation as well.
A detailed description of the processes that are relevant for this work is given in the following.

1.1.1 Elastic Collisions

For a binary collision of two atomic particles, as schematically illustrated in Fig. 1.2a, the following equation results from the conservation of energy and momentum [20]:

$$E = E_0 \left(\frac{M_1}{M_1 + M_2} \right)^2 \left(\cos\Theta + \sqrt{\left(\frac{M_2}{M_1} \right)^2 - \sin^2\Theta} \right)^2 , \qquad M_2 \geq M_1 \ . \tag{1.1}$$

M_1 and M_2 are the masses of the projectile and the target atom, respectively, the former having the primary energy E_0 before and the kinetic energy E after the collision in the laboratory system.

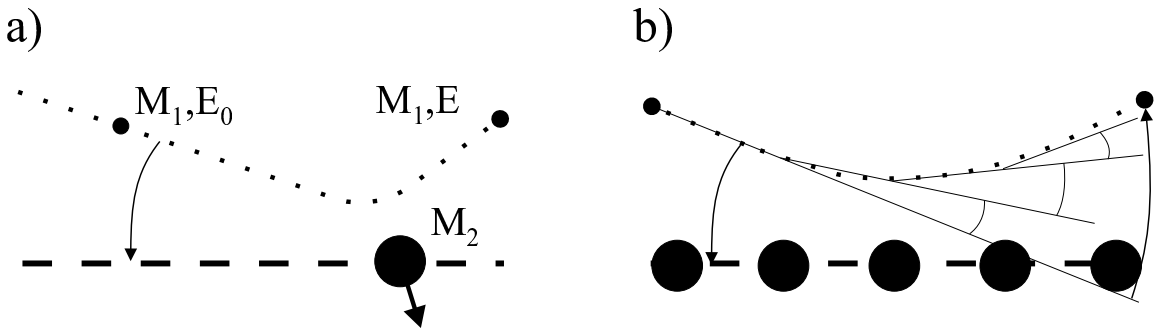

Figure 1.2: a) Binary collision. b) For grazing incidence (small glancing angles Ψ), multiple scattering occurs rather than binary collisions between the projectile and the target atoms.

Via Eq. 1.1, the elastic energy loss is defined as

$$(\Delta E)_{\text{elastic}} = \mathcal{F}(E_0, \Theta) = E_0 - E \quad . \tag{1.2}$$

Equations 1.1 and 1.2 can be used to show how small the amount of elastic energy transferred from the C.O.M. system of the projectile to the target crystal lattice is, for the scattering geometry illustrated above. Assuming the 'worst case' combination of parameters used in this work, namely a projectile of mass $M_1 = 28$ u (representing the mass of a nitrogen molecule), a scattering angle of $\Theta = 10°$ and a target atom with $M_2 = 106$ u (palladium), the elastic energy loss is only

$$(\Delta E)_{\text{elastic}} \approx 0.008 \cdot E_0 \quad , \tag{1.3}$$

i.e., less than 1% of the initial energy.

In fact, the elastic energy transfer is even smaller, since the condition for a binary collision as assumed in Eq. 1.1 is not given in the experiments on grazing scattering off surfaces. Fig. 1.2b shows how the total scattering angle Θ separates into numerous small angles θ_n due to multiple scattering events. The total energy loss thus achieved is the sum of multiple evaluations of Eq. 1.2:

$$(\Delta E)^{\text{tot}}_{\text{elastic}} = \mathcal{F}(E_0, \theta_1) + \mathcal{F}(E_1, \theta_2) + \mathcal{F}(E_2, \theta_3) + \ldots \quad . \tag{1.4}$$

For $\mathcal{F}$ being a convex, monotonously growing function for small angles Θ, the energy loss which results from Eq. 1.4 is smaller than for a single binary collision with the same total scattering angle (Fig. 1.2a, Eq. 1.1) [20, 26, 27].

Furthermore, the constituents of a diatomic molecule scatter rather independently from the surface [4, 28]: in the above example we have to consider two particles, each with

the mass ($M_1 = 14$ u) instead of one with ($M_1 = 28$ u). Eq. 1.1 depends on this parameter non-linearly in a similar way as for Θ, so for the given molecule, the sum of energy losses of both atoms is less then the energy which would be transferred from one single projectile of twice the mass.

For molecular projectiles, vibrational and rotational excitations due to the elastic interaction may occur. The respective energies for the diatomic molecule are calculated by Bitensky *et al.* in [28] as follows:

$$E_{rot} = \frac{E_0}{2}\left((\Theta_1 - \Theta_2)^2 + \left(\frac{\Theta r \psi}{b}\sin\phi\right)^2\right) \tag{1.5}$$

$$E_{vib} = \frac{E_0}{2}\left((\Theta_1 - \Theta_2)\,\psi\cos\phi - \frac{\Theta r \psi^2}{b}\sin^2\phi + \left(1 + \frac{m}{M}\right)\Theta\,(\Theta_1 - \Theta_2)\right)^2 \tag{1.6}$$

Θ is the scattering angle for the C.O.M., r the intramolecular separation, b the impact parameter of the molecular constituent which is nearest to the surface, and ϕ the azimuthal orientation of the molecular axis. Θ_1 and Θ_2 are the two glancing angles of the respective constituents which must not differ too much. Furthermore, the validity of Eqs. 1.5 and 1.6 is restricted to small angles ψ between the molecular axis and the surface.

The transfer of kinetic energy from the laboratory system into the C.O.M. system as rovibrational excitation might eventually lead to dissociation of the molecule. The importance of this mechanism, especially for the nitrogen molecule, will be discussed in more detail in Chapter 4.

1.1.2 Charge Exchange Processes

In the first phase of the scattering event, the positive ion approaches the surface, at some time advancing close enough for electron tunneling processes to take place. The initial neutralization process is the first electron transition in which the impinging molecular ion is involved.
Charge exchange processes have a typical time constant of $10^{-16} \ldots 10^{-15}$ s – short enough for the duration of molecule-surface interactions which typically range from 10^{-15} to 10^{-13} s in the experiments performed in this work. For this reason, it can be assumed that the neutralization of the ions is already complete in the incoming part of the trajectory [29, 30, 31, 32].

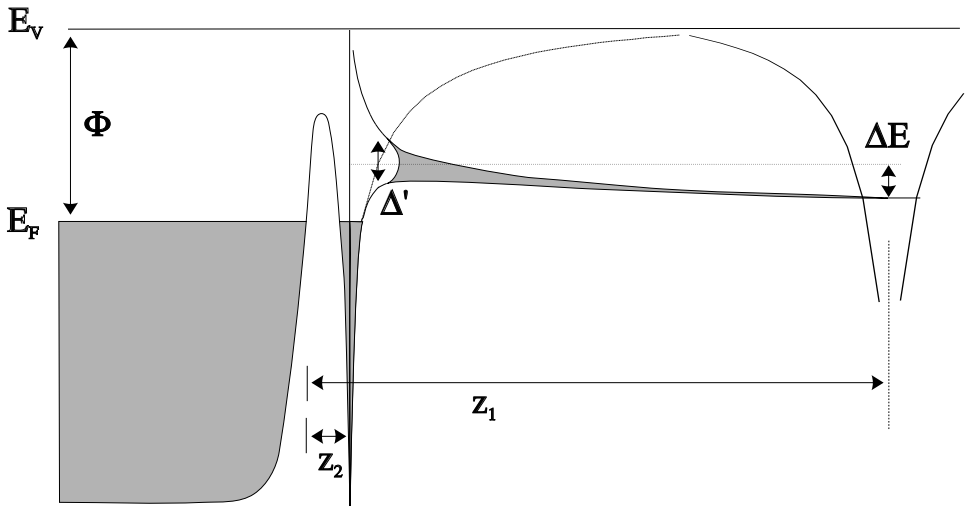

Figure 1.3: Shifting (ΔE) and broadening (Δ') of the valence level in a hydrogen-like atom approaching a metallic surface [31]. E_F: Fermi level, E_V: vacuum level, Φ: work function of the metal.

Perturbation of the Energy Levels

On its approach towards the surface, the ion is subject to certain perturbation effects which influence the energy levels of its electrons. In Fig. 1.3, this situation is illustrated for the simplest case, a hydrogen-like atom:
First, the valence level shifts up due to the induced image charge of the valence electron and the positive ion core. For example, for the adsorption of alkali atoms on metal surfaces, a typical ΔE of $\approx +0.3$ eV is observed [33].
Secondly, a broadening of the level occurs due to the limited lifetime of the respective electron states. The lifetimes are shortened by the tunneling probability between adsorbate and surface states. As a typical magnitude for this effect, $\Delta' \leq 1$ eV is reported for an adsorbed alkali atom [31, 33].

In contrast to the valence level which is shifted up towards higher energies when the atom approaches the surface, its affinity level is shifted down. A broadening due to lifetime limitation of this vacant state also occurs [34, 35].

As for the atomic levels, the shift and broadening of the energy levels also exists in molecular systems, albeit a quantitative treatment of this problem is much more complicated. Imke *et al.* [29, 36] mention a shift of $\Delta E \approx +1 \ldots 2$ eV and a maximum broadening of $\Delta' \leq 5$ eV for the lowest molecular states of H_2 at a distance of 2 Å to an Al(110) surface.

For projectiles with a high velocity component parallel to the surface ($v_{\|} \gtrsim v_F$), an

additional effect becomes relevant: within the C.O.M. system of the projectile, the substrate electrons appear as energetically excited due to the Galilei transformation of the Fermi sphere [31, 37]. The relative motion at such high $v_{||}$ leads to a shift of the energy scales which can affect the probabilities for certain electronic transitions.
For the experiments with nitrogen in this work, the typical Fermi velocity in metals of several 10^6 ms^{-1} is at least one order of magnitude higher than the velocity of the projectiles (ranging from 4×10^4 ms^{-1} to 2×10^5 ms^{-1}). This allows us to consider the dynamic effects on the electronic structure to be negligible.
In the case of hydrogen, the velocity for molecules with the same energy range is a factor of $\sqrt{14}$ higher and therefore the influence of dynamic effects is stronger. Van Wunnik *et al.* [38] observe a correlation between the charge state of hydrogen scattered from a cesiated tungsten surface and the parallel component of the velocity in their experiments, which they ascribe to this effect.

Electron Transfer

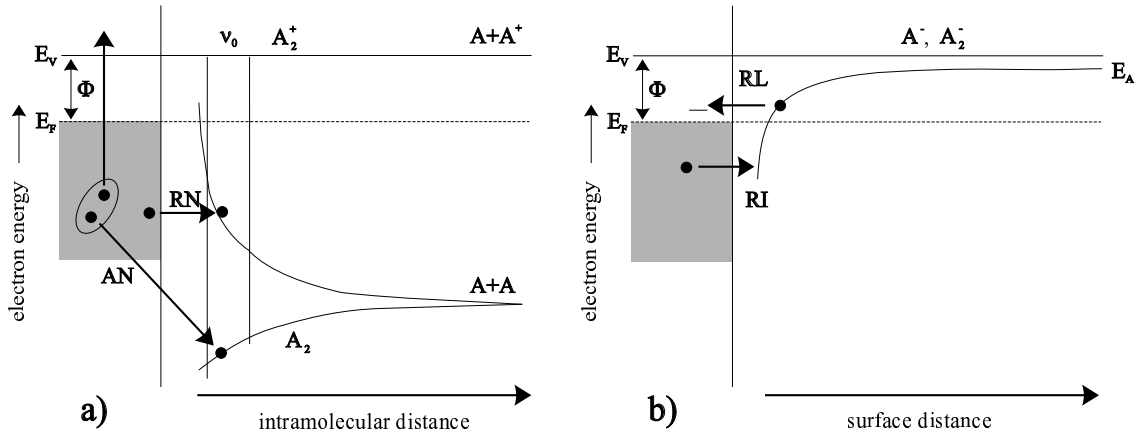

Figure 1.4: Charge exchange processes in front of a metal surface. The occupied conduction band of the metal is schematically depicted as well as its Fermi level E_F, its work function Φ, and the vacuum level E_V. Compared to them are in a): The ionization energies of the first electronic states of an H_2 molecule as a function of the intramolecular distance. The potential curves are normalized with respect to the H_2^+ ground state, perturbation effects (shifting, broadening) due to the presence of the metal are neglected. The most probable capture processes into the Franck-Condon range of the ion's vibrational ground state (ν_0, marked by vertical lines) are shown: resonant (RN) and Auger neutralization (AN). In b): energetic displacement of the affinity level of a neutral atom or molecule versus surface distance.

In the course of a molecular ion-surface interaction, a variety of charge transfer processes are possible. Fig. 1.4a shows the most probable ones for the initial neutralization of the incident H_2^+ as an example.
The Born-Oppenheimer approximation, due to which the electronic response on the

movement of the atomic cores is considered to be adiabatic, is always valid here. Therefore, the Franck-Condon principle restricts transitions to the separation range defined by the initial state, as marked by the vertical lines for $H_2^+(\nu_0)$.
Basically two concurrent processes have to be mentioned [36]: Auger capture into the ground state of the neutral molecule and resonant transfer into an excited state. In most situations, as for the systems studied in this work, a resonant electron transition into the ground state is energetically not allowed. Thus the former two-electron Auger process is favoured. In that case, a second electron from the metal band gains the excess energy and becomes detectable by electron spectroscopy, provided that it is ejected from the surface [39, 40].

The resonant charge transfer rates, in this case to excited states, are orders of magnitude larger, since only one electron is involved. A requirement for such a process is an energetical overlap of the occupied conduction band and the respective molecular state.
For H_2^+, the ground state $X^1\Sigma_g^+$ and the excited triplet state $b^3\Sigma_u^+$ are the main candidates for the neutralization process. As sketched in Fig. 1.4a, the triplet state, which lies resonant to the metal conduction band, is antibonding and leads to dissociation of the molecule, in contrast to the singlet ground state. Recent calculations of the corresponding transition rates show that the neutralization of H_2^+ scattered off Al produces less than 1% of H_2 molecules in the ground state [41, 42]. The situation for the targets used in this work is expected to be the same: Since resonant capture is much faster than the Auger process, it can be assumed that the majority of H_2^+ ions are neutralized into the repulsive $b^3\Sigma_u^+$ state. As a consequence, high dissociation rates for the scattering of H_2^+ from metals should be expected, in contrast to what is reported from experimental studies [12, 16, 39, 43].

Lorente *et al.* show in [42, 44] that there is no direct correlation between the resonant neutralization and the molecular decay: The latter process is slow enough for the dissociating molecule to become de-excited into its stable ground state during the incoming trajectory.
To this end, a triplet to singlet conversion from the $b^3\Sigma_u^+$ to the $X^1\Sigma_g^+$ state is necessary, mediated by the metal surface. Because of the difference in spin state, this process has to involve exchange. The so-called Auger de-excitation is comparable to the singlet-triplet conversion of He^* involving its intermediate He^- [45, 46] and in analogy, it can be considered as a two-step process, involving the unstable $H_2^-(^2\Sigma_u^+)$ resonant state [41]:

$$H_2^*(b^3\Sigma_u^+) + e_M^- \rightarrow H_2^-(1\sigma_g^2 1\sigma_u, ^2\Sigma_u) \rightarrow H_2(X^1\Sigma_g^+) + e_f^- \quad , \tag{1.7}$$

where e_M^- is an electron of the metal target and e_f^- the ejected $p\sigma_u$ electron with opposite spin to the captured metal electron.

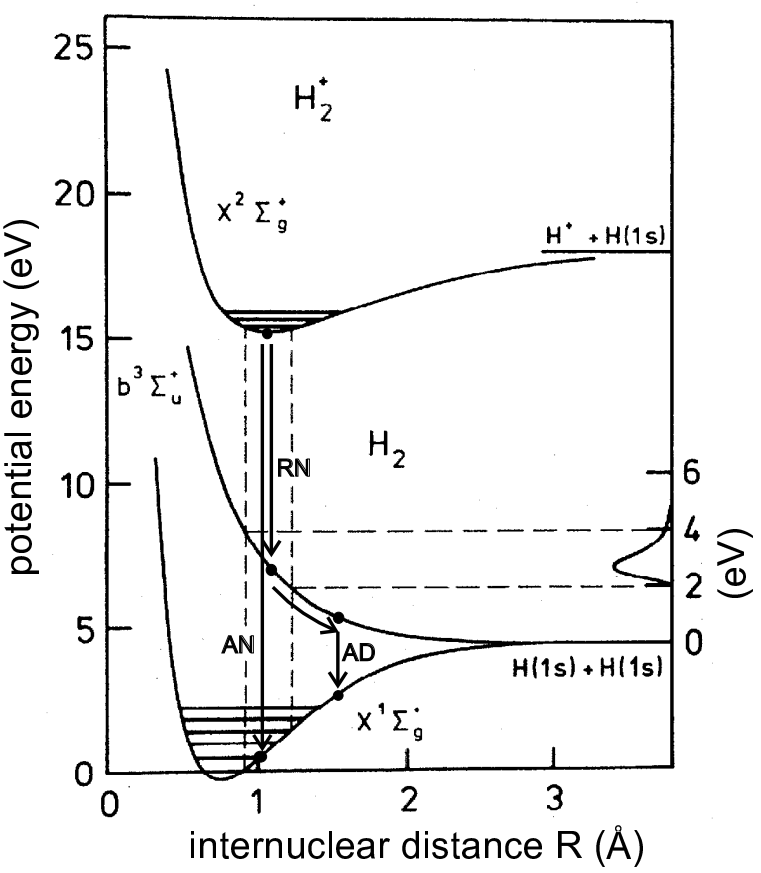

Figure 1.5: Potential curves of unperturbed H_2 and H_2^+ in comparison (adapted from [47]). Under the assumption that the primary ions populate the ($\nu = 0$) vibrational state, Franck-Condon transitions (the allowed region is marked by vertical dashed lines) via Auger neutralization (AN) into $X^1\Sigma_g^+$ lead to $\nu = 1, 2, 3$. Resonant neutralization (RN) into the $b^3\Sigma_u^+$ state and subsequent Auger de-excitation (AD) can produce higher vibrational states. In case of dissociation, the relative kinetic energy distribution of the fragments is schematically plotted on the right.

However, Auger processes like the one just described and the above mentioned Auger neutralization are rather short ranged, in contrast to resonant transitions. Hence, the resonant neutralization of the incoming molecular ions is already completed with a high efficiency before it approaches the surface close enough for the Auger capture process to contribute.

While dissociating along the potential curve of the $b^3\Sigma_u^+$ state (see Fig. 1.5), the molecule transfers its potential energy into relative kinetic coordinates. In case of dissociation of a gas phase hydrogen molecule, a typical relative energy of $2 \ldots 4$eV shows up in the C.O.M. system. However, if Auger de-excitation interrupts this decay process not too late, a vibrationally excited molecule is produced. Thus, a significant

fraction of excited molecules can be transferred into the stable ground state of H_2, explaining molecular survival rates of 20% or more, as observed experimentally.

It is clear from Fig. 1.5, that if the de-excitation sets in exceeding a critical time after the b state is formed, the transferred energy reaches a magnitude where the dissociation is certain, but this time along the potential curve of the $X^1\Sigma_g^+$ ground state. An extended discussion of the de-excitation cutoff problem is given in [41].

The above mentioned was restricted to the H_2 molecule so far. Lorente and co-workers show in [44] that there is a general formula describing the charge transfer scenario for several systems of small molecules A involving a negative ion shape resonance A^- as a reaction intermediate:

$$\begin{aligned} A^+ + e^- &\rightarrow A^* \\ A^* + e^- &\rightarrow A^- \\ A^- &\rightarrow A^0 + e^-. \end{aligned} \tag{1.8}$$

Accordingly, a similar situation is present for the N_2 molecule as well. In contrast to H_2^*, however, the neutral excited state N_2^* is not dissociative. Hence, no contribution from the electronic neutralization process to the dissociation is expected.

Once the ion is neutralized, further charge exchanges are possible along its trajectory. The lowering of the affinity level opens a channel for resonant processes, namely resonant ionization (RI) and resonant loss (RL). See Fig. 1.4b for a schematical illustration.

1.1.3 Energy Losses

The energy loss of scattered projectiles can be of elastic as well as inelastic nature. The elastic energy loss process has been discussed in Section 1.1.1. Under grazing scattering conditions as examined in this work, the observed loss can be attributed mainly to inelastic processes:

$$\Delta E = E_0 - E = (\Delta E)_{\text{elastic}} + (\Delta E)_{\text{inelastic}} \quad \text{with} \quad (\Delta E)_{\text{elastic}} \approx 0 \tag{1.9}$$

Inelastic energy losses can arise from three different processes, depending on the velocity of the respective particle [48, 49, 50]: While at high energies or velocities ($v_{proj} \gg v_F$) ionization processes take place, creation of electron-hole pairs within the electron gas contributes mainly in the low velocity range ($v_{proj} \lesssim v_F$). Also a collective excitation of free electrons (plasmons) on the metal surface is possible which may occur for $v_{proj} > v_F$.

For the energy range studied in this work, electron-hole pair excitations are the dominant process [37, 51]. Thus, the energy loss per trajectory length ds can be expressed through a stopping power S via a friction coefficient γ:

$$S = \frac{dE}{ds} = v_{proj}\gamma \quad . \tag{1.10}$$

Integration over the whole trajectory leads back to the energy loss [27, 52]:

$$\Delta E = (\Delta E)_{\text{inelastic}} = \int_{-\infty}^{\infty} v_{proj}\gamma(s)\, ds \quad . \tag{1.11}$$

Now it is helpful to make use of two approximations. The first is to consider v_{proj} as being constant during the scattering. The second is to approximate the particle's trajectory by negligible entrance and exit sections. This limits the trajectory to a straight line of motion parallel to the surface over a distance L. The whole interaction can thus be restricted to a finite trajectory with an effective friction coefficient $\bar{\gamma}$ [52]:

$$\Delta E = v_{proj} \int_{-\infty}^{\infty} \gamma(s)\, ds \tag{1.12}$$

is reduced to

$$\Delta E = v_{proj}\bar{\gamma}L \quad . \tag{1.13}$$

Monte-Carlo-calculations based on the binary collision approximation (BCA) using the MARLOWE code [52, 53, 54, 55] reveal that the trajectory length L grows roughly linear with v_{proj}. Under the assumption that the effective friction coefficient $\bar{\gamma}$ is constant in the energy range under study, the energy loss is a linear function of v_{proj}^2 and thus approximately proportional to E_0:

$$\Delta E \sim v_{proj}^2 \sim E_0 \quad . \tag{1.14}$$

As already discussed in Section 1.1.1 for the elastic energy loss processes, also in case of molecular projectiles the inelastic stopping power affects the constituents independently. This may result in an increase of their angular momenta, which furthermore can contribute to the dissociation probability.

1.2 Interaction Potentials

The interaction between particles can always be described by potentials. The more particles are involved, the more complex is the problem. For binary collisions as found

for atoms in gas phase, the essential physics is described by simple pair-potentials. In Chapter 4, model calculations of the molecular surface scattering process are performed using six-dimensional potential energy surfaces (PES). These PES are also based on analytic pair-potentials but take into account many-body-effects as well.

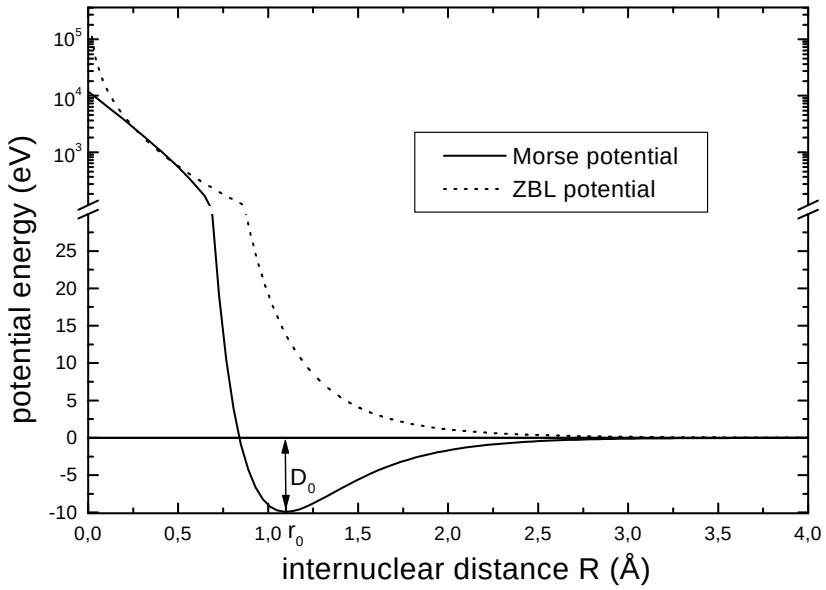

Figure 1.6: Comparison of N-N ZBL potential (dotted line) and N_2 Morse potential (solid line). Note the change of the ordinate from linear to logarithmic scale for high energies.

The two most important pair-potentials used in this work, the ZBL and the Morse potential, are plotted for the case of the diatomic nitrogen molecule in Fig. 1.6 and discussed in the following sections.

1.2.1 ZBL Potential

Based on the Thomas-Fermi theory of atoms [56, 57], a screened Coulomb potential has been proposed by Ziegler, Biersack, and Littmark [58]. This potential represents only the repulsive interaction between two atoms, but has proven to give reliable results for small impact parameters. Its general form is

$$V_{\mathrm{ZBL}}(R) = \frac{Z_1 Z_2 e^2}{R} \cdot (0.1818e^{-3.2x} + 0.5099e^{-0.9423x} + 0.2802e^{-0.4029x} + 0.02817e^{-0.2016x}) \tag{1.15}$$

with

$$x = R/a_{\mathrm{ZBL}} \quad \text{and} \quad a_{\mathrm{ZBL}} = \frac{0.88534 a_0}{Z_1^{0.23} + Z_2^{0.23}} \,,$$

where Z_1 and Z_2 are the atomic numbers of the corresponding atoms, e is the elementary charge, a_0 the Bohr radius, and R is the internuclear distance.

1.2.2 Morse Potential

The Morse potential has the form

$$V_{\mathrm{Morse}}(R) = D_0 \left(1 - e^{-\alpha(R-r_0)}\right)^2 - V_0 \tag{1.16}$$

and is used for the analytic description of the interaction in bound dimers. The parameters directly reflect physical meanings (cf. Fig. 1.6): r_0 is the equilibrium distance and D_0 is the well depth of the potential curve as a measure for the dissociation energy, i.e., the difference between the minimum (which is located at r_0) and the energy for infinite separations ($R \to \infty$).

For the gas phase nitrogen molecule, the most suitable parameters are [59]: $D_0 = 9.9\,\mathrm{eV}$, $\alpha = 2.687\ \mathrm{\AA}^{-1}$, and $r_0 = 1.098\ \mathrm{\AA}$.
The last term V_0 in Eq. 1.16 is arbitrary; e.g. in Fig. 1.6, $V_0 = D_0$ is chosen in order to force $V_{\mathrm{Morse}}(\infty) = 0$.

The Morse potential does not fulfil $V_{\mathrm{Morse}}(R) \to \infty$ for $R \to 0$, hence it fails to describe interactions for small impact parameters. For this part, the ZBL potential is more accurate. In Chapter 4, both types of potentials will be combined in one analytic expression in order to get a better representation over a wide range of internuclear distances.

1.2.3 Screening Effects

When a molecule approaches the surface, its bond weakens (s. Fig. 1.7). This effect can be observed for instance by High-Resolution Electron Energy Loss Spectroscopy (HREELS) as a decrease of the molecule's vibrational frequency when the molecule is adsorbed [60, 61, 62]. The softening is caused by the mutual screening of the molecular constituents through the delocalized metal electrons [19, 63].

For systems with fast moving molecules, the softening can become a dynamical process, as for the charge state of moving (atomic) ions in matter [64, 65, 66]. The molecule-surface interaction time reaches the order of magnitude of the typical time constant of

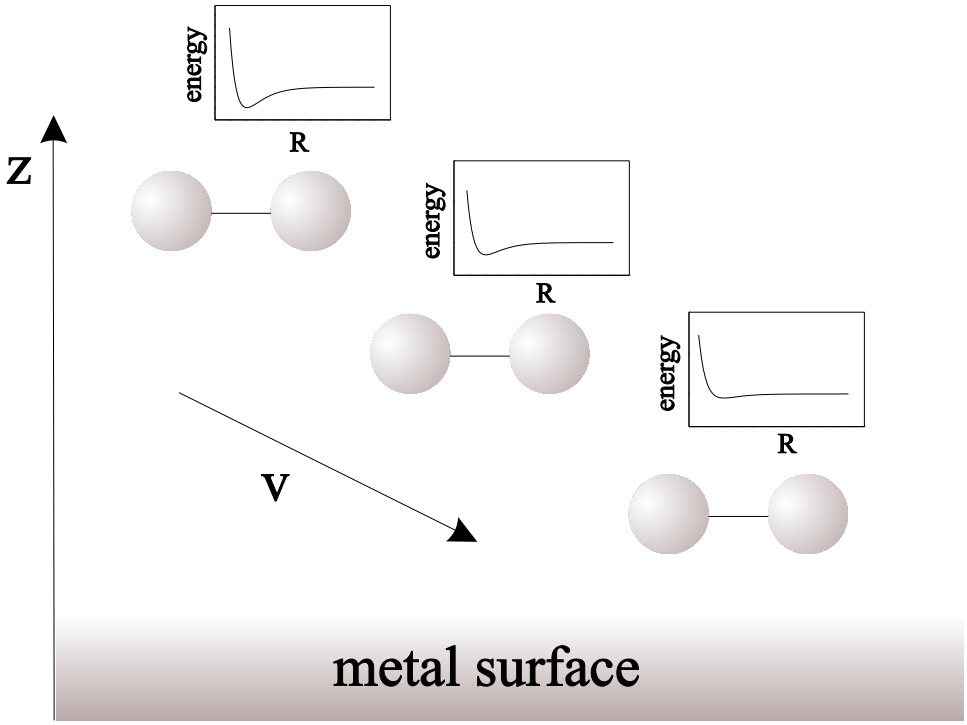

Figure 1.7: Softening of the intramolecular bonding forces, caused by the presence of free electron gas at the surface. Illustration from [16].

electronic processes, hence, if the velocity of the molecule becomes comparable to the Fermi velocity ($v_{\mathrm{proj}} \gtrsim v_F$), the softening can be incomplete. Due to its nonadiabatic character, the term *dynamic* screening [17, 18] is justified. Anyway, the dissociation is affected due to the lowering of the intramolecular binding force [19].
The projectile velocity v_{proj} obtained with N_2 and the primary energies in this work ranges from $4 \times 10^4 \mathrm{ms}^{-1}$ to $2 \times 10^5 \mathrm{ms}^{-1}$, i.e., at least one order of magnitude lower than typical Fermi velocities of several 10^6 ms^{-1} in metals. For molecular hydrogen in the same primary energy range, the resulting velocities are higher, in this work ranging from $1 \times 10^5 \mathrm{ms}^{-1}$ to $6 \times 10^5 \mathrm{ms}^{-1}$.

Chapter 2

Experiment

In this chapter, the 'hardware' used for the investigations in this work will be presented. This does not only concern the apparative setup, but also the samples, their preparation, and analysis will be described. Special attention is drawn towards the time-of-flight system, which is the most important tool in this work. First of all, the three target materials under investigation will be characterized and compared to each other.

2.1 The Investigated Surfaces

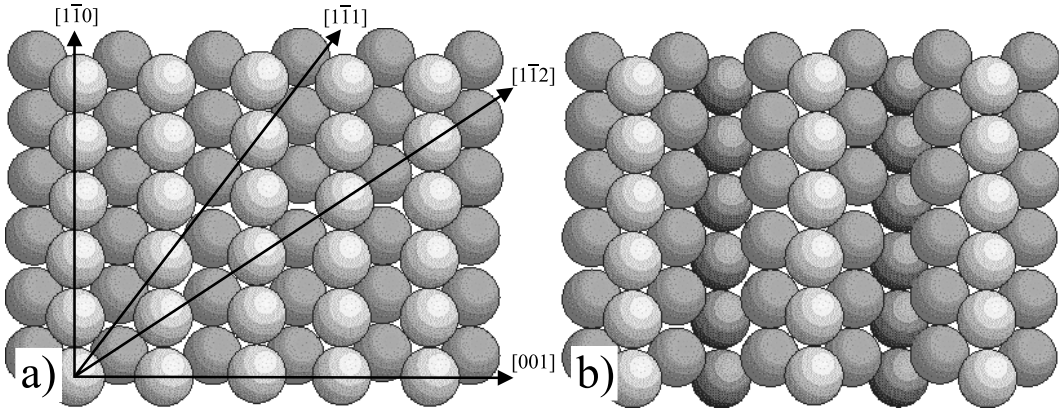

Figure 2.1: Schematical illustration of the fcc(110) surface with the most important crystallographic directions: a) unreconstructed (1×1), b) 1×2-reconstructed.

The investigations in this work extend over the fcc-structured[1] metals palladium (Pd), silver (Ag), and platinum (Pt).
The (110)-surfaces of these single crystal samples provide semichannels of different structure and width. Fig. 2.1a shows the schematic structure of such a surface in the

[1] fcc = **f**ace **c**entered **c**ubic

unreconstructed case, as found for Pd(110) and Ag(110) at room temperature. The crystallographic directions $[1\bar{1}0]$, $[1\bar{1}1]$, and $[1\bar{1}2]$ are found under the azimuthal angles $\varphi = 0°$, 35.3°, and 54.7°, respectively. A well chosen 'random' direction, i.e., a direction that can be described with high Miller indices only, can be found at $\varphi = 45°$ [32, 51] for all mentioned samples.

The $[1\bar{1}0]$-direction is of special interest: it provides closely-packed atom rows which are separated from each other by the lattice constant a_0. The distance of two neighboring atoms within a row is $a_0/\sqrt{2}$.
In contrast to the two other metals, Pt(110) is reconstructed at room temperature in the 1×2-*missing-row* pattern [67]. Fig. 2.1b gives an illustration of this structure. The most important constants for the three surfaces are summarized in Table 2.1.

For ion scattering under grazing conditions, significant channeling effects are expected for low-index azimuthal incidence [68, 69]. As predicted by simulations for the scattering of molecular projectiles [16, 70], a high rotational excitation occurs, in contrast to the high-indexed incidence, where vibrational excitation is dominant. The fcc(110) surface is well designed for studies on this field, especially the Pt(110)(1×2) surface, providing wide and deep semichannels.
The experiments in this work are intentionally performed in order to compare the molecular ion scattering along the low-index $[1\bar{1}0]$- and the high-index 'random'-direction.

Table 2.1: Structural and electronic properties of the surfaces used in this work.

surface	structure	lattice constant a_0	distance between atoms in $[1\bar{1}0]$	distance between $[1\bar{1}0]$-rows	work function Φ
Pd(110)	1×1	3.89 Å[71]	2.75 Å	3.89 Å	5.2 eV[72]
Ag(110)	1×1	4.12 Å[73]	2.92 Å	4.12Å	4.52 eV[71]
Pt(110)	1×2	3.92 Å[74]	2.77 Å	7.84 Å	5.65...5.7 eV

2.2 The Apparatus

The experimental setup has been developed in the early 80's by Willerding *et al.* and is described in detail in [75] and [76]. The apparatus is designed for the scattering of atomic and molecular ions from single crystal surfaces and allows the measurement of energy spectra of positive, negative, and neutral products. It consists of an ultra-high-

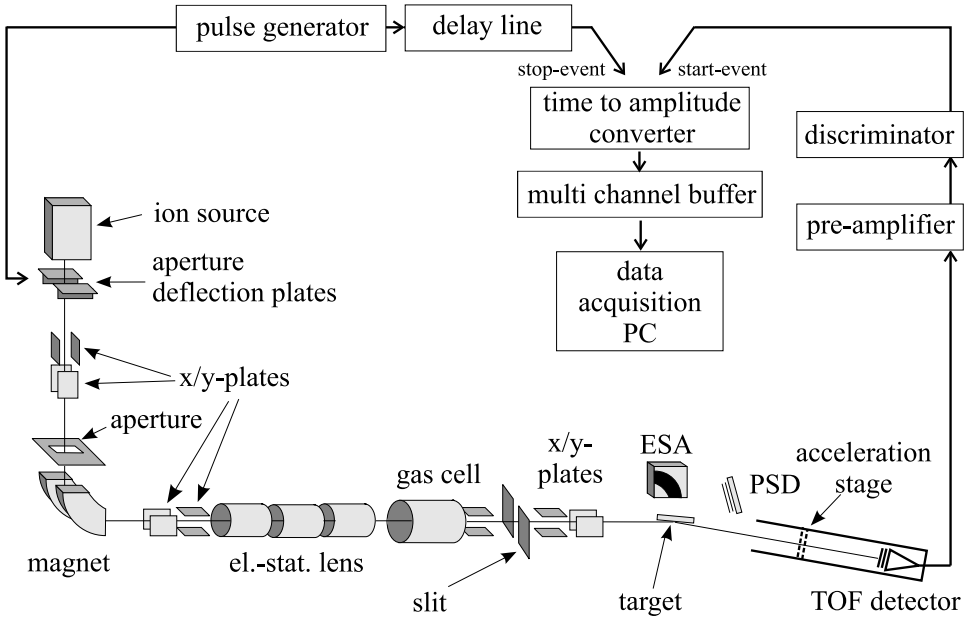

Figure 2.2: Experimental Setup.

vacuum chamber which provides a base pressure of $\sim 2 \cdot 10^{-10}$ mbar and is equipped with a plasma-ion source, an m/q-selection magnet, and a time-of-flight (TOF) detection system. A schematical sketch is given in Fig. 2.2.

The laboratory scattering angle Θ, the azimuthal orientation of the target φ, and the TOF-detector orientation ϑ with respect to the incident beam are variable. To this end, the target as well as the TOF-detector are mounted on movable high precision holders. The angle ϑ is obtained when rotating the TOF-detector for fixed φ, Ψ, and Θ around the axis given by the target surface normal. A range of $-10° \leq \vartheta \leq 10°$ is accessible in the current setup. The polar scattering angle Θ is variable between $0° \ldots 15°$. The TOF-spectra are usually obtained under specular reflection, i.e. $2\Psi = \Theta$ (Ψ is the glancing angle of incidence) and $\vartheta = 0°$. The angle of acceptance of the TOF-detector is 1.2°.

After extraction with a defined voltage from the source, the ion beam passes several apertures, deflection plates, and electrostatic lenses before it hits the target with an effective diameter of about 1 mm. Depending on the primary energy and on the intensity of the beam, a current of up to several 10^{-7} A can be achieved that way. The TOF-tube is surrounded by a pair of Helmholtz coils in order to compensate the earth magnetic field which otherwise deflects (light) ions [12].

Also available in the setup are a LEED system, a position sensitive detector (PSD), and an electrostatic energy analyzer (ESA). These instruments are mainly used for surface

analysis methods which are described later.

2.2.1 The Time-of-Flight System

An electrostatic energy analyzer, as for instance used in this work for the ISS analysis method (cf. Sec. 2.6), can only detect charged particles. The present time-of-flight detection system also allows the spectrometry of neutral particles, which form the majority of the scattering products. Consisting of a 30 mm ø channelplate, the detector is placed in a distance of $s_{\mathrm{TOF}} = 1550$ mm behind the sample. The energy of a given particle is then determined from its time of flight for this length, i.e., primarily the velocity is measured rather than the energy.

For particles of a known mass, the correlation between velocity and energy is simple but since the scattering process leads partly to dissociation of the incident molecules, their mass is halved in the homonuclear case and consequently their energy is redistributed on the fragments. Hence, it is reasonable to use the unit 'energy per atom' from the beginning.

Nevertheless, with a simple trick, mass separation is possible at least for charged secondary particles. To this end, the final section of the TOF-tube – including the detector – is electrically isolated from the rest of the apparatus, so that a high voltage potential (with respect to the target) can be applied. Two parallel metal grids are placed perpendicularly to the beam line inside the isolator ceramic, $s_{\mathrm{acc}} = 861$ mm in front of the detector entrance plane (s. Fig. 2.2). Each of them is put to the potential of target and detector, respectively, which (de-)accelerates the particles depending on their mass and charge state in the electric field over a distance of 1-2 mm.

An absolute time measurement is not possible, since we cannot determine the exact time when the projectile is scattered off the surface. Instead, the absolute time of flight is traced back from two relative measurements.
In order to provide a reference for the time measurement, the beam is pulsed by electronically sweeping it across an aperture. This way, only small ion-packets with a repetition frequency of about $5 \ldots 50$ kHz are directed towards the sample surface, rather than a continous beam. Those particles which are scattered under the appropriate angle into the detector, generate an electrical signal with a certain probability (cf. Sec. 2.2.3). After amplification and pulse shaping, this signal serves as the start command for the time measurement. Meanwhile, the same pulse which initiated the ion packet in the beginning, passes a delay line which is intentionally chosen to lie in a defined time window after the detection event. This time window is limited by the settings of the time-to-amplitude converter (TAC). By means of raising a linear voltage ramp triggered by the start pulse, the TAC realizes the time acquisition. The delayed pulse, whose occurrence is certain in each period, stops a running time measurement if

necessary.

If one particle has been detected, the reached TAC voltage is stored in the multi channel buffer (MCB) by increasing the counter of the associated channel. This way, the whole spectrum consists of counts versus time intervals, $n([t_i, t_{i+1}[)$.
The delay time (typically several μs), the width of the time window (typ. μs), and the chopper period (in the ms range) are parameters to be adjusted for each measurement. With this method, the time-of-flight spectra are acquired on an inverted time scale and must be reversed afterwards.

The benefit of this technique is that the stop event is always given, as initiated periodically from the delay – even for 'empty' periods in which no detector event is registered. Note, that these empty periods are not unusual: The detection electronics is designed for count rates of up to ~1000 per second, which means for a typical chopper frequency of 10 kHz, that on average only every 10th period contributes one count to the total spectrum. If the intensity of the ion beam is tuned in such way that these detection count rates are considerably exceeded, not only the channelplates may suffer from the increased impact; in case of multiple detection events per period, only the first one is registered. Thus, the whole spectrum becomes distorted since only the fast particles contribute.

In order to compute the absolute time scale, the TOF-system has to be calibrated first. A relative calibration is necessary to assign time intervals to each of the 4096 channels of the MCB, according to the actual time window wich is chosen by the TAC. This is done by applying start/stop signals of two exactly defined periods.

In the following absolute calibration, the determination of the energy of the primary beam is performed. The position of the primary peak in the TAC window fixes the absolute time scale. To this end, the primary beam is deflected directly into the detector and measured twice, the first time without, and a second time after applying a defined postacceleration voltage U_{acc}. The accelerated ions are faster in the final part of the flight tube for the length of s_{acc}, reaching the detector Δt earlier than the unaccelerated ions. Δt is well defined since the system has been calibrated relatively before. The (numerical) solution of

$$E_0 + ZeU_{\mathrm{acc}} = \frac{m \cdot s_{\mathrm{acc}}^2}{2} \left(\sqrt{\frac{m \cdot s_{\mathrm{acc}}^2}{2E_0}} - \Delta t \right)^{-2} \tag{2.1}$$

leads to the appropriate primary energy E_0. $Z \cdot e$ is the charge of the primary ions of the mass m.

Assigning

$$t_0 = \sqrt{\frac{m}{2E_0}} \cdot s_{\mathrm{TOF}} \tag{2.2}$$

to the position of the unaccelerated primary peak completes the time calibration.
The feature of relative and absolute calibration is implemented user-friendly in the acquisition application TOFISS written by T. Schlathölter [16].

2.2.2 TOF- and Energy Spectra

For further analysis, it is necessary to convert the time-of-flight spectra into energy spectra. Therefore, not only the abscissa has to be converted but also the count rate has to be corrected. The correlation between time of flight and energy is non-linear:

$$E(t) = \frac{m}{2}\left(\frac{s_{\mathrm{TOF}}}{t}\right)^2 \quad , \tag{2.3}$$

and since the equidistant time-intervals on the abscissa of the TOF-spectra are converted into energy-intervals of different widths, the respective count value $n(]E_{i+1}, E_i])$ has to be corrected by means of

$$\frac{d\,n(]E_{i+1}, E_i])}{dE} \sim \frac{d\,n([t_i, t_{i+1}[)}{dt} \cdot t^3 \quad . \tag{2.4}$$

The application TOFISS can perform this conversion as well and creates a spectrum normalized with respect to its maximum.

Due to the time resolution of the TOF-system, the beam spread on the target and the scatter of the TOF-data, the absolute error of the energy adds up to ± 10 eV for the energy range under study [54].

2.2.3 Detection Efficiencies of the TOF-System

The detection of a particle reaching the detector (which consists of a channelplate) depends on the generation of a sufficient amount of secondary electrons, therefore the detection probability depends on particle energy, mass, and charge state. Several studies about this topic have been published so far [77, 78].

For quantitative analysis as done in this work (cf. Chapter 3), these detection efficiencies must be taken into account. To this end, respective calibration measurements are performed for the particles H^+, H_2^+, N^+, and N_2^+ in the following way [12, 16, 79]:
An ion beam of a defined energy is deflected directly into the TOF-detector, which is running in integration mode (acquiring count rates). While preserving the ion flux,

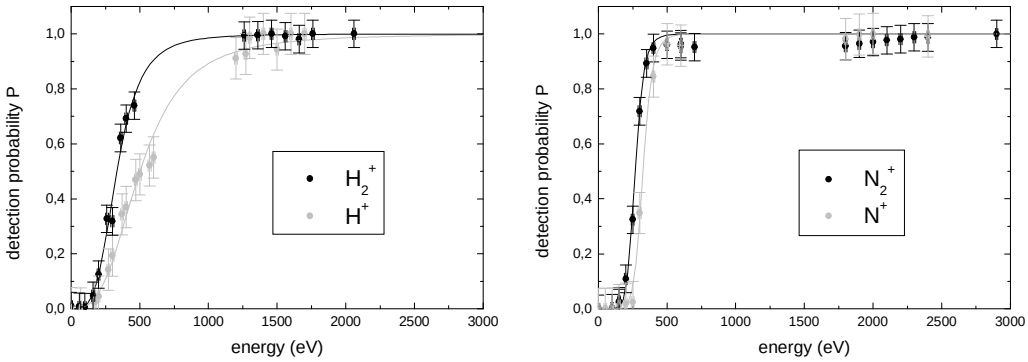

Figure 2.3: Detection efficiencies for (atomic and molecular) hydrogen and nitrogen, respectively, achieved with the TOF-detector. P is determined by count statistics, the error bars ΔP are the standard deviations. The curves are fits using exponential functions.

the final energy can be varied by applying corresponding voltages to the acceleration stage. Saturation of the count rate is reached for sufficiently high energies; this serves as normalization value of the curve $P_{\mathrm{X}}(E)$ (Fig. 2.3).

Since the current setup does not allow to examine the impact of the particles' charge state on the detection efficiencies, it will be neglected in the following.

2.3 Sample Preparation

For all experiments, clean single crystal surfaces are used. The samples have been purchased mechanically pre-polished, so the *in situ* preparation can be restricted to sputtering with an incident 2 keV Ne^+-beam and subsequent annealing at temperatures up to 800°C (Pt).
For a new sample, this preparation process may take several weeks of repeated sputter-annealing cycles.

Once the surface is clean, a steady sputtering at grazing incidence overnight and one final annealing process prior to the measurement is sufficient. To probe the cleanliness of the surface, several analysis methods are used in this work and will be described in the following sections.

2.3.1 Ion Desorption Spectrometry (IDS)

The Ion Desorption Spectrometry makes use of the elastic collisions between the primary ion and a target atom [23, 24]. Based upon the theory of binary collision (cf. Sec. 1.1.1), it is assumed that if a target atom with mass M_2 is desorbed by the impact of the primary ion (mass M_1 and energy E_0), the transferred energy E_{rec} of the recoil

reads

$$\frac{E_{rec}}{E_0} = \frac{4M_1M_2}{(M_1+M_2)^2} \cdot \cos^2\Theta_{\text{rec}} \quad . \tag{2.5}$$

Θ_{rec} is the angle between the trajectory of the recoil and the incident primary beam.

The energetic distribution of the forward scattered recoils under a given Θ_{rec} reveals information about their masses. Thus, substrate- and adsorbate atoms on the target surface can be recognized.
In order to keep the contamination of the sample at a minimum, noble gas ions are used as projectiles.

Ion Desorption Spectrometry can be easily performed with the TOF-System which already is installed in the apparatus. However, since the Ion Scattering Spectrometry delivers better results, this method is described more detailed in the next section.

2.3.2 Ion Scattering Spectroscopy (ISS)

Similar to the above mentioned IDS method, the ISS reveals information about the surface impurity from the elastic interaction between the primary ion and the target [20, 21]. In this case, however, the energetic distribution not of the recoils, but of the scattered ions is analyzed. To be more precise, the energy loss in the elastic collision reveals information about the mass of the target atom, according to Eq. 1.1.

Restricting the scattering angle to $\Theta = 90°$ simplifies the equation to

$$M_2 = \frac{1+\frac{E}{E_0}}{1-\frac{E}{E_0}} \cdot M_1 \quad . \tag{2.6}$$

It is reasonable to choose $\Psi = \Theta/2 = 45°$, as highest intensity is found for specular reflection conditions.
The relatively large scattering angle (compared to the one used for the TOF-measurements) leads to a high elastic energy loss, which in this case is intended. The use of light noble gas ions, usually He^+ at $E_0 = 1.5$ keV, keeps destructive sputtering and implantation into the substrate low.

The energy ratio of such a particle scattered off an Ag atom with $\Theta = 90°$ is

$$\frac{E}{E_0} = 0,9284 \quad . \tag{2.7}$$

With this method, surface contaminations of 10^{-2} monolayers or more can be identified. Fig. 2.4 shows typical ISS-spectra before and after preparation of the Ag sample. For

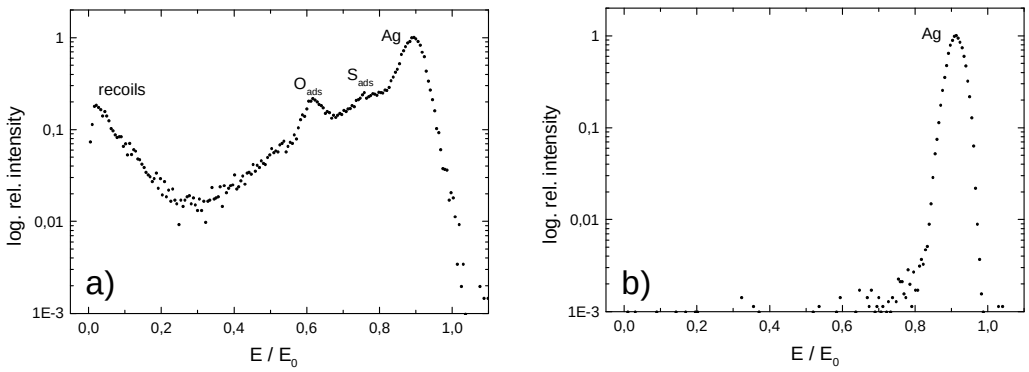

Figure 2.4: Ion Scattering Spectroscopy (ISS) of the Ag sample before (a) and after preparation (b). 1.5 keV He^+ is used as primary ion. The intensity is plotted logarithmically.

the unprepared surface, clear peaks identify the main contaminants oxygen and sulfur.

Due to the conservation of energy and momentum, it is not possible to detect adsorbates with masses below the one of the He projectiles; hydrogen therefore appears only as recoil in the low-energy part of the spectrum.

2.3.3 LEED

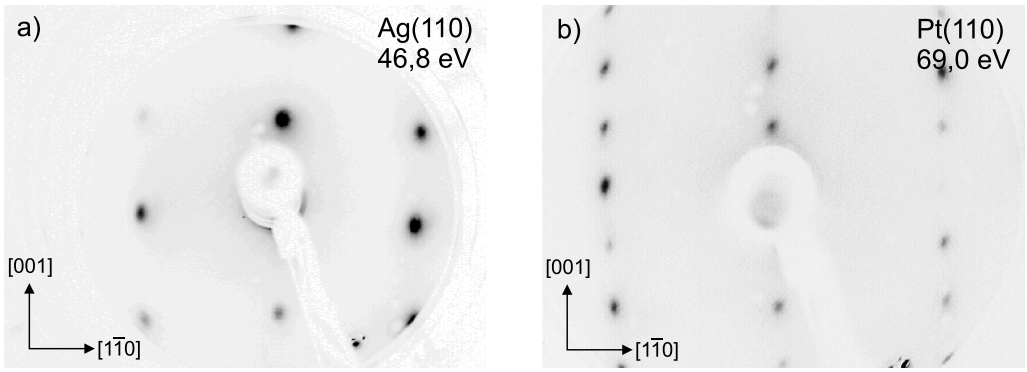

Figure 2.5: LEED pattern of the investigated surfaces (inverted). a) 1×1-structure of Ag(110), which is also found on Pd(110), and b) 1×2-structure of the Pt(110) surface.

A LEED-System (LEED = Low Energy Electron Diffraction, for further details see [80] and [81, 82]) allows to observe the preparation process as well. In addition, this method reveals information about the structure of the surface. A well prepared single crystal surface produces a diffraction pattern with sharp spots, ordered in a reciprocal relationship with respect to the surface lattice.

Some impurities may induce specific reconstructions (e.g. 1×1 for Pt(110)) or form overlayer structures which can be identified in the LEED pattern.

Fig. 2.5 compares the pattern of the clean Ag(110)(1×1) and Pt(110)(1×2) surfaces, respectively. For this work, the LEED analysis is also a very helpful tool for the initial (rough) azimuthal alignment of the samples. The inset coordinate system shows the respective orientations.

2.4 Sample Orientation

The exact azimuthal orientation of the target surface with respect to the ion beam is very important for the experiments performed in this work. As described above, a first rough alignment to the apparatus can already be achieved using the LEED optics. However, this method cannot provide an exact alignment of a given crystallographic direction with the beam. Instead, the scattering of ions itself can be used.

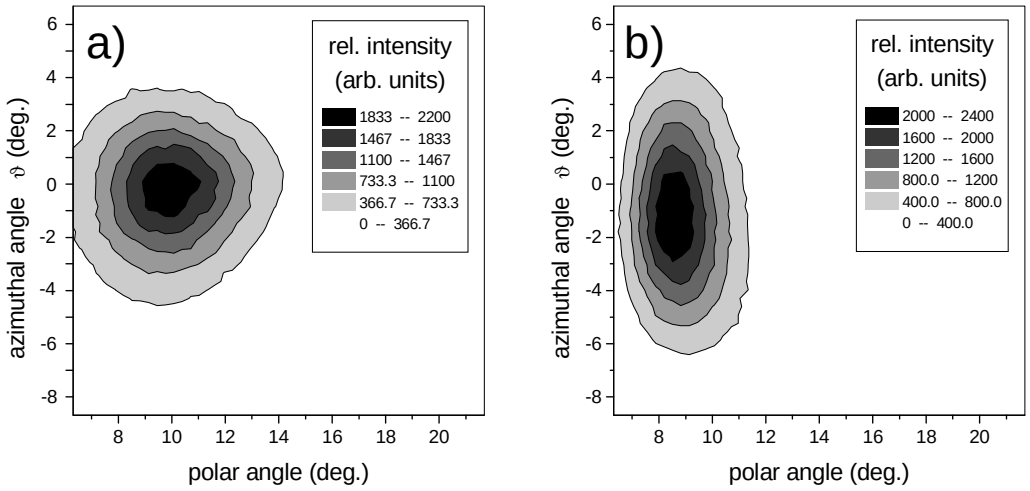

Figure 2.6: Spatial distributions of a forward scattered grazing 2.5 keV Ne^+-beam, as seen by the PSD-detector. The left plot (a) shows the profile due to high-indexed primary beam incidence and the right one (b) results from low-index scattering.

Due to focusing and defocusing of the scattered beam depending on the respective crystallographic orientation, its spatial distribution is sensitively affected. The visualization via the position sensitive detector (PSD) in Fig. 2.6 is shown for 2.5 keV Ne^+-particles scattered off a typical fcc(110) surface. When scattering the ions along a high-indexed direction, the corrugation due to the surface structure tends to average out and the surface acts like a diffuse but overall planar mirror [70], resulting in a round angular distribution as seen in Fig. 2.6a.

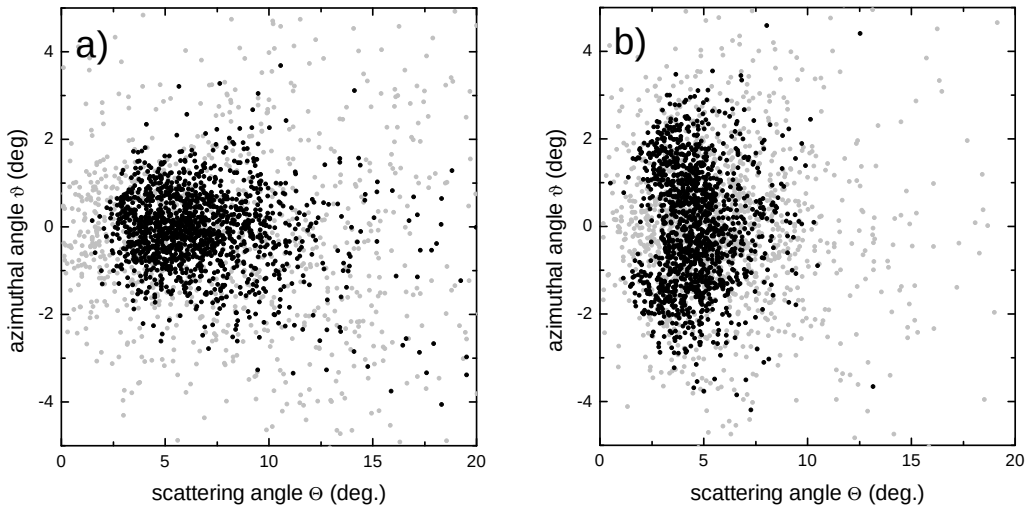

Figure 2.7: Simulated spatial distributions of forward scattered grazing 2 keV $N_2 \rightarrow Pt(110)$, (a) under high- and (b) under low-indexed incidence. Black dots are representative for the detection of intact molecules, gray dots for dissociated N fragments. Such a separation is not possible with the PSD-detector; it just records the distribution of all detected events.

In contrast, when scattering along a low-indexed direction (Fig. 2.6b), a part of the projectiles is guided along the surface semichannels and another part is scattered on top of the potential walls of the rows, leading to the azimuthal broadening of the distribution. The basic principle of this channeling effect is the steering action [83] exerted by the regular array of target atoms on the incoming particle [54]. In some studies on Pd [3, 84], Au [85], and Pb [86, 87], even a 'banana'-shaped pattern has been observed. However, this characteristic shape is only accessible via atomic projectiles as primary particles. The spatial distribution of particles scattered after high- and low-indexed molecular incidence, respectively, is shown in Figs. 2.7a and b. As generated by comprehensive computer simulations (cf. Chapter 4) rather than by experiments, the data in these plots allow a clear distinction between surviving molecules and atomic fragments resulting from dissociation. While the fraction of intact molecules in the scattered beam forms the typical 'banana'-shaped profile (Fig. 2.7b), the diffuse distribution of the atomic particles arising from dissociation covers this steering pattern and leads to an overlayed PSD-picture. This as a result is quite similar to the one seen under high-indexed incidence (Fig. 2.7a) but only a bit more broadened along the azimuthal coordinate.

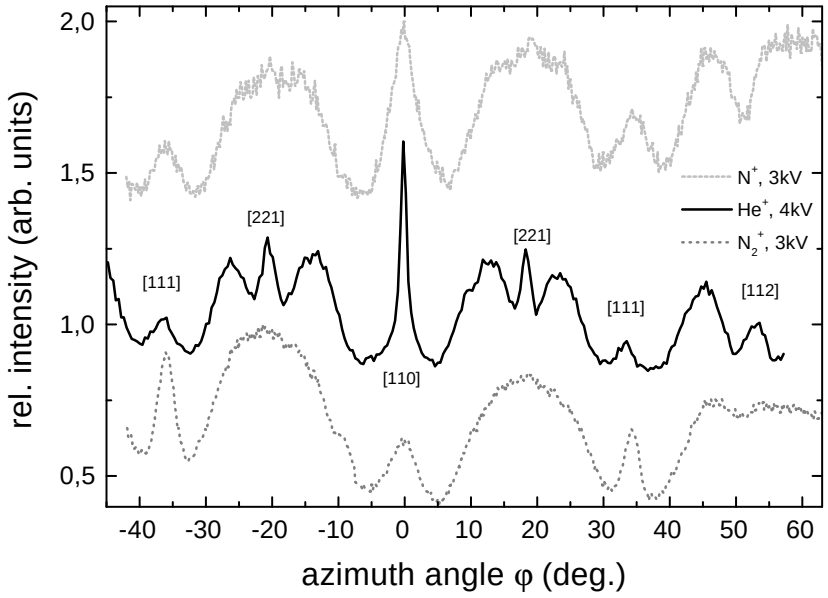

Figure 2.8: Azimuth spectra of a typical 1×1 fcc(110) surface (here Pd(110)) with He^+, N^+, and N_2^+ at different energies in surface channeling geometry measured with the small aperture TOF-detector ($\Psi = 5°, \Theta = 10°, \vartheta = 0°$).

Azimuthal scanning of the count rate achieved by the specularly reflected beam facilitates the determination of the orientation with an absolute accuracy better than $\pm 1°$. To this end, the intensity of the forward scattered particles – using the small aperture TOF-detector – is recorded as a function of the variable azimuth φ, measuring the rotation of the $[1\bar{1}0]$ surface direction with respect to the plane of scattering (Fig. 2.8). The signal increases significantly along low-index directions. For a particle as He^+, this effect is obviously more pronounced (solid black curve in the plot); but even for the diatomic N_2^+-ion, a strong influence of the surface structure is visible. As determined by the fcc(110) geometry, the directions $[1\bar{1}0]$, $[1\bar{1}1]$, and $[1\bar{1}2]$ are found at $\varphi = 0°$, 35.3°, and 54.7°, respectively.

Chapter 3

Results

This chapter is dedicated to present the experimental results of the molecule scattering with nitrogen and hydrogen. The first part gives a general introduction on the form of the acquired energy spectra and the further analysis techniques. Later, the results for the two projectile gases will be presented separately.

3.1 General Results

Since the energy distributions of the scattered particles are to be analyzed, it is necessary to convert the raw time-of-flight spectra into energy scale (cf. Sec. 2.2.2). Fig. 3.1 shows a typical energy spectrum which is obtained from a TOF-measurement.
Attention has to be drawn to the labeling of the energy axis; since molecules are used as primary ions, the spectrum consists in most cases of two superimposed peaks, one formed by the fraction of surviving molecules and the other by the dissociated atoms. Due to their different masses, the total energy scales of both classes of particles differ by a factor two (diatomic, homonuclear molecules). For this reason, it is more elegant to use the relative energy scale (as in Fig. 3.1) or 'energy per atom' (Fig. 3.2).

The intensity scale is usually logarithmic, in order to make both distributions visible. The shape of the distribution is asymmetric: the low energy tail generally levels off slower than the high energy tail, in contrast to the energetic spectrum of the primary beam (i.e., before the surface interaction) which is a Gaussian distribution.

The distribution of the fragments is broadened and partly extends to values higher than E_0. This indicates a dissociation process in which an energy ε is released within the center-of-mass system of the molecule. In the laboratory system, the resulting energy of the constituents can be obtained by a Galilei transformation [75]:

$$E_{lab} = \frac{1}{2}E_i + \frac{1}{2}\varepsilon \pm \sqrt{E_i \varepsilon}\cos\psi \sin\phi \quad , \tag{3.1}$$

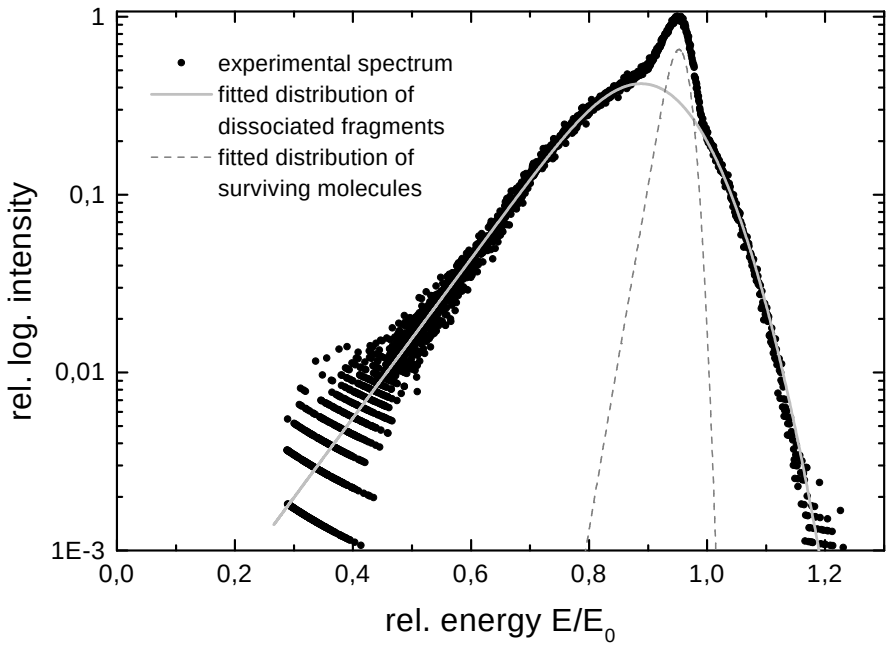

Figure 3.1: Typical energy spectrum obtained from a TOF-experiment (550 eV $H_2^+ \rightarrow$ Pt(110) under high-indexed incidence). Each spectrum is a superposition of atomic and molecular distributions, determined by fitting.

where ψ and ϕ are the angles determined by the molecule's axis orientation and E_i is the kinetic energy of the molecule at the moment of its decay.

Choosing $E_i = E_0$, Eq. 3.1 does not consider any inelastic effects such as energy loss and straggling. These effects, affecting both the molecular and the atomic distributions, give rise to the asymmetric shape of the spectra which is discussed in more detail by Wojciechowski *et al.* [14] and by Närmann *et al.* [88, 89, 90]. These authors use analytic functions to describe the energetic distributions of the forward scattered beam; in this work, the best agreement with the experimental results is found when fitting a universal so-called exponentially modified Gauss-function (EMG) [91]:

$$I = \frac{a_0}{2a_3} \exp\left(\frac{{a_2}^2}{2{a_3}^2} + \frac{E - a_1}{a_3}\right) \cdot \left[1 + \mathrm{erf}\left(\frac{\sqrt{2}}{2}\left(\frac{a_1 - E}{a_2} - \frac{a_2}{a_3}\right)\right)\right] \quad . \tag{3.2}$$

E is the kinetic energy within the laboratory system, $I(E)$ the intensity. The parameter a_0 describes the area, a_1 the center, a_2 the width, and a_3 the distortion of the distribution function, respectively. A function of the type of Eq. 3.2 has been derived *ab initio* by Remizovich *et al.* [92] from the Boltzmann statistics for the small angle approach, taking into account the inelastic energy losses for different trajectories leading to a

given scattering angle. In the work of Närmann *et al.*, the reason for the asymmetry is also the energy loss straggling due to electron exchange processes between the surface and the projectile while moving along its trajectory.

For molecular scattering under channeling conditions, a surprising behavior may arise: For primary energies not too low, the 'hat' in the spectra, which is usually attributed to the surviving molecules, cannot be fitted by one single EMG function anymore (Fig. 3.2b). At least two EMG functions are superimposed here, hence the complete spectrum consists of three peaks. In Chapter 4, it will be shown that the sharp additional peak is not – as intuitively expected – due to surviving molecules but rather the result of a certain class of fragmentation products. The effect mainly occurs under axial surface channeling conditions and makes the proper assignment of the respective fractions more difficult.

The peaks obtained from the fitting procedure can be used to calculate the fraction of surviving molecules via integration of the corresponding distributions:

$$Y = \frac{\frac{1}{P_{\mathrm{N_2}}}\mathcal{N}(\mathrm{N_2})}{\frac{1}{P_{\mathrm{N_2}}}\mathcal{N}(\mathrm{N_2}) + \frac{1}{2 \cdot P_{\mathrm{N}}}\mathcal{N}(\mathrm{N})} \ , \tag{3.3}$$

where $\mathcal{N}(\mathrm{X})$ is the total area under the spectral distribution of particles of species X:

$$\mathcal{N}(\mathrm{X}) = \int_0^\infty n_{\mathrm{X}}(E)\ dE \tag{3.4}$$

and P_{X} their energy-dependent detection probability [93], according to Sec. 2.2.3. For reasons of simplicity, P_{X} is just used as a 'correction factor' for the whole distribution, determined at the energy of its maximum:

$$P_{\mathrm{X}} = P_{\mathrm{X}}(E)|_{E_{\mathrm{max}}} \ , \tag{3.5}$$

rather than performing the integration in Eq. 3.4 over the calibrated distributions, obtained by convoluting

$$n_{\mathrm{X,cal}}(E) = n_{\mathrm{X}}(E) * \frac{1}{P_{\mathrm{X}}(E)} \ . \tag{3.6}$$

The molecular survival rates, as expressed by Eq. 3.3, can now be obtained from the spectra. Respective results using N_2^+ and H_2^+ are presented in the following. The error bars are calculated for some representative data points, based on ΔP_{X} according to Fig. 2.3 and $\Delta\mathcal{N}(\mathrm{X})$ estimated to 5%.

3.2 $\mathbf{N_2^+}$

As already mentioned in the introduction, nitrogen is an inert molecule which so far is known to interact mainly elastically with the target surface [11, 16]. Therefore, the

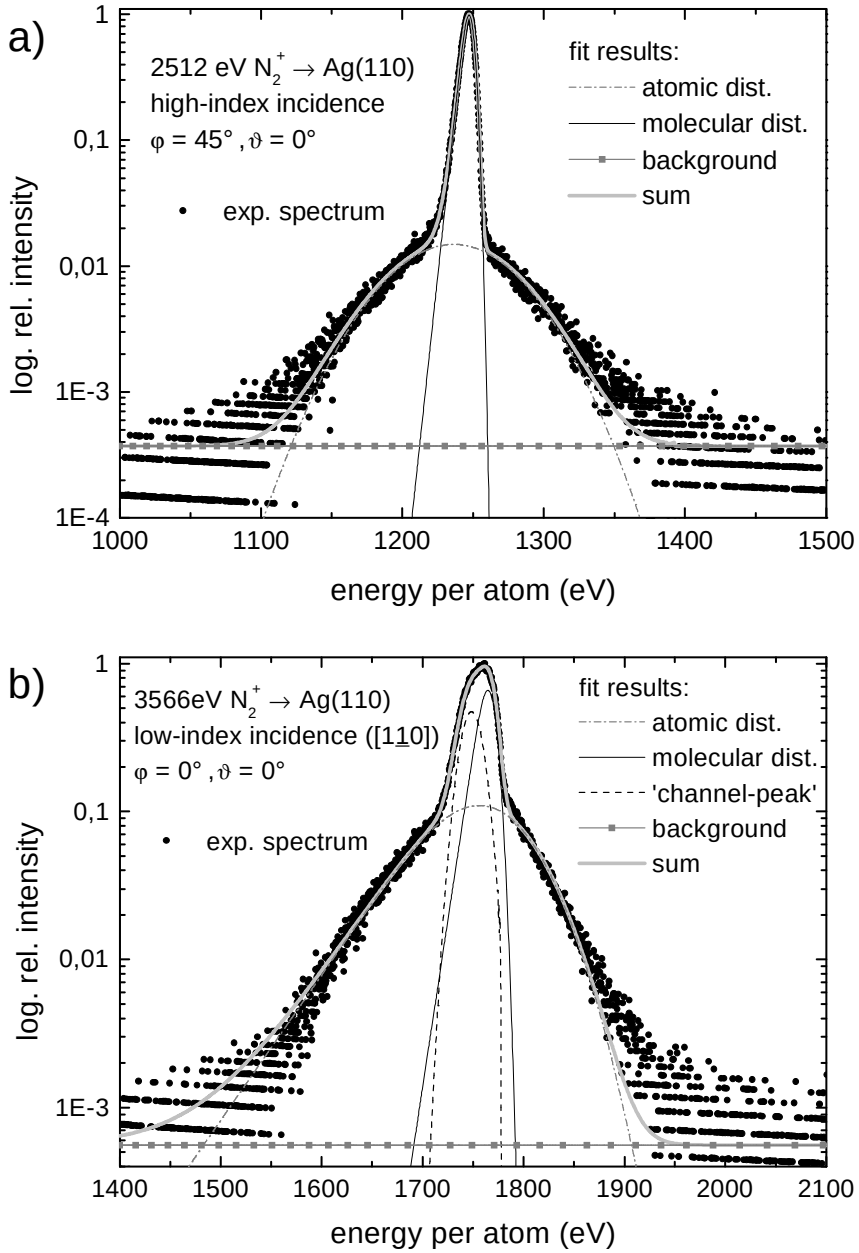

Figure 3.2: Sample energy spectra, obtained from time-of-flight measurements (here $N_2^+ \rightarrow$ Ag(110)). The intensity scale is logarithmic. a) In most cases, the total spectrum is a superposition of one atomic and one molecular distribution, their contributions are determined by fitting EMG functions (see text). b) In case of low-index scattering, an additional distribution appears (at sufficiently high primary energies) which is due to axial surface channeling. The energetic width of this 'channel-peak' is comparable to the molecular one.

opportunity to simulate the scattering process by means of classical trajectory calculations – as done in the next chapter – makes this system particularly interesting.

In general, nitrogen spectra clearly differ from the hydrogen case in such a way that molecular nitrogen survives the scattering process to a larger extent. As a consequence, a comparatively high molecular peak appears in the spectra (cf. Fig. 3.2). Especially for low energies $E \to 0$, the survival is almost complete, i.e. $Y(\mathrm{N}_2) \simeq 1$.

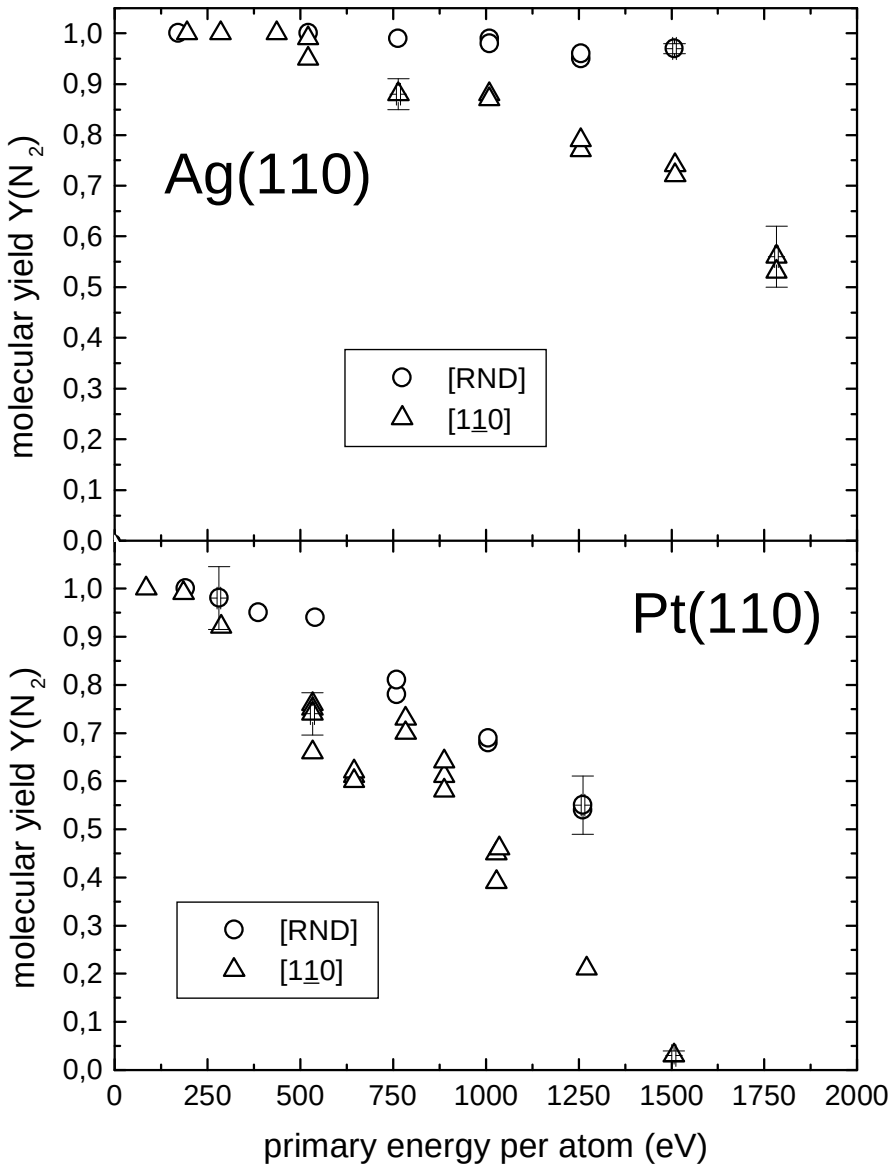

Figure 3.3: Molecular yields obtained from scattering N_2^+ off Ag(110)(1×1) and Pt(110)(1×2), each for both the random- (◯) and the $[1\bar{1}0]$-direction (△) under grazing incidence ($\Psi = 3.1°, \Theta = 6.2°, \vartheta = 0°$).

Fig. 3.3 displays the experimentally obtained molecular yields $Y(N_2)$ as a function of the projectile energy E_0. It is obvious, that $Y(N_2)$ depends on the target (Ag, Pt, or also Pd as follows) as well as on the azimuthal angle of incidence φ. However, the same trend is visible for all cases: Starting with comparable yields for all orientations in the low-energy region, a clear azimuth dependent behavior becomes apparent for higher energies. Obviously, the yield for the $[1\bar{1}0]$-scattered particles decreases faster with increasing energies than for higher indexed directions, though for the Pt(110) surface, the difference between scattering along the 'random' and the $[1\bar{1}0]$-direction is not as clear as for Ag(110).
Anyway, the fragmentation on Pt(110) is generally stronger for an identical scattering geometry, especially in case of the random direction. This result is not surprising, since the molecules are exposed to a stronger corrugation due to the 1×2-reconstruction.

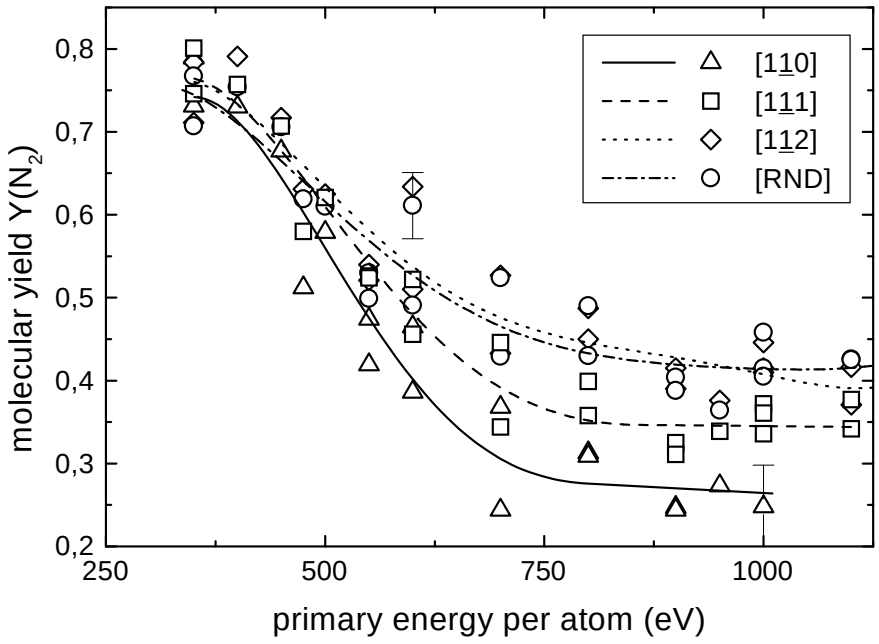

Figure 3.4: Molecular yields obtained from TOF-measurements on palladium, scattering under grazing incidence ($\Psi = 5°, \Theta = 10°$). The atomic and molecular distributions are determined by fitting Gauss-functions to the energy spectra.

In addition to the scattering experiments with Ag(110) and Pt(110), also some experiments with N_2^+ and Pd(110) are performed [94]. Due to a slightly different apparative setup, these measurements are performed under $\Psi = 5°$ and $\Theta = 10°$, respectively. The data for the molecular survival are plotted in Fig. 3.4.
Obviously, the larger scattering angle results in higher kinetic energy components associated with velocity components perpendicular to the surface and gives rise to higher

fragmentation. It has to be noted here, that the Pd results have been determined using a simple Gaussian fitting procedure [94], which turned out to be less accurate and reliable than the 'new' method using formula 3.2.

Nevertheless, the trend in Fig. 3.4 is qualitatively equivalent to the behavior observed with Ag(110) and Pt(110) above. The dissociation probability increases when going from the $[1\bar{1}2]$ to the $[1\bar{1}1]$ and the $[1\bar{1}0]$ directions, respectively. No remarkable difference can be seen between the $[1\bar{1}2]$- and the random direction, but their survival probabilities exceed those of $[1\bar{1}0]$ and $[1\bar{1}1]$ over the complete energy range under study.

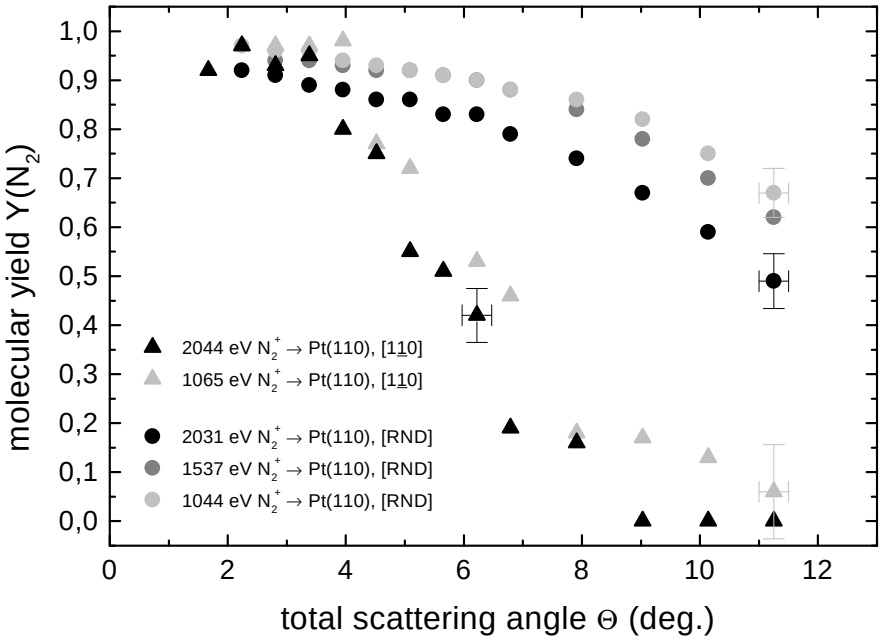

Figure 3.5: Molecular survival probabilities obtained from measurements with Pt(110)(1×2) when varying the total scattering angle Θ. The fragmentation is more pronounced for $[1\bar{1}0]$-incidence than for highly indexed directions.

In a next step, the influence of the scattering angle Θ on the molecular yield for N_2^+ scattering from Pt(110) at constant primary energies is studied. Fig. 3.5 illustrates the results for some selected energies for both azimuthal orientations encountering the $[1\bar{1}0]$- and the high-indexed direction, respectively.
Beside the strong decrease of $Y(N_2)$ with Θ, a dramatic difference is found when comparing the results for the two directions under study: At larger Θ the dissociation is strongly enhanced for scattering under channeling conditions.

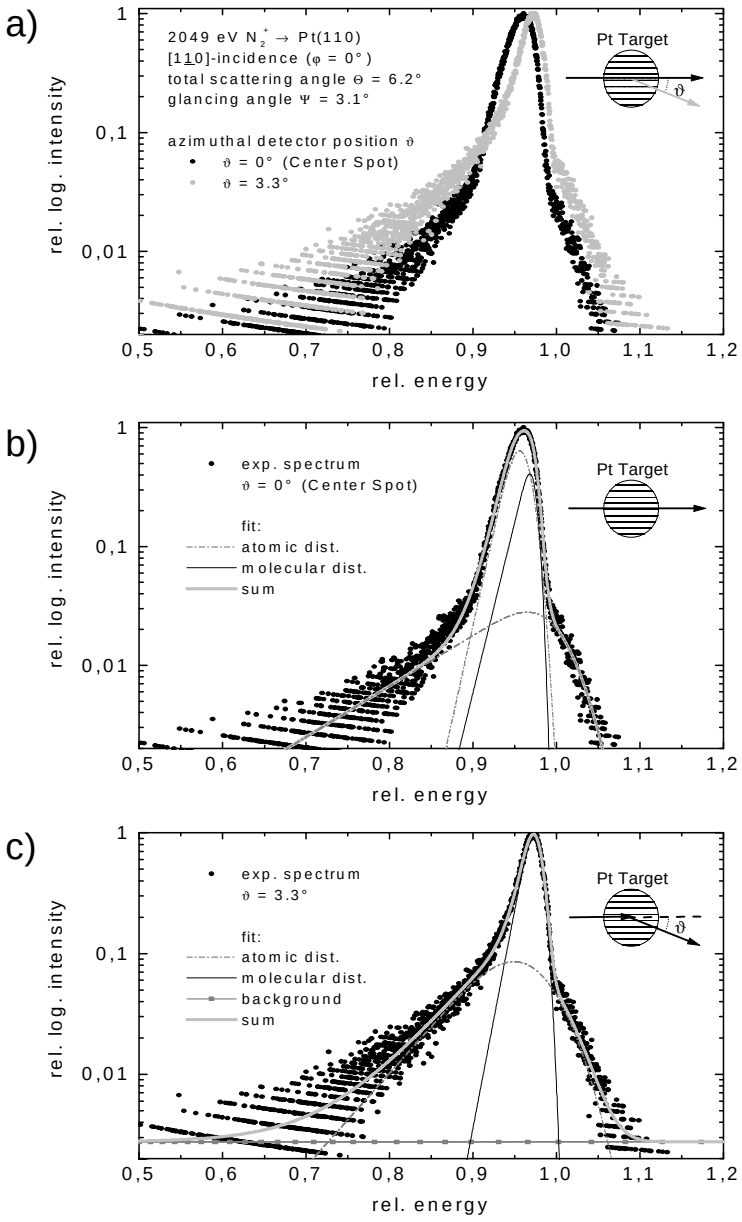

Figure 3.6: TOF-energy spectra of N_2^+ scattered off the 1×2-reconstructed Pt(110) under low-indexed incidence along the [1$\bar{1}$0]-semichannels. a) Two spectra measured at different azimuthal detector positions behind the target: The center spot ($\vartheta = 0°$) and a position slightly outside the specularly reflected beam ($\vartheta = 3.3°$). The underlying geometries are also illustrated in the insets. b) Obviously, the 'channeled' nitrogen fragments are focused into a small region centered in the plane of scattering. Here, the atomic distribution prevails in the narrow 'hat' of the spectrum, but gives way to the molecular contribution when turning the detector off-center (c).

A special measurement, also in view of a later comparison with the appropriate simulations (s. Chapter 4), is performed to learn more about the 'channel peak', which occurs mainly under optimal channeling conditions (s. Fig. 3.2b). To this end, it is of interest to investigate the scattering from the more corrugated Pt(110)(1 × 2) surface with its wide semichannels.
A beam of 2049 eV N_2^+ is scattered along the $[1\bar{1}0]$-direction of Pt(110). The specularly reflected particles which are detected within the scattering plane as well as for detection at an increased azimuthal angle $\vartheta = 3.3°$ in the wing of the PSD profile (cf. Fig. 2.7b) are shown in Fig. 3.6a.
These spectra, showing surprisingly different shapes, are further analyzed in Fig. 3.6b and c, respectively. Obviously, the additional sharp distribution is only present under specular reflection (Fig. 3.6b), indicating that the respective atoms are axially guided by the surface semichannels. These atoms are thereby focused into a very small spot within the scattering plane. Away from the specular reflection, the remaining sharp distribution is due to scattered molecules only (Fig. 3.6c).

3.3 H_2^+

For the case of molecular hydrogen projectiles, the scattering from Ag(110) and Pt(110) surfaces is studied in this work.

A typical feature in most of the spectra – even when originating from high-index incidence – is the presence of two distinct distributions contributing to the fraction of dissociated particles. Fig. 3.7 gives an example for 1520 eV H_2^+ scattered off Ag(110) along a random direction. The two atomic peaks (not to be confused with the additional sharp 'channel peak' which is mainly observed when scattering along crystallographic directions) indicate the presence of two different dissociation processes.

Fig. 3.8 shows for comparison a typical energy spectrum obtained from scattering H_2^+ off LiF(100), a wide band-gap insulator [95]. The single crystal is heated up to 330°C during the measurement in order to avoid a pile-up of surface charges.
In this case, the atomic distribution is formed by one single peak, as observed in the spectra of N_2^+ under high-indexed incidence. Obviously, one channel for dissociation is switched off by the presence of the band gap. A similar situation is also given for the oxygen–insulator systems O_2^+/diamond(111) [96, 97, 98] and O_2^+/MgO(100) [99].

The total molecular yields from scattering H_2^+ off metals show an entirely different behavior from N_2^+ (s. Fig. 3.9): only very few molecules with energies below 500 eV per atom survive the scattering along the $[1\bar{1}0]$-direction on both, silver and platinum. A remarkable difference between the two metals however becomes apparent for the high-index case. While the survival rates on Pt(110) are in random direction comparatively

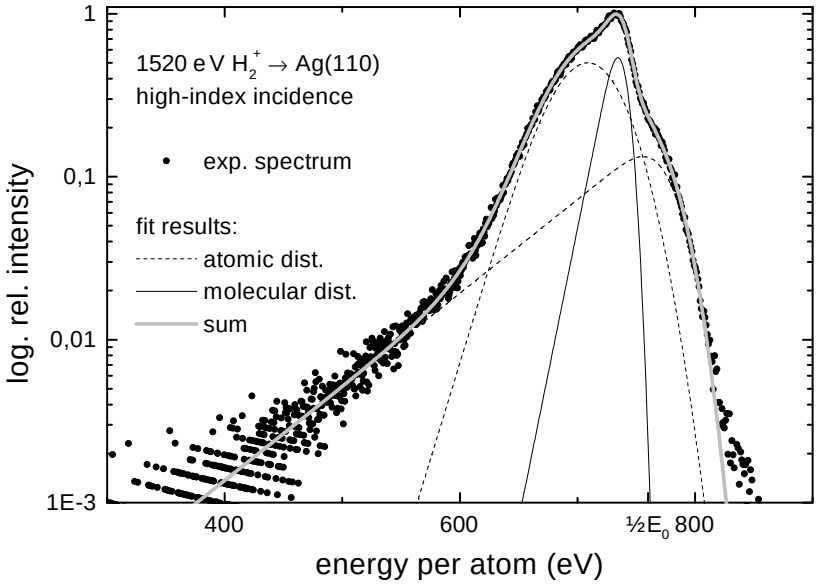

Figure 3.7: Energy spectrum from scattering H_2^+ off Ag(110) under high-indexed incidence. The atomic and molecular distributions are determined by fitting. The two (broad) atomic distributions indicate two different dissociation mechanisms.

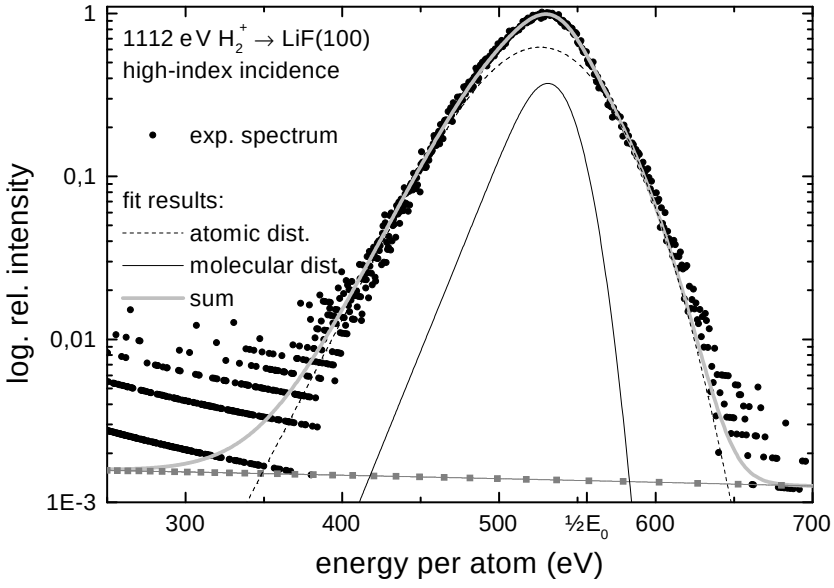

Figure 3.8: Energy spectrum from scattering H_2^+ off LiF(100) under grazing incidence ($\Psi = 5°, \Theta = 10°, \vartheta = 0°$) along a high-indexed direction. [95].

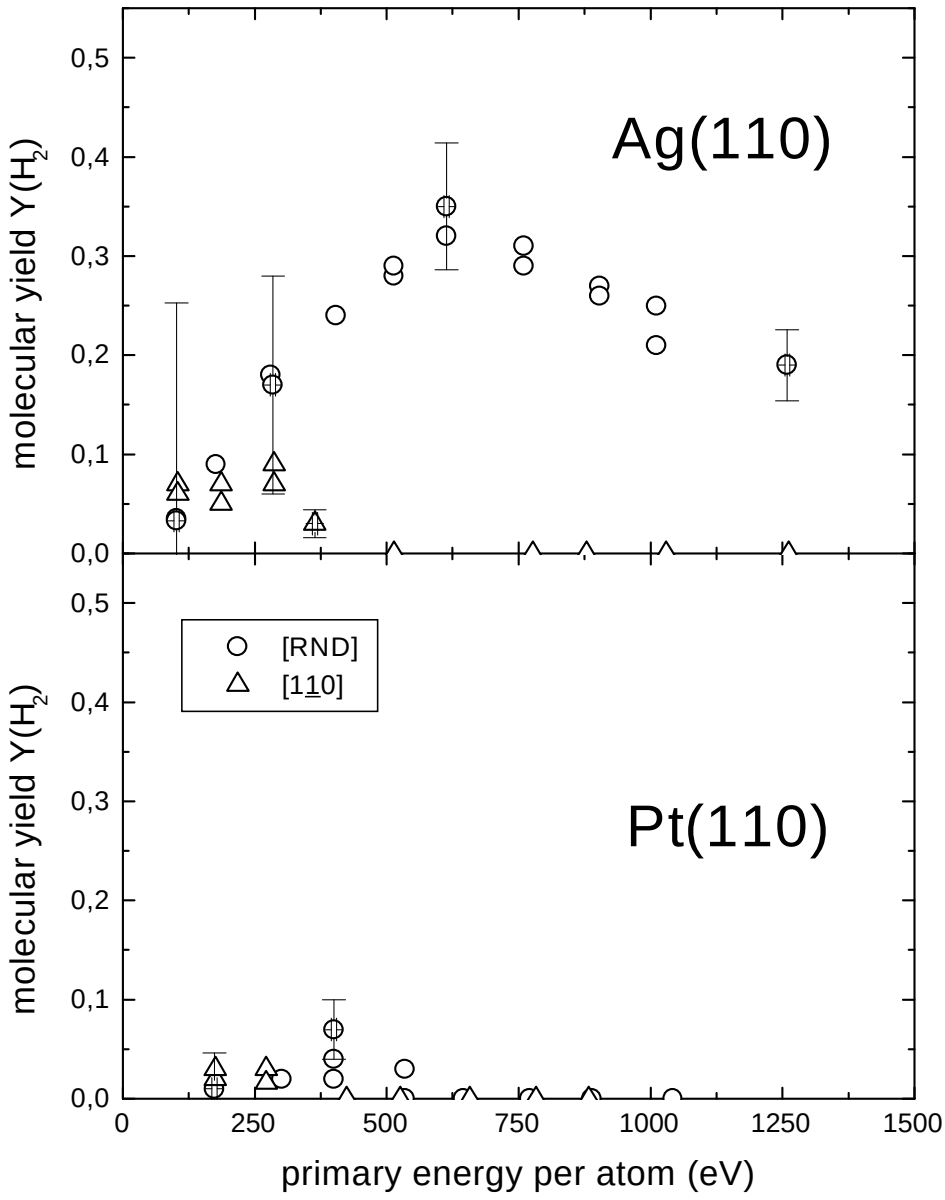

Figure 3.9: Molecular yields from scattering H_2^+ off Ag(110)(1×1) and Pt(110)(1×2) under grazing incidence ($\Psi = 3.1°, \Theta = 6.2°, \vartheta = 0°$) along high (◯) and low-indexed (△) directions.

low as for $[1\bar{1}0]$, they are appreciably higher for high-indexed incidence on the Ag(110) surface. Starting with minimal values for $E \to 0$, the molecular yield initially increases with the energy up to ~ 600 eV/atom and then decreases again.

This behavior changes completely when scattering from the insulating LiF surface. The molecular survival fraction which is plotted as a function of the primary energy in Fig. 3.10 shows a similar tendency as for N_2^+ on metals: The molecular yield at low

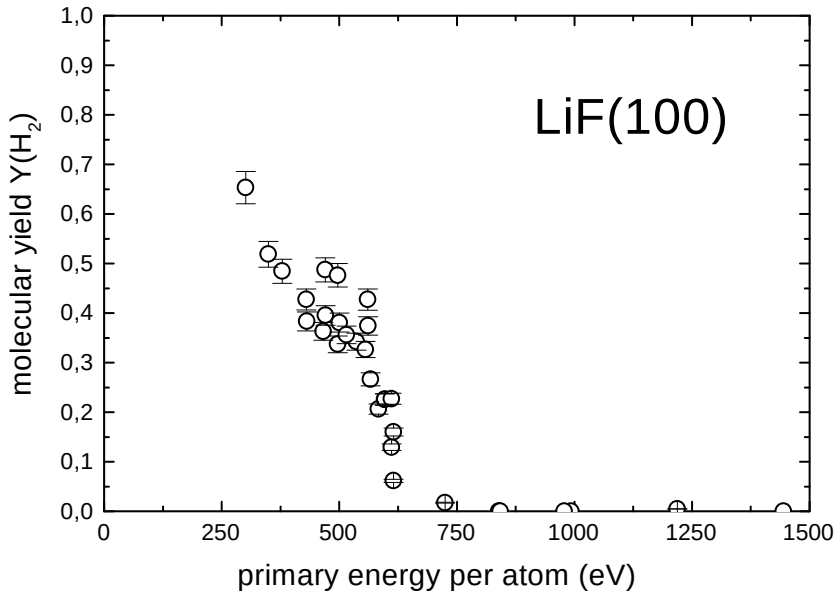

Figure 3.10: Molecular yields from scattering H_2^+ off LiF(100) under grazing incidence ($\Psi = 5°, \Theta = 10°, \vartheta = 0°$) along a high-indexed direction. [95].

energies is high and then decreases with increasing energy.

Chapter 4

Simulation

A helpful tool for a better understanding of the experimental results is the computer simulation of the scattering process. Widely spread on the field of particle-solid interaction are such programs as TRIM [100] or MARLOWE [101]. The underlying computational models in these applications treat the collision of the incoming projectile with target atoms within the Binary Collision Approximation (BCA), i.e., the scattering process is described as a sequence of binary collisions, based upon pair-potentials between the collision partners. This approach is only justified in case of atomic projectiles.

For molecular scattering in the studied energy range, a model based on an analytical six-dimensional potential energy surface (PES) has proven to yield good results [11, 16]. First structures of the program ScaDiM have been established in 1989 by Imke *et al.* [15]; the code was then further developed by Schlathölter and Vicanek [11]. It succeeded in qualitatively describing the scattering process of N_2 from Pd(111) via classical trajectory (CT) calculation.

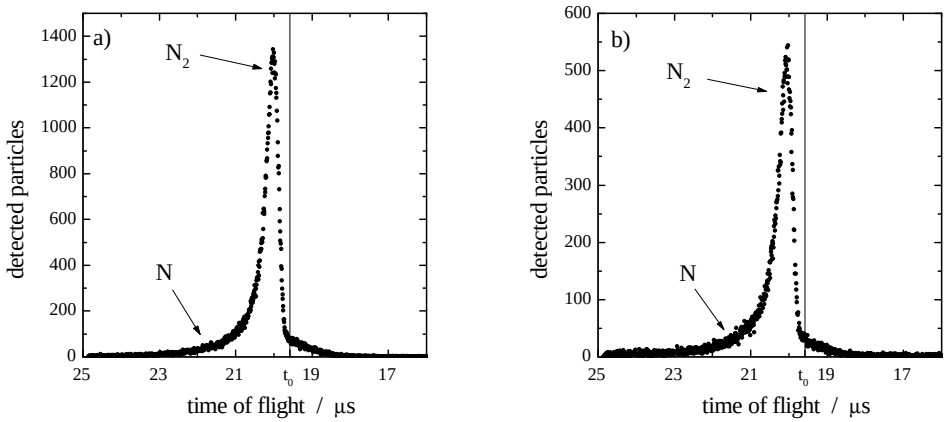

Figure 4.1: Time-of-flight spectra of 584 eV N_2^+ (a) and N_2 (b) scattered off Pd(111) under $\Psi = 5°$ and $\Theta = 10°$. The azimuthal direction is highly indexed. From [6].

ScaDiM does so far consider neither inelastic effects (cf. Sec. 1.1.3) nor electron exchange processes (cf. Sec. 1.1.2), making it inapplicable for simulating the correct dissociative behavior of H_2^+ scattered from metal surfaces. For nitrogen however, charge transfer processes are of minor importance for the dissociation process [4, 5, 6]. Fig. 4.1 compares the raw spectra resulting from time-of-flight experiments scattering N_2^+ and N_2 off Pd(111), respectively. No remarkable differences occur in the spectra, since the dissociation is only weakly influenced by the charge state of the projectile. As well, the work function of the target plays no important role in the dissociation process. This can be concluded from the experimental data plotted in Fig. 4.2, comparing the molecular yields of N_2^+ scattered off a clean and a potassium covered Pd(111) surface as a function of the primary energy. The dissociation probability is nearly the same in both cases. N_2 is therefore a perfect system for a direct comparison of the N_2^+ scattering experiments from Section 3.2 with purely classical simulations for neutral N_2.

4.1 Atomic Units

In atomic physics, measures are usually expressed in atomic units (a.u.). In contrast to the commonly used SI units, this leads to much more convenient orders of magnitudes of the values.

Atomic units directly result from Bohr's model, where elementary charge e, electron mass m_e, and Planck's constant $\hbar$ is set to unity, respectively. Consequently, the length unit equals the first Bohr's radius

$$1 \text{ a.u.} = a_0 = 0.529 \text{ Å} \tag{4.1}$$

and the energy unit is Hartree

$$1 \text{ a.u.} = 1 \text{ H} = 27.21 \text{ eV} \quad . \tag{4.2}$$

In the following sections, the system of atomic units will often be used for convenience.

4.2 Motivation

Preceding investigations [11, 16] predict on the base of ScaDiM simulations, that the dissociation of N_2 scattered off Pd(111) depends strongly on the azimuthal angle of incidence.
Qualitatively, these results are in agreement with the experimental results for the azimuthally resolved studies presented in the last chapter. However, a good quantitative agreement is not observed. Fig. 4.2 compares the experimental and simulational results as reported in the above references for the system N_2/Pd(111).

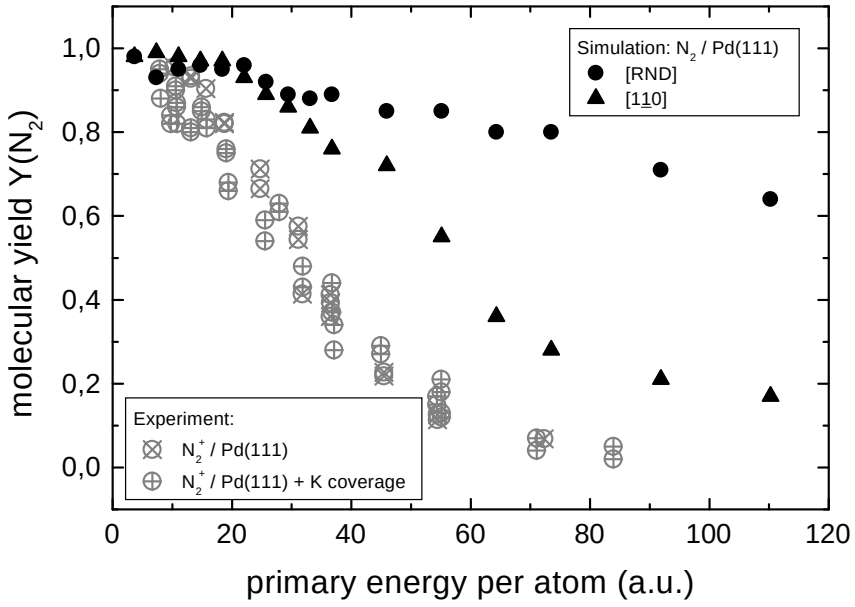

Figure 4.2: Molecular yields from scattering N_2^+ off Pd(111) under grazing incidence ($\Psi = 5°, \Theta = 10°, \vartheta = 0°$) for incidence along high (◯) and low-indexed (△) directions. Appropriate simulations are plotted as black symbols. In the experiment, a high-indexed direction is chosen. Negligible influence of the target work function is observed by comparing the results obtained from a clean and a K-covered surface. From [11, 16].

4.3 Current Model

ScaDiM is based on a classical calculation of the molecule-surface interaction. Basically, Newton's equations of motion are numerically solved along the trajectory of the molecule. The surface is built up chessboard-like by a periodically repeated lattice of 50×50 atoms in the corresponding geometry. No step or point defects are considered. A total depth of 5 layers is taken into account; the first layer atoms are each thermally displaced perpendicularly to the surface in terms of the Debye model. Therefore, a random number generator which produces Gaussian distributed values is weighted by the mean square atomic displacement which is proportional to $T/\theta_\perp$ (T is the surface temperature, set to 300 K, room temperature, throughout this work, and $\theta_\perp$ is the perpendicular component of the surface Debye temperature, according to Tab. 4.1). The parallel displacements are neglected considering the geometry of the scattering (grazing conditions).

The position of the molecule within the surface unit cell as well as its axis orientation is chosen randomly and the velocity is determined by the Gaussian-distributed primary

Surface	Pd(110)	Ag(110)	Pt(110)
$\theta_\perp$	191 K	142 K	167 K

Table 4.1: Debye temperatures $\theta_\perp$ (perpendicular components) of the investigated surfaces [102].

energy. A vibrational and rotational temperature of 600 K is assigned to the molecule, according to the models of the harmonic oscillator and the rigid rotator, respectively. These values are roughly estimated from the plasma temperature in the ion source. An extensive study of variable initial temperatures showed in [11, 16], that only the surface temperature has a noticeable influence on the interaction dynamics.

The forces acting on the molecular constituents are computed within the main Monte-Carlo loop. To this end, a set of differential equations has to be integrated numerically by means of a third order predictor-corrector method [103, 104, 105, 106]. In each integration step, the coordinates $r_i(t + \Delta t)$ are computed via

$$r_i\left(t + \Delta t\right) = r_i\left(t\right) + \Delta t \cdot v_i\left(t\right) + \frac{\Delta t^2}{6}\left(4a_i\left(t\right) - a_i\left(t - \Delta t\right)\right) \tag{4.3}$$

from the positions r_i, the velocities v_i, and the accelerations a_i at the times t and $t-\Delta t$. For the new $r_i(t + \Delta t)$, the $a_i(t + \Delta t)$ have to be determined (using the PES) and the new $v_i(t + \Delta t)$ are then given by

$$v_i\left(t + \Delta t\right) = v_i\left(t\right) + \frac{\Delta t}{6}\left(2a_i\left(t + \Delta t\right) + 5a_i\left(t\right) - a_i\left(t - \Delta t\right)\right) \quad . \tag{4.4}$$

Δt is the infinitesimal variable which has to be chosen in a way that the total energy of the system is conserved within a certain tolerance. A value in the order of some 10^{-17} s keeps the fluctuations below 2×10^{-3} a.u. [11].

The molecule-surface interaction is essentially described via six-dimensional potential energy surfaces (PES). They allow to describe both, the physisorption of the N_2-molecule and the chemisorption of the atomic nitrogen. Fig. 4.3 gives a schematical, one-dimensional illustration of the dissociative adsorption of a homonuclear diatomic molecule A_2 on a metal surface. In contrast to atomic nitrogen, N_2 does not chemisorb on the metals Pd, Ag, and Pt studied in this work [108].

The analytical PES, based on *ab initio* density functional theory (DFT) cluster calculations and empirical data, has the form

$$\mathbf{V} = \begin{pmatrix} V_1 & V_{12} \\ V_{21} & V_2 \end{pmatrix} \quad . \tag{4.5}$$

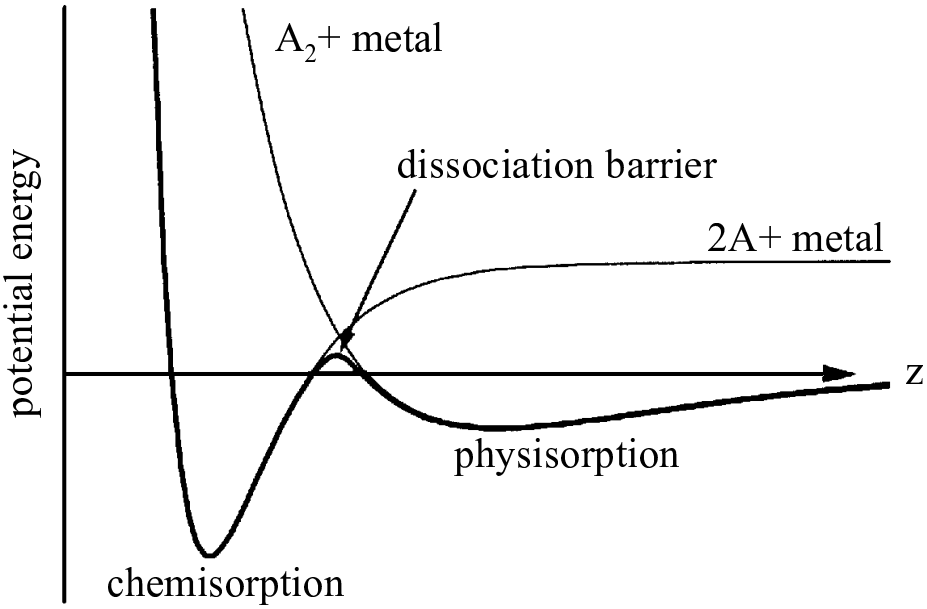

Figure 4.3: Schematical potential curves for a dissociative adsorption of an A_2-molecule on a metal surface (Lennard-Jones [107]).

V_1 embodies the diabatic N-Me PES, V_2 the diabatic N_2-Me PES (here and in the following, Me represents the corresponding target metal). The coupling terms must obey $V_{12} = V_{21}$ since the Hamiltonian is Hermitian. Diagonalization of $\mathbf{V}$ yields the adiabatic PES describing the ground state and an excited state of the N_2-Me system, where only the former is of interest here:

$$V(\mathbf{r}_1, \mathbf{r}_2) = \frac{1}{2}\left[V_1(\mathbf{r}_1, \mathbf{r}_2) + V_2(\mathbf{r}_1, \mathbf{r}_2) - \sqrt{(V_1(\mathbf{r}_1, \mathbf{r}_2) - V_2(\mathbf{r}_1, \mathbf{r}_2))^2 + 4V_{12}(\mathbf{r}_1, \mathbf{r}_2)^2}\right] \quad (4.6)$$

The $\mathbf{r}_i$ are the positions of the N_2 constituents. The diabatic interaction potential of the two N atoms with the surface atoms is assumed to be the sum of the repulsive N-N potential and binding N-Me potentials, which again is the sum of several dimer pair potentials:

$$V_1(\mathbf{r}_1, \mathbf{r}_2) = V_{\mathrm{N-N}}^{\mathrm{ZBL}}(r) + \sum_{i=1}^{2}\sum_{j=1}^{n} V_{\mathrm{N-Me}}(R_{ij}) \quad (4.7)$$

where r is the N-N distance, R_{ij} is the distance between the ith N atom and the jth metal atom, and n is the number of surface atoms interacting with the molecule. Since the N-N interaction is repulsive in this state, $V_{\mathrm{N-N}}^{\mathrm{ZBL}}$ is taken here (cf. Sec. 1.2.1).

Morse type potentials (s. Sec. 1.2.2) usually provide a good representation of the attractive part of the N-Me dimer interaction. For the pair-potentials $V_{\mathrm{N-Me}}(R_{ij})$, the Morse potentials are not sufficient to describe the small impact parameter interactions reached at higher beam energies. Here again, the ZBL potential describes the repulsive interaction for short distances $R_{ij} \to 0$ more exactly. In order to get a common representation with a smooth transition (at the distance R_0) between the high energy region via $V^{\mathrm{ZBL}}_{\mathrm{N-Me}}$ and the low energy part with the Morse potential

$$V^{\mathrm{Morse}}_{\mathrm{N-Me}}(R_{ij}) = D_{0,\mathrm{N-Me}} \left(1 - e^{-\alpha_{\mathrm{N-Me}}\left(R_{ij} - r_{0,\mathrm{N-Me}}\right)}\right)^2 \quad , \tag{4.8}$$

the following expression has been successfully applied in earlier studies [6, 11]:

$$\begin{aligned} V_{\mathrm{N-Me}}(R_{ij}) &= \frac{1 - \tanh(R_{ij} - R_0)}{2} \cdot V^{\mathrm{ZBL}}_{\mathrm{N-Me}}(R_{ij}) \\ &\quad + \frac{1 + \tanh(R_{ij} - R_0)}{2} \cdot V^{\mathrm{Morse}}_{\mathrm{N-Me}}(R_{ij}) \; . \end{aligned} \tag{4.9}$$

In the same way, the diabatic N_2-Me potential is defined as:

$$V_2(\mathbf{r}_1, \mathbf{r}_2) = V'^{\mathrm{Morse}}_{\mathrm{N-N}}(r) + \sum_{i=1}^{2} \sum_{j=1}^{n} V'_{\mathrm{N-Me}}(R_{ij}) \tag{4.10}$$

with

$$\begin{aligned} V'_{\mathrm{N-Me}}(R_{ij}) &= \frac{1 - \tanh(R_{ij} - R_0)}{2} \cdot V^{\mathrm{ZBL}}_{\mathrm{N-Me}}(R_{ij}) \\ &\quad + \frac{1 + \tanh(R_{ij} - R_0)}{2} \cdot V'^{\mathrm{Morse}}_{\mathrm{N-Me}}(R_{ij}) \end{aligned} \tag{4.11}$$

and

$$V'^{\mathrm{Morse}}_{\mathrm{N-Me}}(R_{ij}) = D'_{0,\mathrm{N-Me}} \left(1 - e^{-\alpha'_{\mathrm{N-Me}}\left(R_{ij} - r'_{0,\mathrm{N-Me}}\right)}\right)^2 \quad . \tag{4.12}$$

The N-N interaction is in this case attractive and can be described by a Morse potential (cf. Sec. 1.2.2):

$$V'^{\mathrm{Morse}}_{\mathrm{N-N}}(r) = D'_{0,\mathrm{N-N}} \left(1 - e^{-\alpha'_{\mathrm{N-N}}\left(r - r'_{0,\mathrm{N-N}}\right)}\right)^2 \quad . \tag{4.13}$$

Depending on which V_{12} is chosen for the final PES, the parameters $D'_{0,\mathrm{N-N}}$, $\alpha'_{\mathrm{N-N}}$, and $r'_{0,\mathrm{N-N}}$ have to be modified from the exact values for the N-N Morse potential [59] in

such a way that Eq. 4.6 results in the correct N-N interaction potential of gas phase N_2 for an infinite molecule-surface distance. This modification becomes necessary due to the hybridization of $V'^{\mathrm{Morse}}_{\mathrm{N-N}}$ and $V^{\mathrm{ZBL}}_{\mathrm{N-N}}$.
The coupling term V_{12} mainly influences the dissociation barrier between the physisorption and chemisorption state and stays as a free 'mixing'-parameter in the calculation:

$$V_{12} = \chi \tag{4.14}$$

Within a reasonable range, the choice of this parameter and therefore the form of the dissociation barrier is of minor importance for the results. This is expected for the system under study where the translational energies are in the keV range.

The parameters used in Eqs. 4.8 and 4.12 as well as R_0 are obtained by fitting V_1 and V_2 to the results of corresponding DFT cluster calculations using the commercial DFT software DMol [109] and experimental data. This procedure is worked out in the next section.

4.4 Construction of the PES

A complete PES for the system N_2/Pd(111) has already been constructed by Schlathölter *et al.* [11]. For reasons of simplicity, the set of parameters (summarized in Tab. 4.2) is adopted here for the system N_2/Pd(110).
For the surfaces Ag(110) and Pt(110), the procedure for the construction is described in the following.

R_0	$D_{0,\mathrm{N-Pd}}$	$\alpha_{\mathrm{N-Pd}}$	$r_{0,\mathrm{N-Pd}}$	$D'_{0,\mathrm{N-Pd}}$	$\alpha'_{\mathrm{N-Pd}}$	$r'_{0,\mathrm{N-Pd}}$	χ	$D'_{0,\mathrm{N-N}}$	$\alpha'_{\mathrm{N-N}}$	$r'_{0,\mathrm{N-N}}$
1.25	0.061	1.05	3.535	0.018	1.3	3.8	0.05	0.4225	1.398	2.059

Table 4.2: Parameters of the N_2/Pd(111) PES [11] (atomic units)

The main task in view of constructing the PES is the determination of the potentials V_1 (Eq. 4.7) and V_2 (Eq. 4.10). To treat the former one (the diabatic N-Me PES) in a first step, the correct parameters for Eqs. 4.8 and 4.9 have to be found. For this purpose, *ab initio* calculations with the commercial DFT software DMOL are performed in order to obtain reference values for the corresponding potentials.

First of all, the geometry of the target surface is approximated by a cluster of about 20...50 atoms arranged in the geometry of the surface under investigation. No relaxation effects are taken into account; the position of the metal atoms is strictly given by the bulk fcc-structure and the (110)-surface. For the Pt(110)-calculations, a 1×1-surface structure instead of the 'real' 1×2 is used considering the small size of the

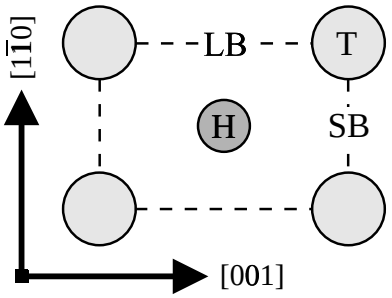

Figure 4.4: Typical adsorption sites on the fcc(110) surface: T = top or terminal site, H = hollow site, LB = long bridge site, SB = short bridge site. The big circles indicate the positions of first-layer atoms which form a surface unit cell, the small (darker) circle is a second-layer atom.

cluster.
In four geometries, a nitrogen atom is placed at a variable distance z over the adsorption sites top, short bridge, long bridge, and hollow (cf. Fig. 4.4).
For each adsorption site, the binding energies are calculated for several N-Pd$_n$ distances z.

These *ab initio* results are fitted by Eq. 4.7 under consideration of all 4 adsorption sites, as shown in Figs. 4.5 and 4.6 for the Ag(110) and Pt(110) surfaces, respectively. A good initial guess for the parameters $D_{0,\mathrm{N-Me}}$, $\alpha_{\mathrm{N-Me}}$, $r_{0,\mathrm{N-Me}}$ (for the Morse potential, Eq. 4.8), and the 'switching distance' R_0 (Eq. 4.9) can be obtained by first fitting V_1 to DFT binding energies for a simple N-Me dimer. These *ab initio* binding energies are quickly computed with DMOL, too.

Since density functional theory is a theory which describes only the ground state of a given system [112], it has to be noted that it cannot provide reliable results for very short distances. For this reason, the fit is performed for z-values greater than ~ 2 a.u. Furthermore, the binding energies obtained by these calculations are systematically slightly overestimated [11, 16]. An adjustment of $D_{0,\mathrm{N-Me}}$ is therefore performed in such way that the binding energy (which is considered to be found in the first local minimum along the potential curves for $z \to 0$) is in accordance with experimental values [110]. For the lack of respective data, the parameters $\alpha_{\mathrm{N-Me}}$ and $r_{0,\mathrm{N-Me}}$ are kept constant.

For the Pt surface, a slight inaccuracy must be taken into account at this stage. On the one hand, a cluster providing a 1×1- instead of the real 1×2-surface structure is used in the DFT- and fit-calculations; thus, pair-potentials obtained for the 1×1-geometry are used to construct the PES for simulating the reconstructed surface. On the other hand, literature values are only available for the adsorption on the Pt(111)-surface

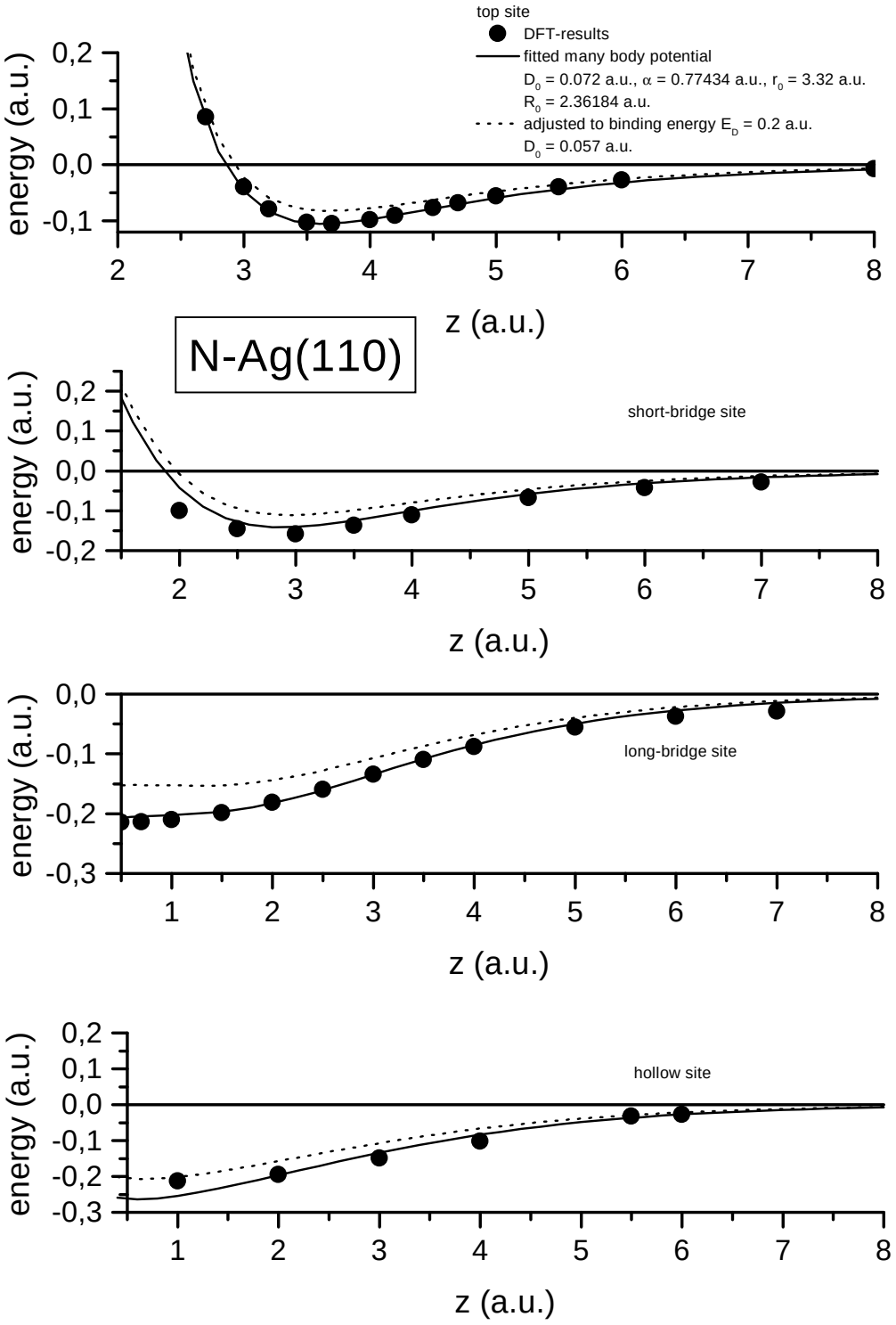

Figure 4.5: Binding energies for atomic nitrogen on Ag clusters representing the adsorption sites top, short bridge, long bridge, and hollow, according to Fig. 4.4. The results from DFT cluster calculations are plotted as circles, the N-Ag PES V_1 fit as solid lines. The dotted lines represent the PES after adjusting the binding energy (see text).

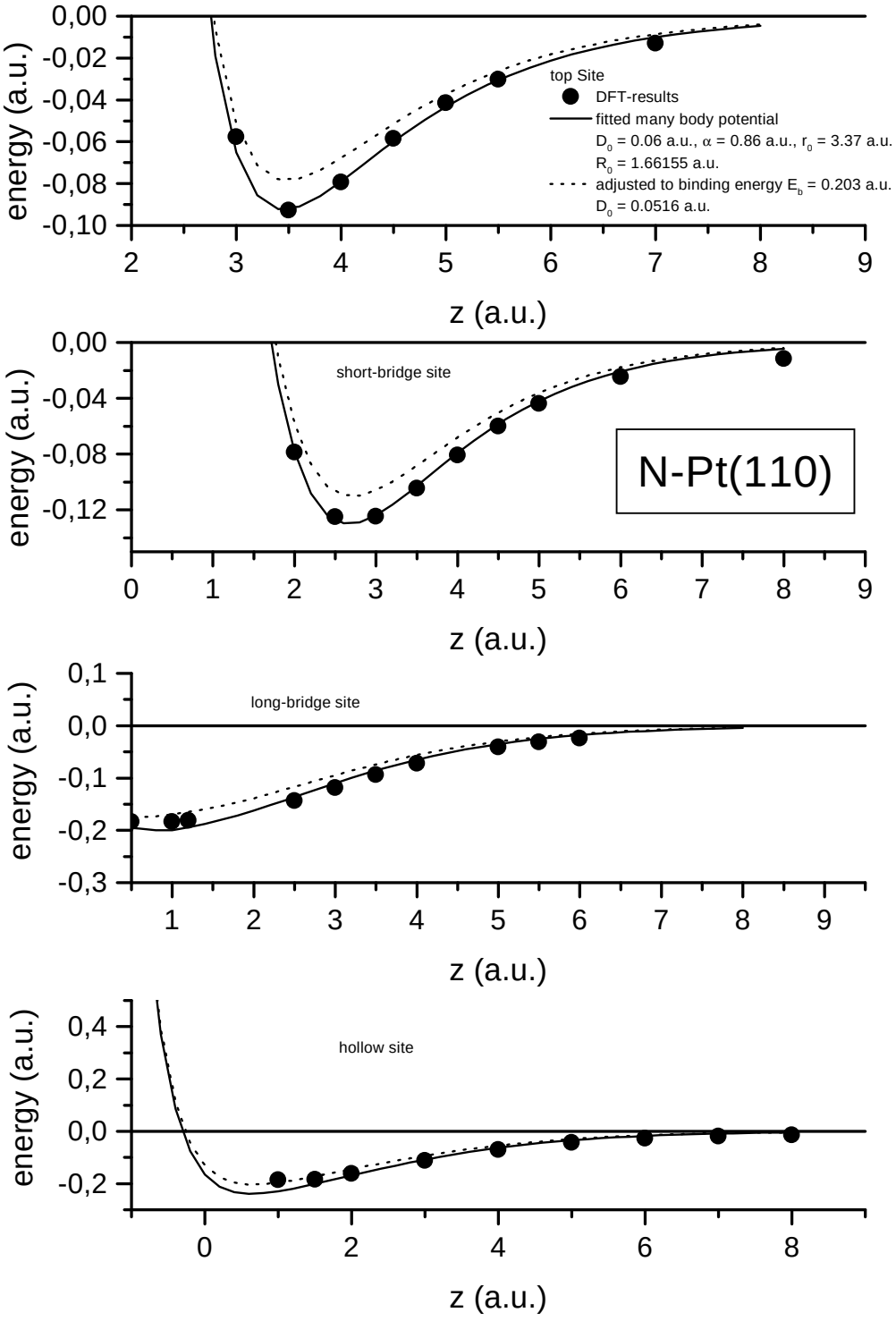

Figure 4.6: Binding energies for atomic nitrogen on Pt clusters. The results from DFT cluster calculations are plotted as circles, the N-Pt PES V_1 fit as solid lines. The dotted lines represent the PES after adjusting the binding energy according to [110, 111].

[110]. However, it is well-known for this material that the heat of adsorption does not vary much with the surface structure [111].

Consequently, the PES V_1 for the Ag(110) surface is determined by $D_{0,\mathrm{N-Ag}} = 0.057$, $\alpha_{\mathrm{N-Ag}} = 0.774$, and $r_{0,\mathrm{N-Ag}} = 3.32$, all in atomic units (s. Fig. 4.5). For Pt(110), the parameters are: $D_{0,\mathrm{N-Pt}} = 0.052$, $\alpha_{\mathrm{N-Pt}} = 0.86$, and $r_{0,\mathrm{N-Ag}} = 3.37$, according to Fig. 4.6.

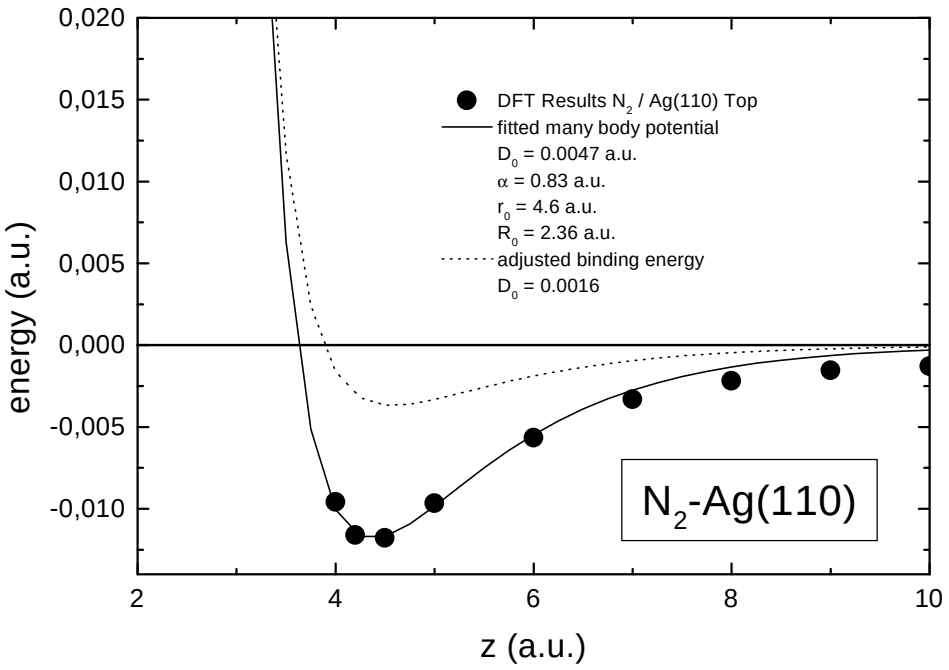

Figure 4.7: Binding energies for a physisorbed N_2 on an Ag cluster in a top site. z is the distance between the surface and the lowest N atom of the perpendicularly oriented molecule. The results from DFT cluster calculations are plotted as circles, the fitted N_2-Ag PES V_2 as a solid line. The dotted line represents the PES with adjusted binding energy.

As reported in [11], the choice of R_0 does not substantially affect the simulation results. From the above fitting procedure, it is determined as $R_0 = 2.36$ a.u. for Ag(110) and $R_0 = 1.66$ a.u. for Pt(110). A complete overview of the parameters will be given in Tabs. 4.4 and 4.5 at the end of this section.
The repulsive ZBL potential of the N-N interaction, which is necessary for the final construction of V_1, is described in Sec. 1.2.1.

For the diabatic N_2-Me PES V_2, a similar strategy as for V_1 is used. However, the number of degrees of freedom does not allow to calculate a complete PES by means of DFT.

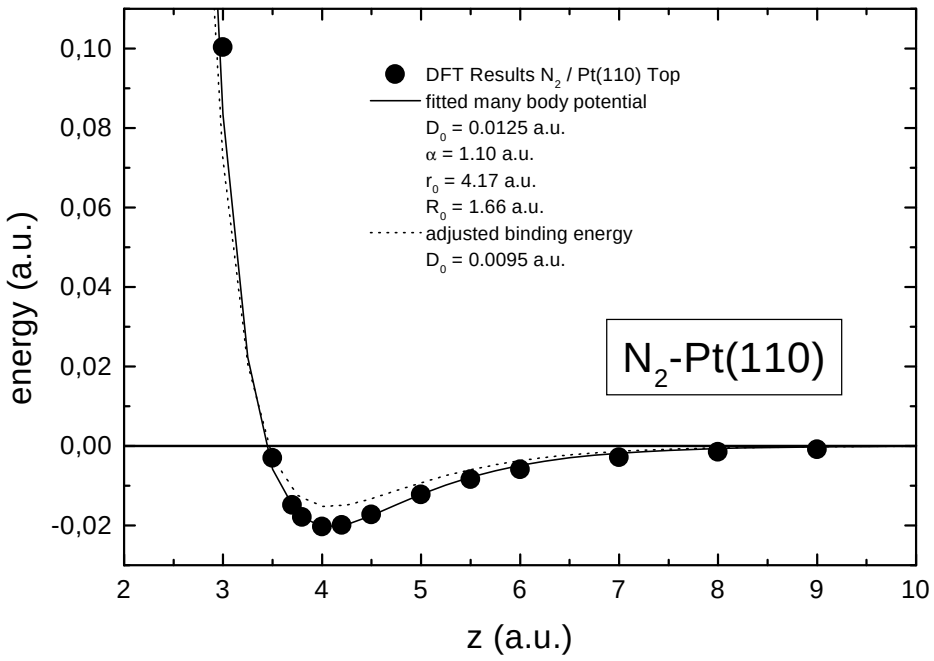

Figure 4.8: Binding energies for a physisorbed N_2 on a Pt cluster. See description under Fig. 4.7 for details.

Following the example in [11, 16], the physisorption system is therefore studied for an upright oriented, on top adsorbed N_2 molecule on the metal cluster. The intramolecular distance is kept constant at the N_2 gas phase equilibrium distance. Figs. 4.7 and 4.8 show the resulting energies as a function of the surface distance for N_2/Ag(110) and N_2/Pt(110), respectively.

Again, the adsorption energies have to be adjusted in order to comply with experimental values, though only approximate binding energies are available for N_2/Ag (about 0.1 eV [113]) and for N_2/Pt (0.41 eV for the (111)-surface [114]). Nevertheless, a correction of the *ab initio* DFT results towards lower binding energies has always to be expected to be necessary [11, 16].

The resulting parameters for the PES V_2 according to Eqs. 4.10–4.13 in atomic units are: $D'_{0,\mathrm{N-Ag}} = 0.0016$, $\alpha'_{\mathrm{N-Ag}} = 0.83$, and $r'_{0,\mathrm{N-Ag}} = 4.6$ for the Ag(110) surface and $D'_{0,\mathrm{N-Pt}} = 0.0095$, $\alpha'_{\mathrm{N-Pt}} = 1.10$, and $r'_{0,\mathrm{N-Pt}} = 4.17$ for the Pt(110) surface.

Only missing in the final PES (Eq. 4.5) is the coupling term V_{12}, i.e., the mixing parameter χ, which describes the magnitude of coupling between the two diabatic PES V_1 and V_2. For the lack of respective data, as in [11, 16], χ is handled as a free para-

χ	$D'_{0,\mathrm{N-N}}$	$\alpha'_{\mathrm{N-N}}$	$r'_{0,\mathrm{N-N}}$
0	0.3638	1.422	2.075
0.025	0.395	1.409	2.066
0.05	0.4225	1.398	2.059
0.1	0.469	1.380	2.049

Table 4.3: Parameters for Eq. 4.13 for different mixing parameters χ (atomic units). The values for $\chi = 0$ are representative for the free N_2 molecule.

meter. It was already reported in these references and at the end of Section 4.3, that the parameters of Eq. 4.13 have to be altered with respect to the choice of χ. Tab. 4.3 summarizes the Morse potential parameters for the free N_2 molecule ($\chi = 0$) as well as for three different arbitrary mixing parameters $\chi = 0.025, 0.05$, and 0.1 a.u.

First attempts to apply ScaDiM with the above constructed PES for the Pd(110), Ag(110), and Pt(110)(1×2) surfaces leads to the results plotted in Fig. 4.9: The simulated molecular yields are largely inconsistent with the experimental data. A variation of the mixing parameter within a reasonable range does not improve this result.

It has already been reported in [11, 16] that no quantitative agreement can be expected due to the neglect of inelastic processes in the simulations. However, in contrast to the results presented there, not even a qualitative agreement is achieved for the (110)-surfaces of this work: Especially in case of the $[1\bar{1}0]$-direction, the molecular yield as a function of E_0 is very poorly reproduced. Over a large energy range, the calculated molecular survival probability is higher than for the high-index case, just opposite to the experiment (s. Fig. 4.9).

Obviously, with the current model the simulations are not able to provide satisfying results. An important part of the molecule-surface interaction seems to be neglected in the purely classical description of the scattering process so far. However, it will be shown in the following, that the model can be significantly improved by introducing a weakening of the intramolecular bond as a function of the electron density of the surface sampled by the N_2.

The choice of the mixing-parameter χ within a reasonable range turns out to be of minor importance for the simulations. In order to reduce the number of free parameters, it is kept fixed at the value 0.05 a.u., as also proposed in the above mentioned references. A final summary of all parameters used for the N_2/Ag(110)- and N_2/Pt(110)-PES is presented in Tabs. 4.4 and 4.5, respectively.

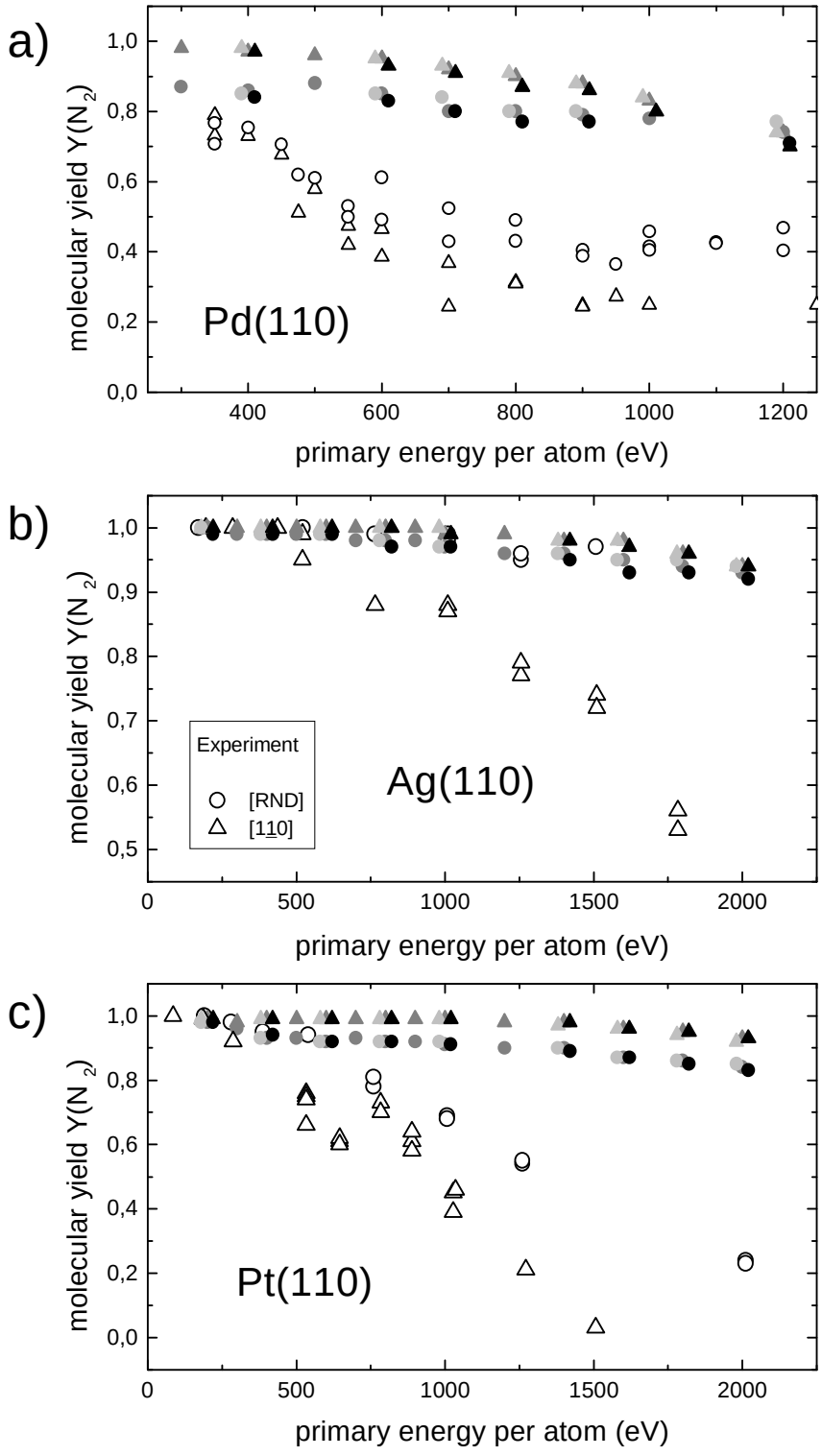

Figure 4.9: Comparison of experimental (open symbols) and simulated (full symbols) molecular yields of N_2 scattered off a) Pd(110), b) Ag(110), and c) Pt(110). Note the different scaling of the axes. Circles (◯) represent high-indexed incidence and triangles (△) along the $[1\bar{1}0]$-direction. The three different mixing parameters from Tab. 4.3 are used in the simulations: $\chi = 0.025$ a.u. is plotted in light gray, $\chi = 0.05$ a.u. in gray, and $\chi = 0.1$ a.u. in black symbols.

R_0	$D_{0,\mathrm{N-Ag}}$	$\alpha_{\mathrm{N-Ag}}$	$r_{0,\mathrm{N-Ag}}$	$D'_{0,\mathrm{N-Ag}}$	$\alpha'_{\mathrm{N-Ag}}$	$r'_{0,\mathrm{N-Ag}}$	χ	$D'_{0,\mathrm{N-N}}$	$\alpha'_{\mathrm{N-N}}$	$r'_{0,\mathrm{N-N}}$
2.362	0.057	0.774	3.32	0.0016	0.83	4.6	0.05	0.4225	1.398	2.059

Table 4.4: Parameters of the N_2/Ag(110)-PES (atomic units)

R_0	$D_{0,\mathrm{N-Pt}}$	$\alpha_{\mathrm{N-Pt}}$	$r_{0,\mathrm{N-Pt}}$	$D'_{0,\mathrm{N-Pt}}$	$\alpha'_{\mathrm{N-Pt}}$	$r'_{0,\mathrm{N-Pt}}$	χ	$D'_{0,\mathrm{N-N}}$	$\alpha'_{\mathrm{N-N}}$	$r'_{0,\mathrm{N-N}}$
1.662	0.0516	0.86	3.37	0.0095	1.10	4.17	0.05	0.4225	1.398	2.059

Table 4.5: Parameters of the N_2/Pt(110)-PES (atomic units)

4.5 Improving the Model

A known disadvantage of the current model – as already reported in [11, 16] – is the neglect of the explicit dependence of the N-N bond strength on the local electron density at the surface, due to the lack of experimental and/or theoretical data. It is therefore worthwhile to improve the simulation by explicitly including a static weakening of the intramolecular bond as a function of the distance to the surface.
This weakening reflects the screening action of metal conduction band electrons and it might play an important role in the dissociation process of the systems under study (cf. Sec. 1.2.3).

Henriksen *et al.* in their work on the dissociative chemisorption of N_2 on rhenium [60] use a similar approach as the model described in the last section but with an additional coordinate-dependent parameter $D'_{\mathrm{N-N}}(R_{ij})$ replacing $D'_{0,\mathrm{N-N}}$ in Eq. 4.13, i.e., a static weakening depending on the distance between the molecule and the surface atoms. The two other parameters in Eq. 4.13 are expected to be only weakly dependent on R_{ij} and therefore kept constant.

Since this work deals with projectiles of much higher translational energies, the lateral change of the surface electron density when moving mainly parallel to the surface can be expected to average out. Therefore, $D'_{\mathrm{N-N}}$ can be treated as a function of the molecule-surface distance z only:

$$D'_{\mathrm{N-N}}(z) = D'_{0,\mathrm{N-N}}\left(1 - D_{\mathrm{soft}} \cdot e^{-\alpha_{\mathrm{soft}} \cdot z}\right) \tag{4.15}$$

and therefore, Eq. 4.13 changes to

$$V'^{\mathrm{Morse}}_{\mathrm{N-N}}(r,z) = D'_{\mathrm{N-N}}(z)\left(1 - e^{-\alpha'_{\mathrm{N-N}}\left(r - r'_{0,\mathrm{N-N}}\right)}\right)^2 . \tag{4.16}$$

$D'_{0,\mathrm{N-N}}$ is the binding energy of the gas-phase N_2 for an infinite molecule-surface distance according to the conditions described in Section 4.3. D_{soft} and α_{soft} are new

parameters which (for instance) arise from DFT calculations as described in the next section.

With this small modification, an effective softening of the intramolecular bond is computed in each integration step along the trajectory of the molecule. Neither lateral structure information nor time-dependent relaxation effects are taken into account.

The additional processing of the bond weakening makes the algorithm more complex and, as a consequence, the total time consumed by the simulation increases noticeable with this change. In the end, the time is the limiting factor for the accuracy of the simulational results. A compensating speedup however was achieved on our machines (IBM SP/2-Cluster) after optimizing and completely converting the ScaDiM source code from *Fortran* into *C* in the course of this thesis.

4.6 Determination of the Softening Effect

To get a first impression of the effect of a z-dependent intramolecular bond, the new model is tested on the system N_2/Pd(111) studied in Ref. [11, 16]. The PES is already known from this work and the parameters are listed in Tab. 4.2. The only thing to do, as for the three other (110)-systems, is to find the softening parameters for Eq. 4.15. For the lack of experimental or theoretical data, to this end *ab initio* DFT cluster calculations are performed to estimate the N-N binding energies $D_{\mathrm{N-N}}$ at different molecule-surface distances z.

A procedure similar to the one for computing the N-Me and N_2-Me interaction potentials (cf. Sec. 4.4) is used: The surface is approximated by substrate clusters. The nitrogen molecule is now placed with its axis lying parallel to the cluster 'surface' at a given distance z. Two adsorption sites are probed for the (110)-surfaces: the top site and the hollow site; only the top site is used for Pd(111) since this is a closely packed surface and the differences between the adsorption sites are not expected to vary much. The values obtained for the top sites are upper limits for the effective screening effect since the local electron density is highest for a given z at that position.
For each adsorption site, two molecule orientations are examined: the molecule is either oriented with its axis parallel to the $[1\bar{1}0]$-direction or perpendicular to that. For each given adsorption site, molecule orientation, and surface distance z, the total energy of the system is calculated for different intermolecular N-N distances r using the commercial DFT software DMol [109]. The results of each study can then be fitted by Morse type potentials as described by Eq. 4.16.

Fig. 4.10 shows the result for the first system, N_2/Pd(111). Eq. 4.15 is used in this plot for fitting the *ab initio* $D_{\mathrm{N-N}}(z)$. It is clearly seen from the plot, that the softening of the molecular bond is not sensitive to the lateral orientation of the molecule (for this

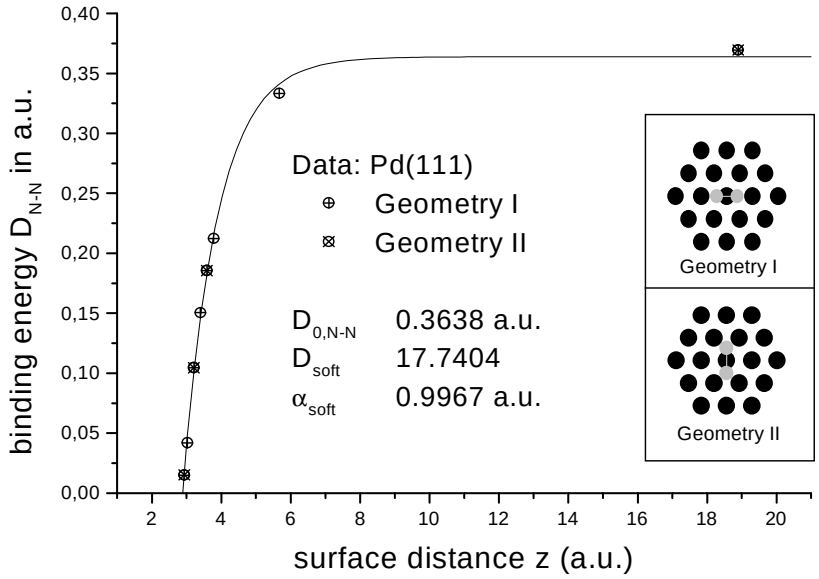

Figure 4.10: Calculated N-N binding energies as a function of the molecule-surface distance on Pd(111). z is measured from the plane of the first layer atoms of the surface. The molecule is placed upon a top site, 'lying' parallel to the surface with its axis oriented along $[1\bar{1}0]$ (geometry I) and [001] (geometry II), respectively. The curve is a fit using Eq. 4.15.

adsorption site). Indeed, also the results for N_2 on top sites of the Pd(110) (Fig. 4.11a), Ag(110) (Fig. 4.11c), and Pt(110) surfaces (Fig. 4.11e) show no remarkable difference between the two orientations with respect to the $[1\bar{1}0]$-chains.
However, when the molecule is placed upon a hollow site, a slight divergence of the $D_{\mathrm{N-N}}(z)$ becomes apparent for small z-values, due to the distortion caused by the surface top row atoms (Figs. 4.11b, d, and e). As a consequence, this model which neglects any lateral dependency is expected to have a weakpoint in describing the interaction in particular for scattering along the $[1\bar{1}0]$ surface-channels at high (perpendicular) velocities (small impact parameters).

In analogy to Sec. 4.4, the 1×1-surface structure instead of the 'real' 1×2 is used for the Pt(110)-calculations (Figs. 4.11e and f) considering the small cluster size.

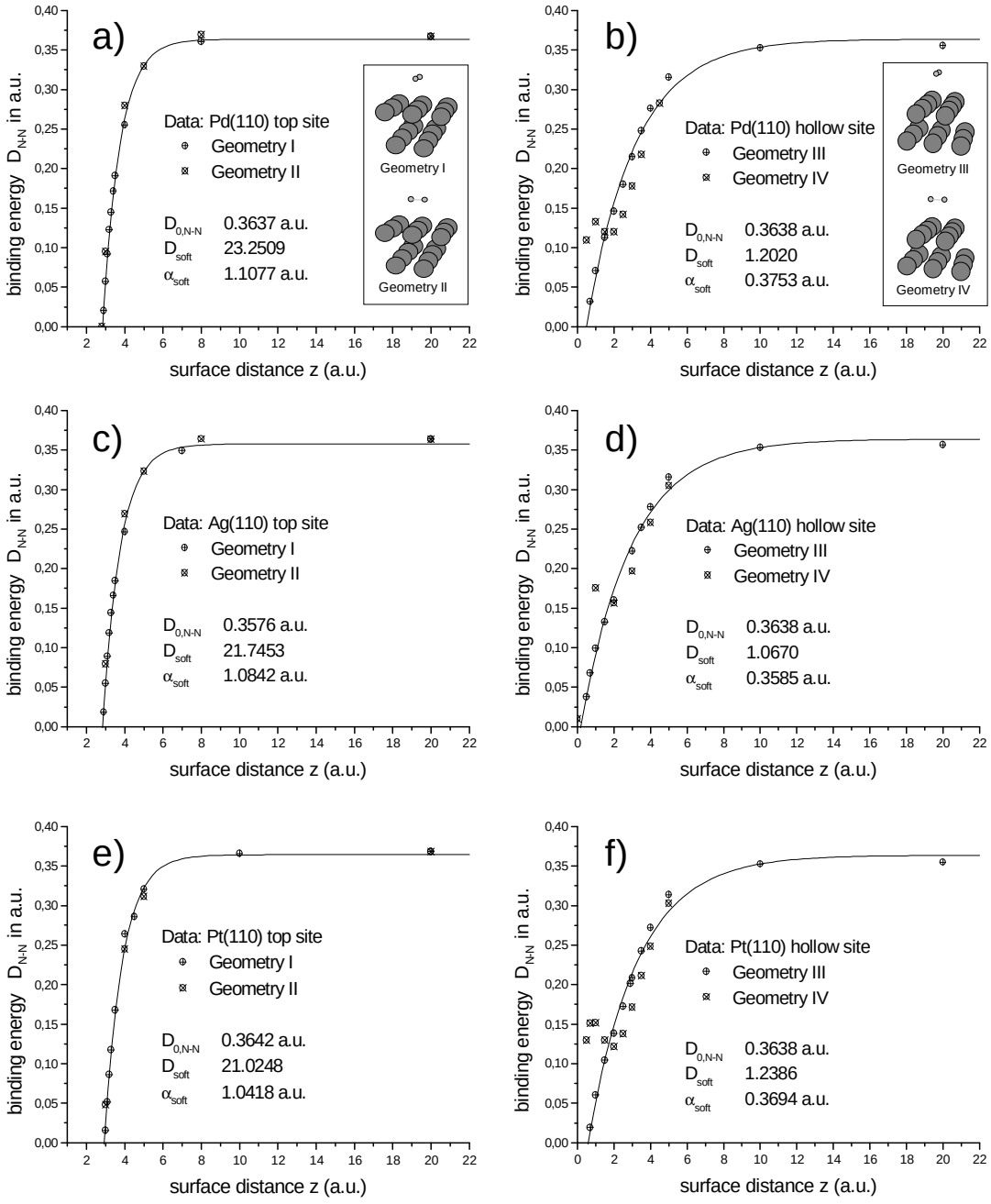

Figure 4.11: Calculated N-N binding energies of a nitrogen molecule adsorbed on Pd, Ag, and Pt(110) surfaces. Adsorption sites are 'top' (a, c, and e) and 'hollow' positions (b, d, and f). The molecular axis lies parallel to the $[1\bar{1}0]$-direction (geometry I and III) or to the [001]-direction (geometry II and IV) as illustrated in the insets. The curve is a fit using Eq. 4.15.

4.7 Results

4.7.1 N_2/Pd(111)

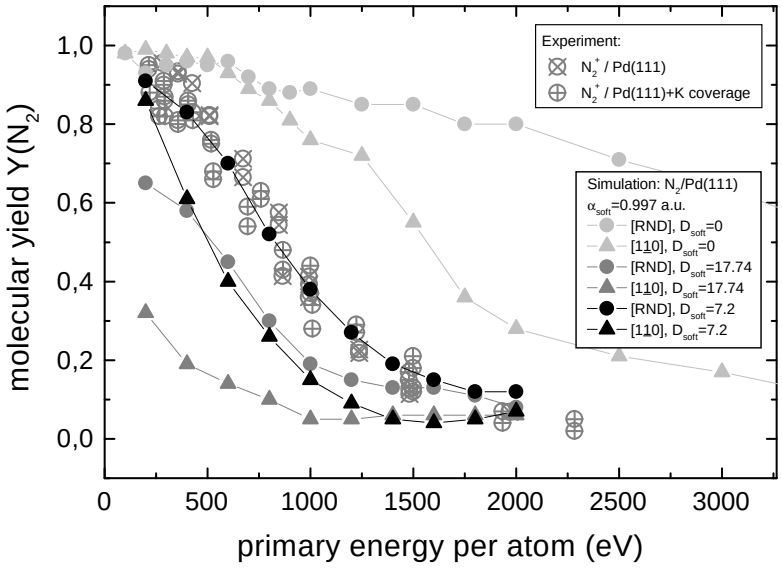

Figure 4.12: Molecular yields from N_2 scattering off Pd(111) (experimental data are taken from [11, 16]) under grazing incidence ($\Psi = 5°, \Theta = 10°, \vartheta = 0°$). Simulations (full symbols connected with lines to guide the eye) are made using the 'new' model with different softening parameters D_{soft} (see text); circles are used for high-indexed directions, triangles indicate scattering along $[1\bar{1}0]$. The case $D_{\text{soft}} = 0$ (light gray symbols) has already been discussed [11, 16]. $D_{\text{soft}} = 17.74$ is the static softening (gray symbols) obtained from *ab initio* DFT calculations for a top adsorption site (s. Sec. 4.6). Best agreement is observed with the effective parameter $D_{\text{soft}} = 7.2$ (random direction).

This system has been studied in detail previously [11, 16] and is reexamined here, to have a comparison of results obtained with and without the softening model. The parameters used for the PES are presented in Table 4.2.

Fig. 4.12 shows the experimental molecular yields of N_2 scattered off Pd(111) as a function of the energy, compared with CT results obtained with three different softening parameters. A high-indexed crystallographic direction is chosen in the experiment, which for the (111)-structure can be found at e.g. $\varphi = 35°$.

The first set of calculations (light gray symbols) is identical to the results from Refs. [11, 16] and corresponds to $D_{\text{soft}} = 0$ in the new model. Obviously, the simulated dissocia-

tion efficiency of the N_2 molecules is too low.
The CT results based on the softening parameters $D_{\mathrm{soft}} = 17.74$ and $\alpha_{\mathrm{soft}} = 0.997$ a.u. as obtained in the previous section are displayed as gray symbols in the same figure. As expected, the dissociation efficiency is too high when adopting these maximum values. Good agreement with the experimental results is found when lowering D_{soft} to an effective value of 7.2 while keeping $\alpha_{\mathrm{soft}} = 0.997$ a.u. (black symbols). This 'effective' softening parameter $D_{\mathrm{soft}} = 7.2$, obtained by fitting, describes the average screening assigned to the molecule.

4.7.2 N_2/Pd(110)

The first (110)-surface investigated with the modified code is chosen to be Pd(110). Since it is based on the same lattice as the Pd(111) surface, for reasons of simplicity the parameters from Table 4.2 are used for this system again.

The calculated results are compared to the experimental ones in Fig. 4.13. As for all (110)-faces, the high-indexed direction (labeled with [RND]) is found at $\varphi = 45°$.

Using $D_{\mathrm{soft}} = 0$, i.e., the 'old' model as in Sec. 4.4, the dissociation efficiency is too low. With the static softening parameters from Figs. 4.11a/4.11b, the screening is slightly over- (Fig. 4.13a) and underestimated (Fig. 4.13b), respectively.
Best agreement is achieved when either lowering the effective D_{soft} from 23.25 (acc. to Fig. 4.11a) to 12.2 with $\alpha_{\mathrm{soft}} = 1.108$ a.u. (Fig. 4.13a), or when raising it from 1.20 (acc. to Fig. 4.11b) to 1.52 with $\alpha_{\mathrm{soft}} = 0.375$ a.u. (Fig. 4.13b).

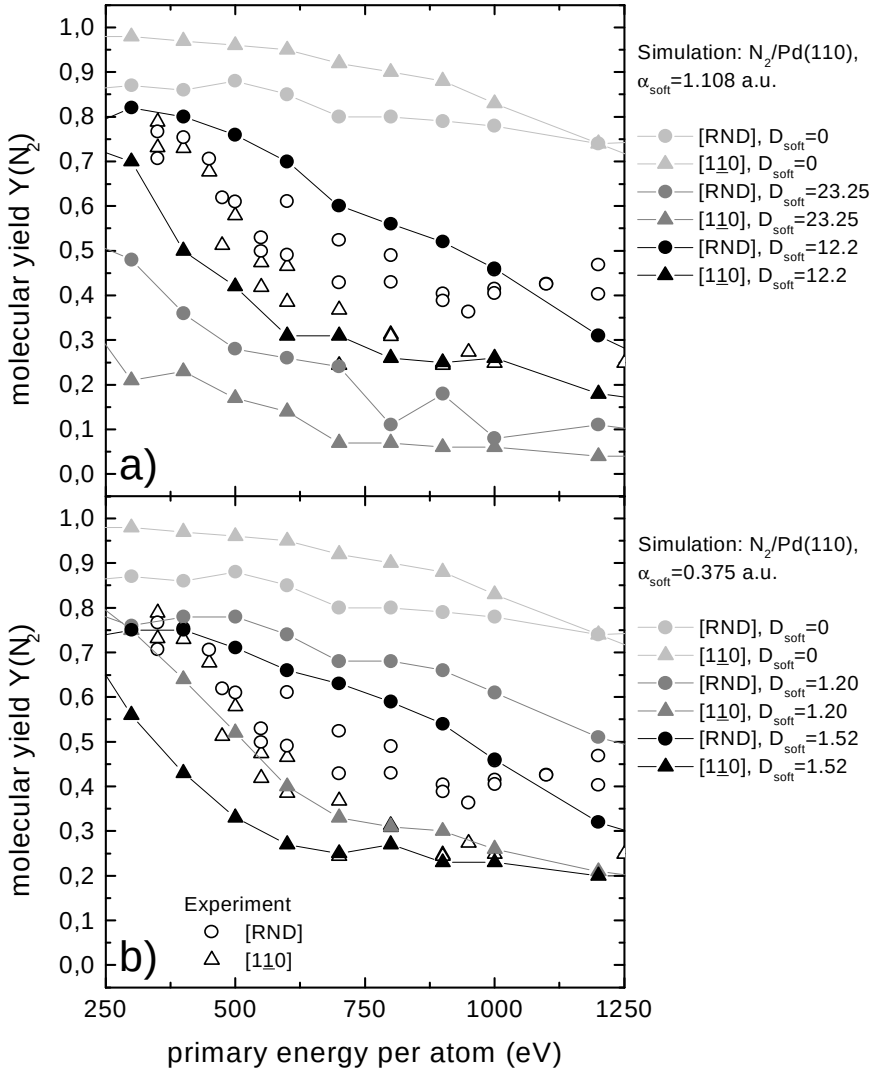

Figure 4.13: Molecular yields from N_2 scattering off Pd(110) (cf. Fig. 3.4) for high-indexed directions (circles) and scattering along $[1\bar{1}0]$ (triangles). The simulations (full symbols) are made with different softening parameters: $D_{\text{soft}} = 0$ (light gray) reflects the 'old' model calculations as from Sec. 4.4. When switching to the 'new' model ($D_{\text{soft}} > 0$), the agreement improves qualitatively and quantitatively (gray and black symbols). In a), the α_{soft} from Fig. 4.11a, in b) from Fig. 4.11b is used.

4.7.3 N_2/Ag(110)

The interaction of N_2 with the Ag and Pt surfaces is studied under more grazing incidence than in the respective study of Pd surfaces. Instead of $\Psi = 5°$ and $\Theta = 10°$ we now use $\Psi = 3.1°$ and $\Theta = 6.2°$, respectively, in order to reduce the perpendicular component of the velocity.
Fig. 4.14 shows the comparison between experiment and simulation for Ag(110). The

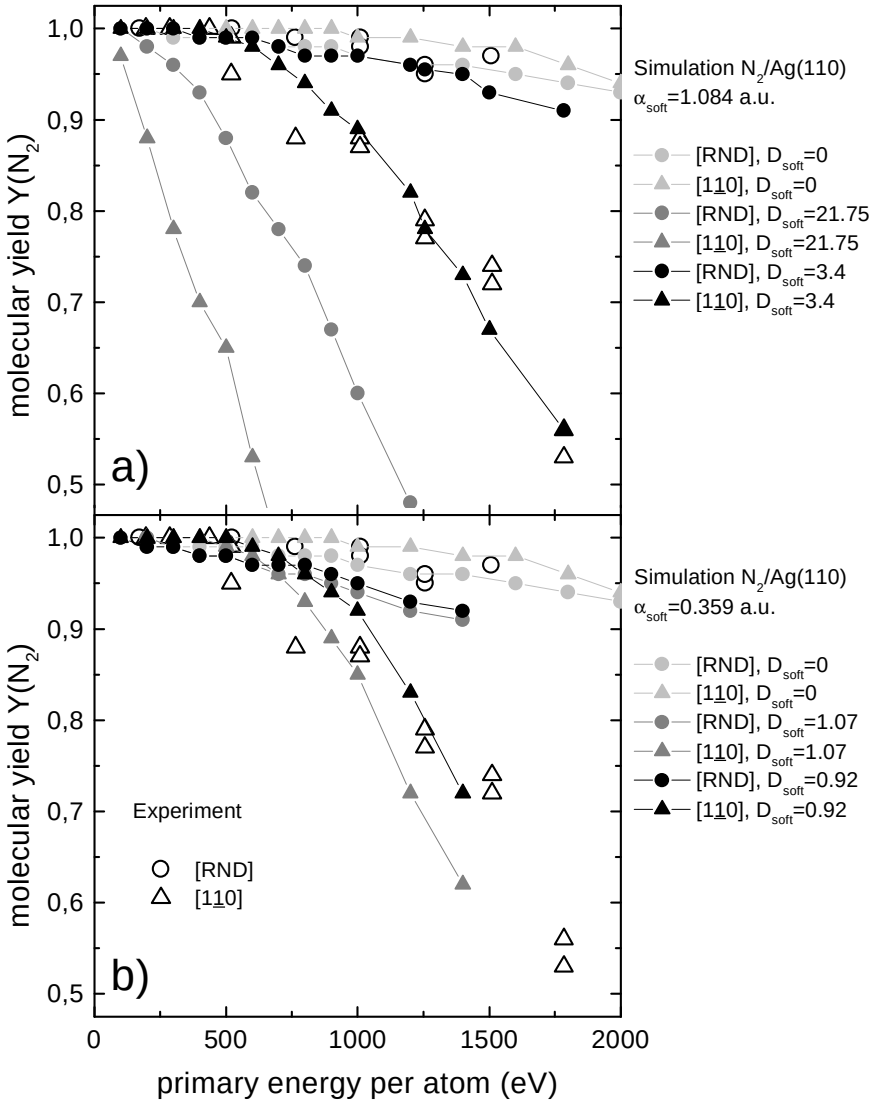

Figure 4.14: Molecular yields from scattering N_2 off Ag(110) (cf. Fig. 3.3). The symbols are the same as explained in Fig. 4.12. In a), the initial softening parameters from Fig. 4.11c (top site), in b) from Fig. 4.11d (hollow site) are used.

parameters determined for the N_2/Ag(110)-PES are given in Tab. 4.4.

Using the static softening parameters from Figs. 4.11c/4.11d, the dissociation becomes too strong.
A good compromise is found with $D_{\text{soft}} = 3.4$ for calculations using $\alpha_{\text{soft}} = 1.084$ a.u. from top site adsorption as taken from Fig. 4.11c.
For the adjusted hollow site softening parameter $D_{\text{soft}} = 0.92$ with $\alpha_{\text{soft}} = 0.359$ a.u. from Fig. 4.11d, the agreement is worse (cf. Fig. 4.14b). This cannot be improved using the hollow site α_{soft} and further adjustment of D_{soft}.

4.7.4 N_2/Pt(110)

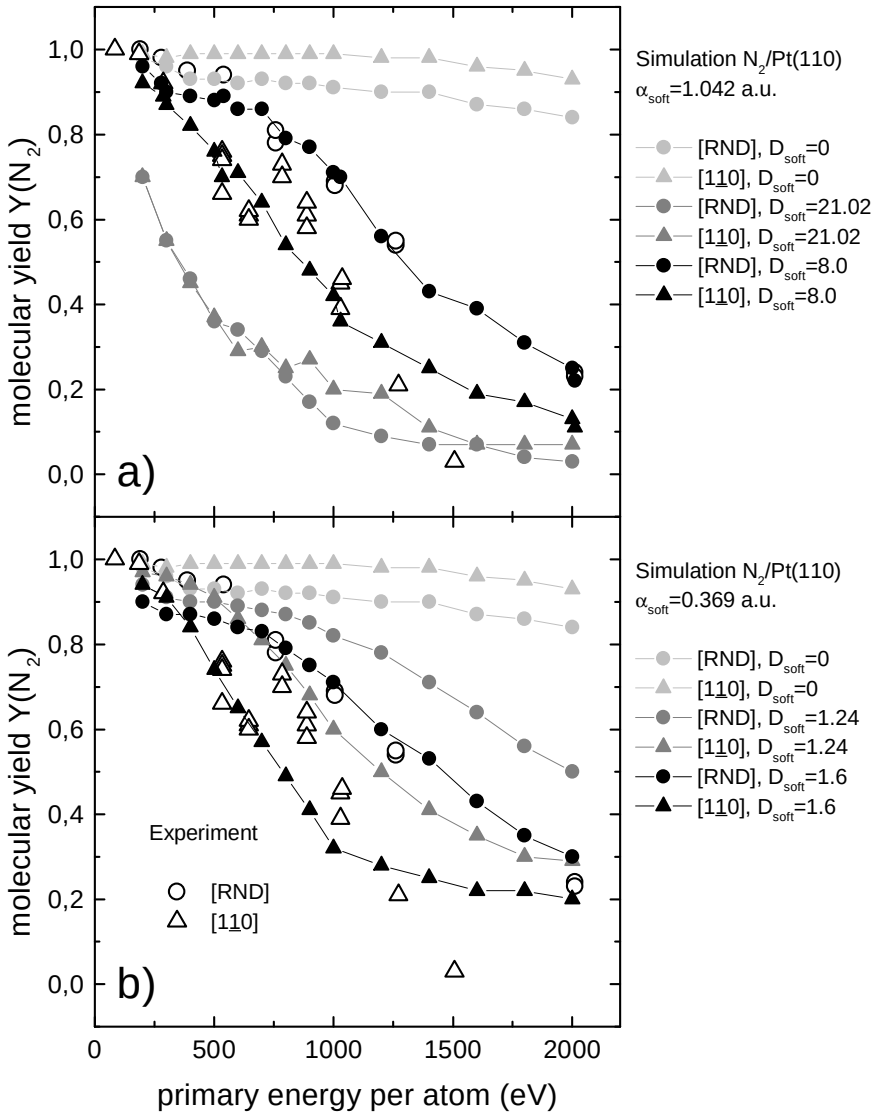

Figure 4.15: Molecular yields from scattering N_2 off Pt(110)(1×2) (cf. Fig. 3.3). The symbols are chosen as explained under Fig. 4.12. In a), the initial softening parameters from Fig. 4.11e (top site), in b) from Fig. 4.11f (hollow site) are used.

As mentioned earlier, Pt(110) plays a special role in this work, since the properly prepared surface is 1×2-reconstructed in the missing-row structure, in contrast to the other surfaces under study which are not reconstructed at room temperature.
In the experiments, higher molecular fragmentation is observed, and the difference between incidence along the high-indexed and the $[1\bar{1}0]$-direction is not as pronounced as for the Ag(110) surface under the same conditions (cf. Sec. 3).

The simulations reflect this behavior. Fig. 4.15 shows that the best description is achieved when either lowering the effective D_{soft} from 21.02 (acc. to Fig. 4.11e) to 8.0 with $\alpha_{\mathrm{soft}} = 1.042$ a.u. (Fig. 4.15a), or when raising it from 1.24 (acc. to Fig. 4.11f) to 1.6 with $\alpha_{\mathrm{soft}} = 0.369$ a.u. (Fig. 4.15b).

Again it turns out, that the former case (the softening parameter calculated for the geometry where the molecule is adsorbed on a top site) generally leads to a better agreement than using the softening parameters from the hollow site geometry as in Fig. 4.15b. For this reason, the parameters from Fig. 4.15a are used for the further calculations.

The next step is to examine the reproducibility of the angular dependence of the fragmentation as displayed in Fig. 3.5. The according results from the simulations can be found in Fig. 4.16.
An almost perfect agreement over the whole angular range is found for the $[1\bar{1}0]$-incidence scattering; for the random case, however, the description merely matches for the low angle range. When assuming a 'fictitious' Pt(110) surface with a 1×1-structure instead of 1×2, which is very easy in a simulation, the calculations obviously lead to a better agreement. Confirmed by the LEED analysis (cf. Sec. 2.3.3) there is no doubt that the experimentally investigated Pt(110) surface is 1×2-reconstructed.

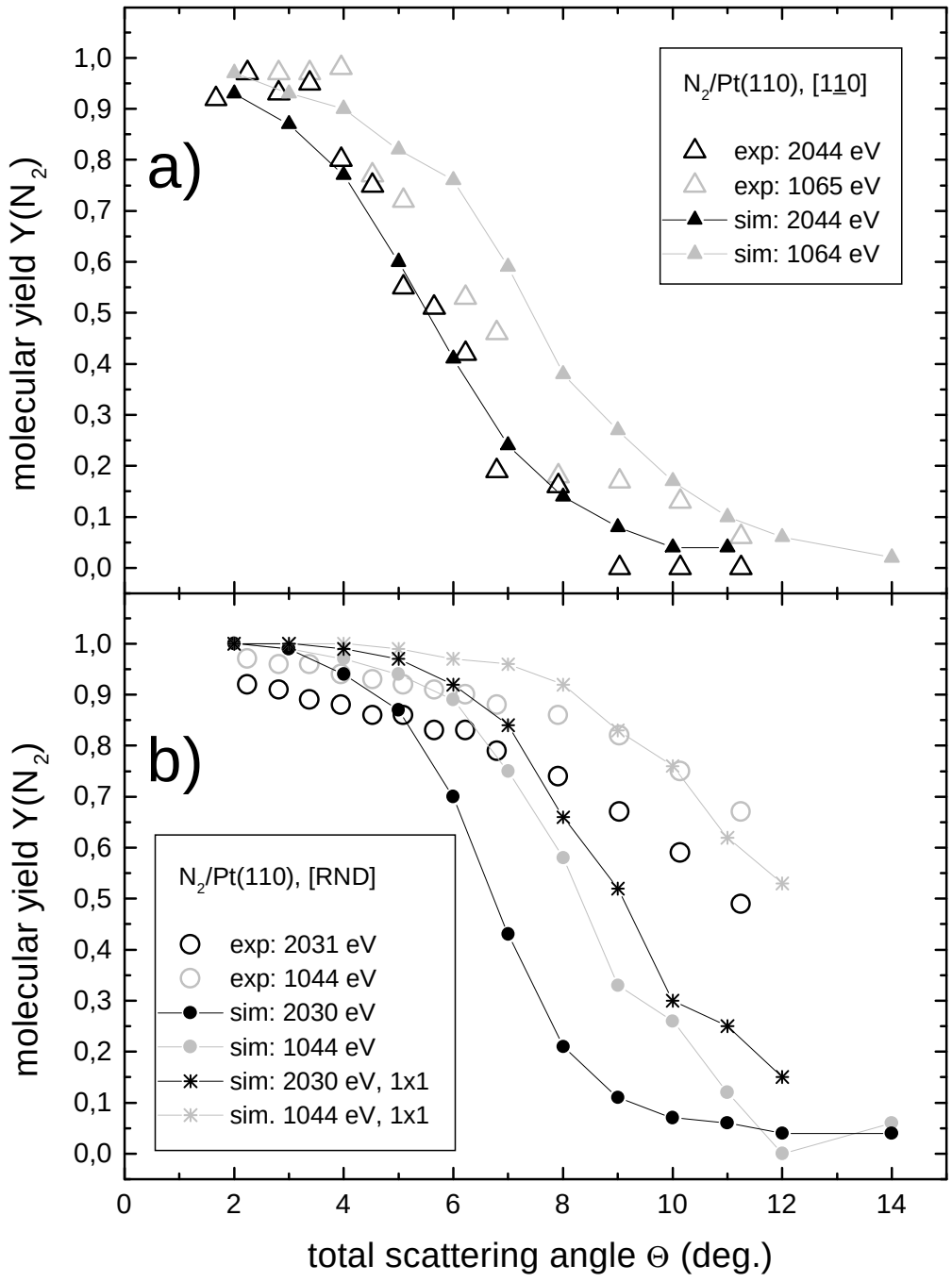

Figure 4.16: Molecular survival for N_2 scattered off Pt(110)(1×2) versus total scattering angle. The open symbols show the experimental results from Fig. 3.5 which are approximated by simulations, plotted as full symbols (connecting lines are drawn just to guide the eye). For $[1\bar{1}0]$-incidence (a), the agreement is good. In case of scattering along a high-indexed direction (b), the simulational results fit better when assuming a 'fictitious' 1×1-surface geometry in the calculations (∗-symbols).

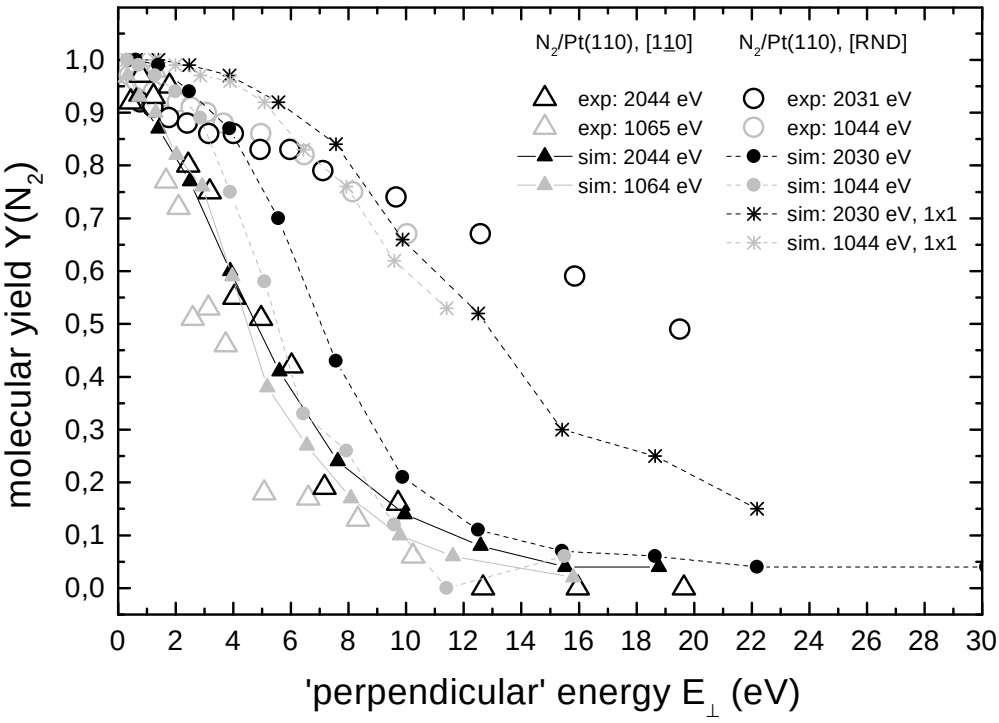

Figure 4.17: The data from Figs. 4.16a and b plotted as a function of the energy which is associated with the perpendicular component of the primary velocity of the molecules. The points fall onto a common curve for the random- and the $[1\bar{1}0]$-direction, respectively.

Plotting the curves from Fig. 4.16 versus the 'perpendicular component' of the primary energy reveals that all data points nicely merge into one common curve for random- and for $[1\bar{1}0]$-scattering, respectively. This result is shown in Fig. 4.17.

Chapter 5

Discussion

Obvious differences in the dissociation behavior have been found for the scattering of hydrogen and nitrogen, thereby unveiling the action of different dissociation mechanisms.
In case of nitrogen, the molecular dynamics simulation achieves good agreement with the experimental results and thus offers a vast quantity of information on the interaction during the scattering process. For hydrogen, substantial information on the dissociation process is obtained from the energy distribution of the fragments.

5.1 General Aspects

As mentioned in Chapter 1, the dissociation of a scattered molecule can arise from two distinct mechanisms: the elastic interaction between the molecular constituents and the surface atoms on the one hand and electronic processes, i.e., electron transitions into antibonding molecular states on the other hand.

For very low kinetic energies, $E_0 \to 0$, the survival probability for all systems with N_2^+ studied in this work is practically one, whereas for H_2^+, it tends to decrease towards zero (cf. Figs. 3.3, 3.4, and 3.9). Apart from the observation of differently shaped spectra, this is evident for the involvement of two distinct dissociation channels. The nitrogen molecule is well known to interact mainly elastically with the surface, so it will be the first subject for the discussion here.

5.2 N_2^+

At higher energies, the fate of the molecules not only depends on their orientation with respect to the surface normal, but also on the azimuthal orientation of the surface with respect to the beam. This azimuthal effect shows up in all measurements where the primary energy or the scattering angle is varied: The dissociation is more efficient when scattering along lower indexed directions.

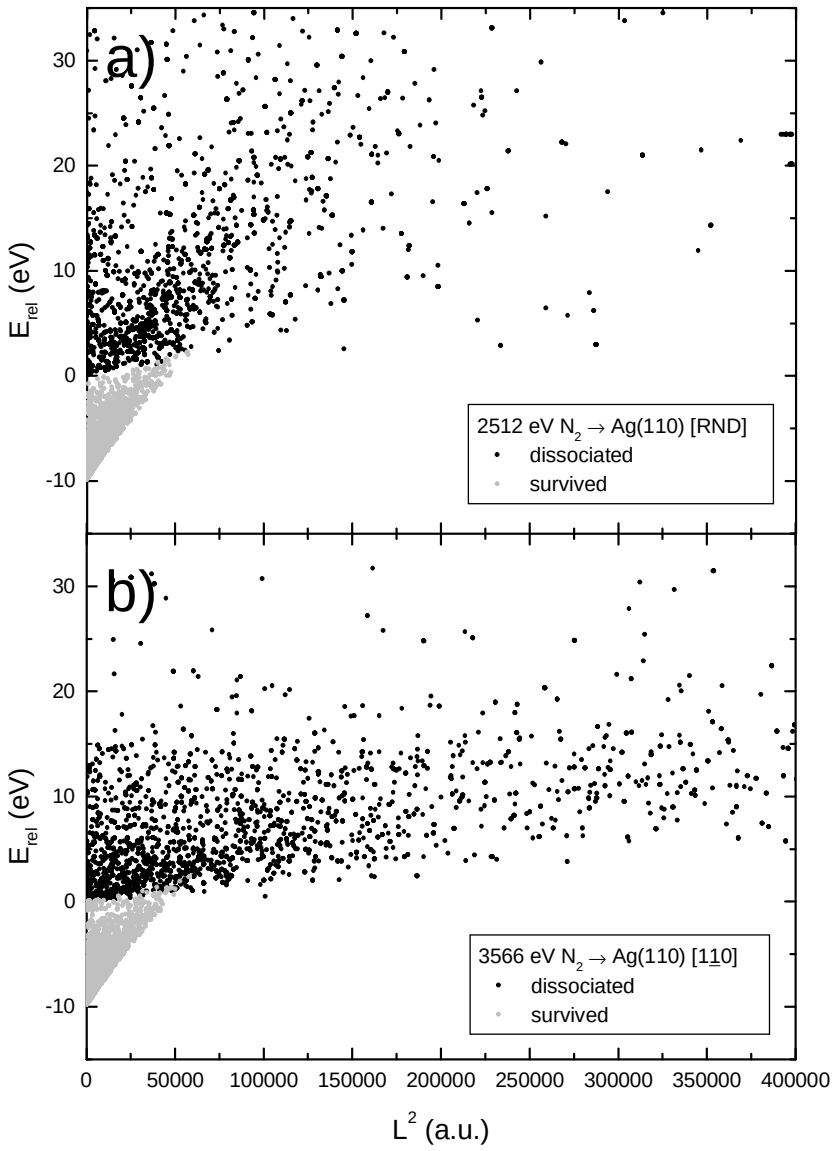

Figure 5.1: Phase space spanned by the squared angular momentum L^2 and the C.O.M. energy E_{rel} of N_2 scattered from Ag(110) along a high-indexed (a) and the $[1\bar{1}0]$-direction (b), obtained by simulation.

In this context, the following picture is proposed by Vicanek and Schlathölter *et al.* [70]: When traversing along high-indexed directions across the target surface, the molecules experience a rather flat potential surface since the corrugation experienced by the projectile averages out (unless it is as strongly corrugated as the Pt(110)(1×2) surface, which will be discussed in particular in the next section). As a consequence, the molecules follow relatively short and uniform trajectories. Negligible rotational excitation occurs during the interaction; the most important elastical process is the vibrational excitation.

For an impact along a low-index direction, however, the trajectories are longer and a deeper penetration between the first layer atoms occurs. The molecular constituents scatter rather independently from the walls of the surface semichannels, their trajectories consist of multiple collisions which usually lead to higher rotational excitation of the molecule compared to the high-index incidence.
Fig. 5.1 compares the phase spaces of squared angular momentum and relative energy in the C.O.M. system of the molecule for the two azimuthal orientations. Both quantities, obtained by simulation of the scattering process, are conserved during the dissociation. Each dot represents an event of dissociation (black) or survival (gray). The essential information however is contained in the density of events: compared to the high-indexed case, the mean density of occurrences of dissociation for $[1\bar{1}0]$-incidence is shifted towards higher angular momenta, i.e., for a given relative energy, the importance of rotational excitation is higher.

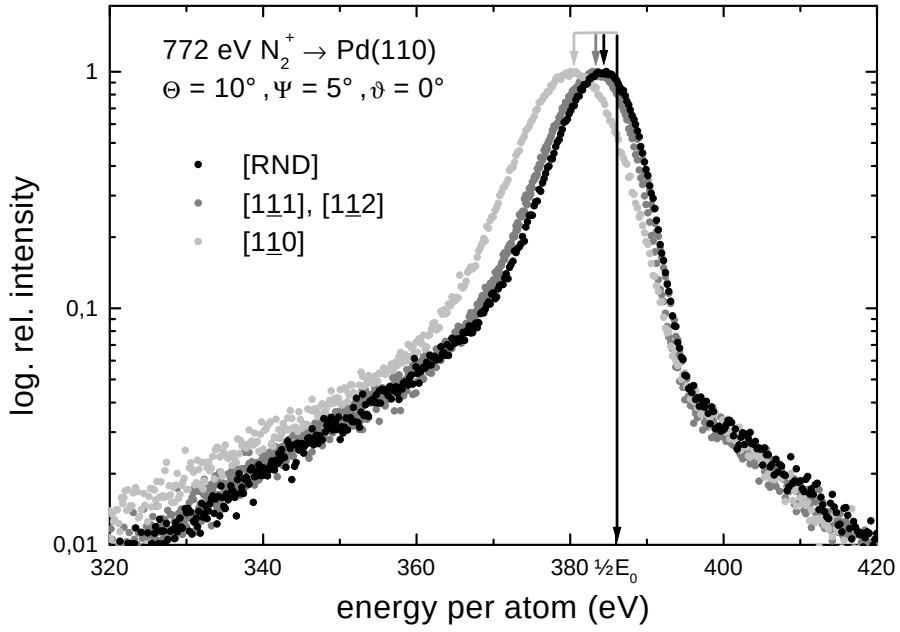

Figure 5.2: Energy spectra of 772 eV N_2^+ scattered from Pd(110) under variation of the azimuthal angle of incidence φ.

The consequence of the trajectory selection is directly visible in the energy spectra. For this purpose, in Fig. 5.2 three spectra obtained from scattering N_2^+ off Pd(110) along different azimuthal directions are compared. The shift of the spectral distribution with respect to the energetic position of the primary beam (vertical line) is a measure for the mean inelastic energy loss during the scattering and therefore a hint on the mean length and depth of the corresponding trajectories. For the high-indexed 'random' di-

rection, this shift is minimal but increases successively when switching to lower indexed orientations. The relatively high energy loss suffered by the $[1\bar{1}0]$-scattered particles is in accordance with the above mentioned model. A further quantitative analysis of the energy losses observed in the spectra will not be performed in this work.

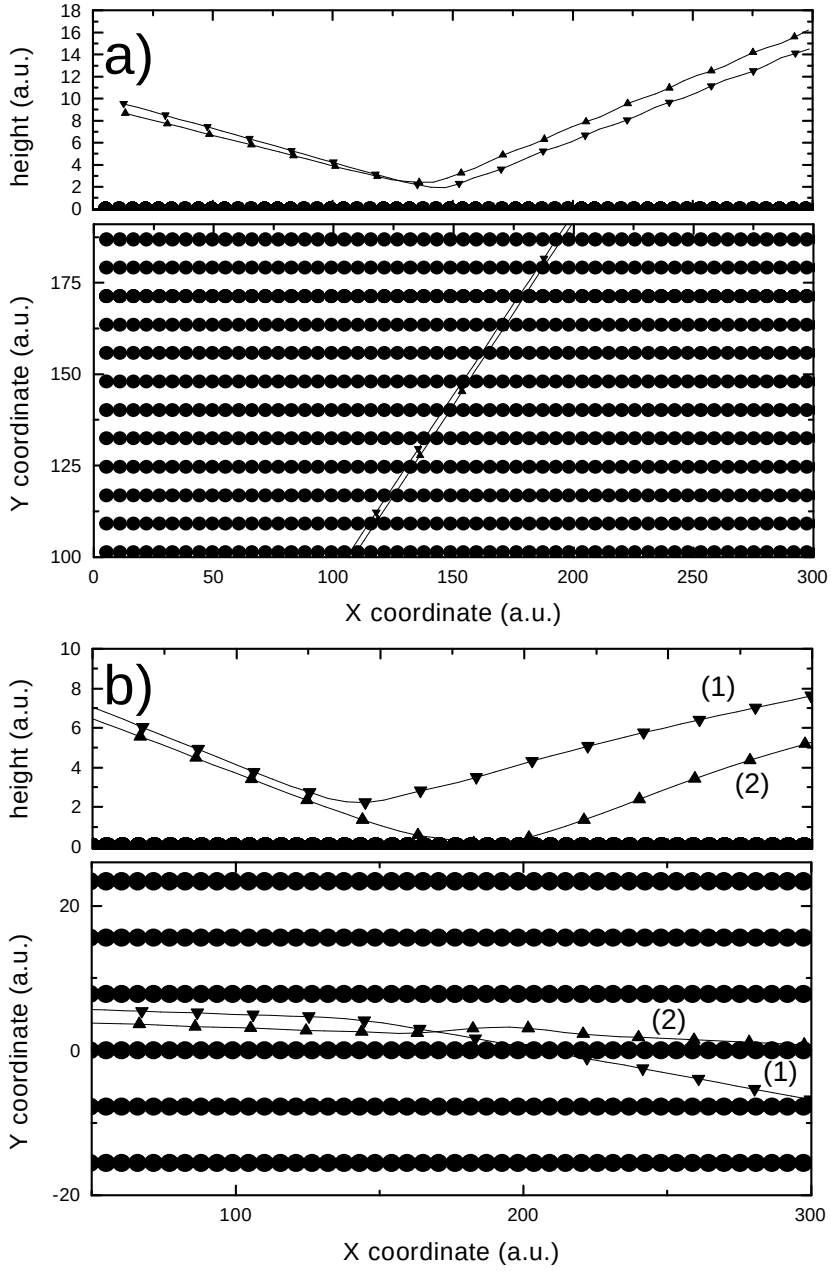

Figure 5.3: Trajectories of N_2 molecules (here 2.5 keV) scattered from Ag(110). The situation for high-indexed ('random') incidence is illustrated in (a), the low-indexed case in (b). Each plot shows a side and a top perspective. Note the different scaling of the axes.

A detailed trajectory analysis comparing high- and low-index scattered N_2 projectiles can also be obtained from ScaDiM. Two representative trajectories of initially bound N atoms for each crystallographic orientation are displayed in Fig. 5.3.
While for high-indexed incidence (Fig. 5.3a) the trajectories show no remarkable differences in their penetration depths and azimuthal dispersion, for the low-index case the scattered particles can be assigned to two classes of trajectories (Fig. 5.3b):

- Particles which impinge on a closely packed top-atom row reach only minimal penetration but scatter with relatively wide azimuthal variation (1). As a result, the interaction time with the surface is very short.
- Constituents which penetrate between the rows and reach respective depths. This channeling also causes significantly longer trajectories. Some of the particles perform 'zig-zag' trajectories due to multiple scattering in the potential wells of the surface semichannels (2).

The purely classical treatment of the molecule-surface interaction is obviously not the whole truth. As a conclusion from the experimental and simulational results on the molecular survival, it is important to consider the effect of screening as well. This effect influences the dissociation considerably by lowering the intramolecular binding energy prior to and during the elastic interaction between the projectiles and the surface.
Subsequent dissociation, activated by mechanical excitation like rotation and vibration, is therefore enhanced. The implementation of the new model in the simulation code – a static z-dependent softening of the intramolecular binding force – is a simple but successful approach to get a qualitative as well as quantitative interpretation of the experimental data in case of the scattering of molecular nitrogen.

5.2.1 The Pt(110) Surface

It has been shown in experiment and simulation that fragmentation is enhanced for scattering along low-index directions, i.e., a clear dependence on the surface structure exists.
In this context, due to its pronounced corrugated structure, the Pt(110)(1×2) surface is a special case. The fragmentation, also for the high-indexed direction, is strikingly high compared to the 1×1-surface of Ag(110) (s. Fig. 3.3). Within the image of mechanically induced dissociation, it is reasonable to suspect the more corrugated missing-row structure to be responsible for these higher dissociation rates. Two observables which may shed some light onto this problem are the distance of the closest approach between projectile constituents and surface atoms as well as the penetration depth of the projectiles [11].

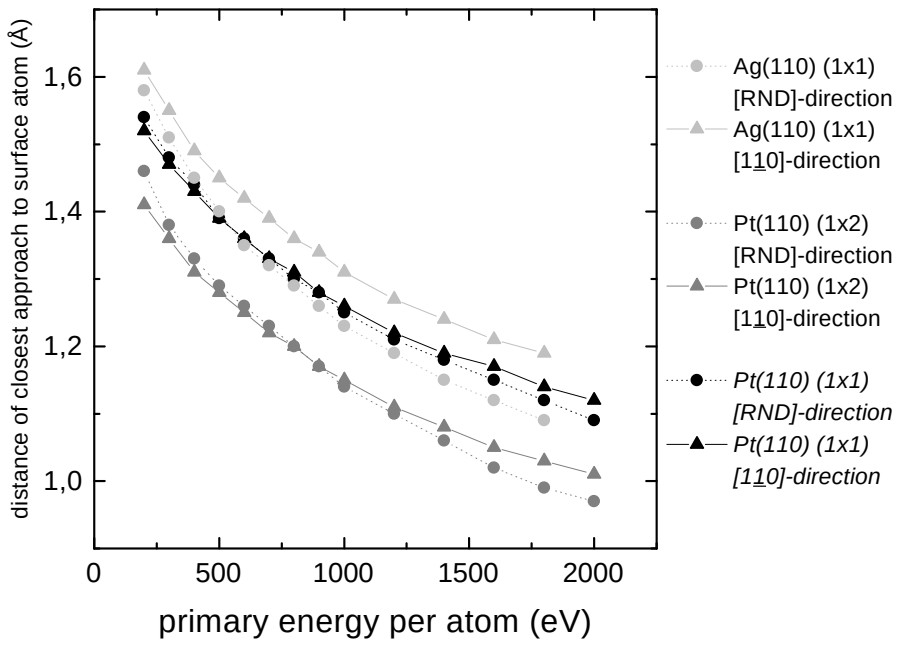

Figure 5.4: Average distances of closest approach between the N_2-molecule constituents and surface atoms of the Ag(110)(1×1), Pt(110)(1×2), and a 'fictitious' Pt(110)(1×1) surface, obtained from simulations.

A closer look into the distances of closest approach as a function of the projectile energy leads to Fig. 5.4. The comparison of the results obtained from the CT calculations is restricted to Ag and Pt, since both, experiment and simulation for the Pd(110) surface, are performed under a different scattering geometry. For the 1×2-reconstructed Pt(110) surface, the impact parameters are generally smaller than those observed for scattering from Ag(110)(1×1) over the whole energy range used in this work, i.e., more violent collisions occur in the former case. This gives rise to a larger transfer of projectile translational energy into internal degrees of freedom. To crosscheck this, Fig. 5.4 also diplays the average distances of closest approach for a fictitious Pt(110)(1×1) surface which is easily modelled in a simulation. These values are now comparable to the Ag case.

In addition, the results for the $[1\bar{1}0]$-direction and the high-indexed direction are almost identical for the Pt(110)(1×2) surface, in contrast to the unreconstructed case of the Ag surface, where the same behavior as in Ref. [11] is found: the mean distance of the closest approach is larger for scattering along a low-indexed direction compared to the high-indexed case. This indicates, that on the Pt surface the fragmentation is not only more efficient but also based on a different mechanism as for the Ag(110)(1×1) surface.

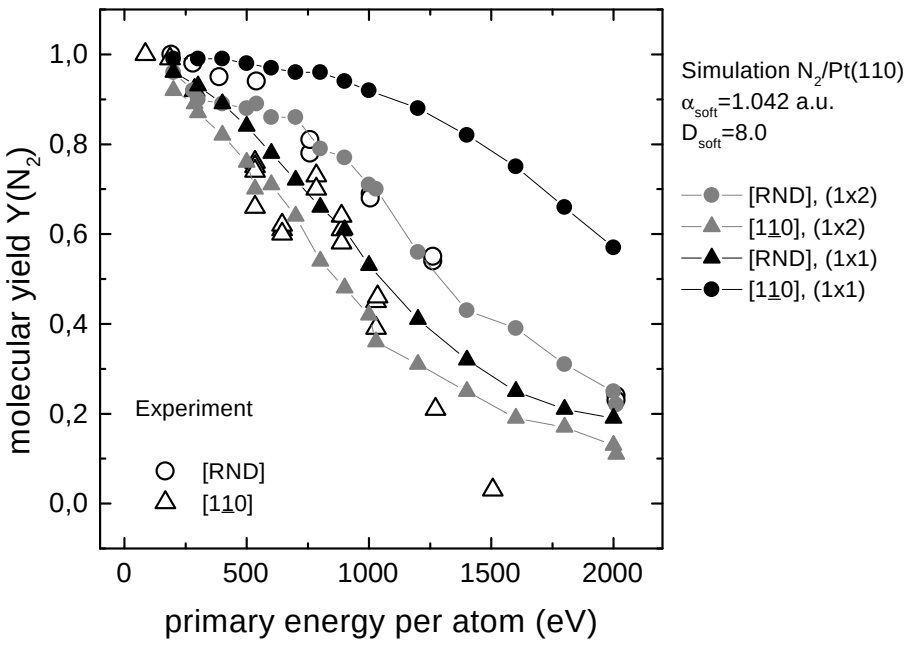

Figure 5.5: Molecular yields from scattering N_2 off Pt(110). The simulations are performed using the 'fictitious' Pt(110)(1×1) surface (black symbols) and compared to the real 1×2-structure (gray symbols). The softening parameters are those from Fig. 4.15a.

Figure 5.5 shows the impact of the surface reconstruction on the molecular survival probability of N_2 scattered from Pt(110). Simply switching from 1×2 to 1×1 – while preserving all other interaction potentials including the softening parameters – increases the molecular survival probabilities remarkably, especially for incidence along the high-indexed direction.

Only for scattering along the $[1\bar{1}0]$-direction off Pt(110)(1×2), negative average distances of closest approach between the molecule and the surface occur in the high energy range (s. Fig. 5.6), which means penetration below the plane of the top layer atoms. In general, a closer approach towards the more 'rugged' 1×2-reconstructed surface is achieved than for the unreconstructed 1×1-faces for both, high- and low-index incidence.
Consequently, the effective $D_{\text{soft}} = 8.0$, which has been determined for the Pt(110)(1×2) surface, is too strong for the 1×1-structure. This explains the fact that the computed dissociation on Pt(110)(1×1) still remains stronger than for Ag(110). The true effective value for Pt(110)(1×1) can be expected to be smaller. Obviously, no experimental data are available for this fictitious geometry.

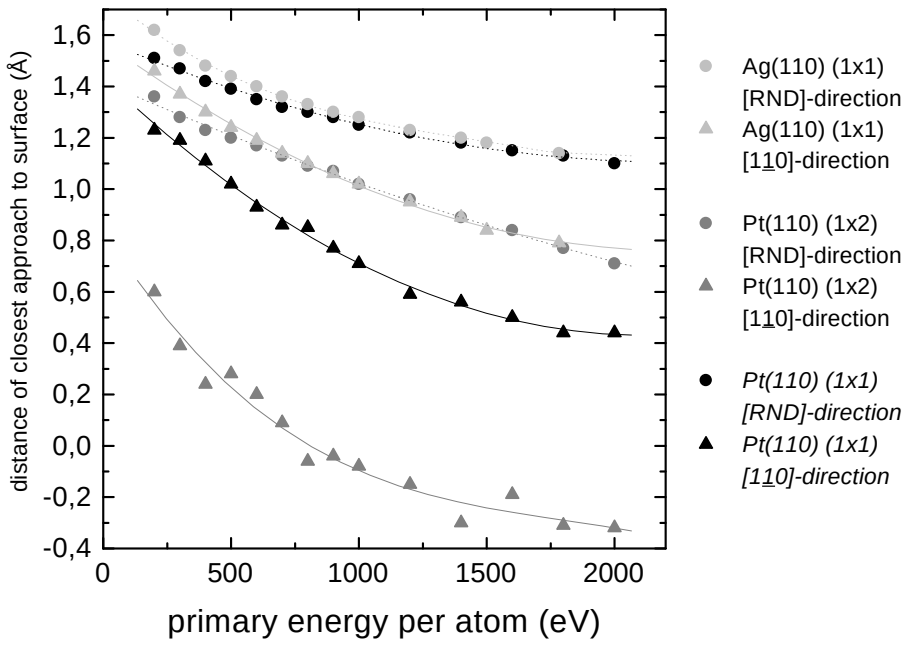

Figure 5.6: Average distances of closest approach between the N_2-molecule and the Ag(110)(1×1), Pt(110)(1×2), and the 'fictitious' Pt(110)(1×1) surface, obtained from the simulations.

To conclude, both features, the more violent nature of the collisions due to the more corrugated 1×2-reconstruction and the higher effective softening due to the deeper penetration of the molecules into the surface are the cause for the enhanced fragmentation in the case of scattering from the Pt(110) surface. This is well reproduced in the simulations.

The results of the energy-dependent molecular yields plotted in Fig. 4.15 show a mismatch between the experimental and calculated values for the $[1\bar{1}0]$-scattering at energies exceeding 1 keV per atom. This might arise from the inaccuracy of the softening model due to the underlying neglect of the lateral surface structure when assuming a simple z-dependence of the molecular bond strength (cf. Sec. 4.6). In particular for the strong corrugation of the 1×2-structure, the impact of this simplification can be expected to become important.

Still unexplained remains the difference in the simulations for the angular resolved study of N_2 scattered from Pt(110) in high-indexed directions (poor agreement) and for the $[1\bar{1}0]$-direction (good agreement), respectively (s. Fig. 4.16).

5.2.2 Further Consequences of the Screening

According to Eq. 3.1, the kinetic energy of the dissociated particles in the laboratory system not only depends on E_0, but also on the actually released energy in the C.O.M. system at the time of the molecular decay as well as on the orientation of the molecule. As a consequence, the distribution of the fragments has a width of several hundred eV in the energy spectra and can thus easily be identified.

Fig. 5.7 compares the measured spectrum of 2512 eV N_2 scattered off Ag(110) in random direction (same spectrum as in Fig. 3.2a) with simulated data. Only one obvious difference is apparent: The EMG function (s. Sec. 3.1) provides the best fit for the experimental spectrum, whereas the simulated distributions merely follow an unshifted (with respect to the energetic position of the primary beam) Gaussian shape. This is not surprising, since in these calculations, the inelastic energy losses and straggling effects, which are known to cause the observed energy shift and the asymmetry in the measured spectra, are omitted.
The simulated spectra are largely symmetric. In order to demonstrate the agreement, the separated atomic distribution is extracted from the plot in Fig. 5.7b and compared to its own Gaussian fit in Figs. 5.7c and d (logarithmic and linear scale), respectively.

An additional peak in the 'hat' of the spectra occurs for molecular scattering under channeling conditions, unless the primary energy is too low. At least two EMG functions are superimposed here, so the complete spectrum consists of three peaks (s. Fig. 3.2b or Fig. 5.8a).
The same 'anomaly' has already been observed in an earlier investigation of the system H_2/Pd(110) at energies around 2 keV [115].

The first intuitive attempt to attribute this additional narrow peak to molecules resulted in inconsistent survival yields. A closer examination of the simulational results (Figs. 5.8b-d), however, reveals the problem:
Not the fraction of the molecules but of the fragments gives rise to the second narrow peak in Fig. 5.8a. The total atomic distribution separated in Fig. 5.8b, which is further analyzed in Figs. 5.8c and d, consists of two superimposed peaks. The broad one is the 'normal' one in analogy to the high-indexed case; the narrow peak is a special feature of the low-index scattering, contributing the characteristic 'hump' to the 'hat' in the total spectrum.

Here, the geometry of the surface allows a deeper penetration of the N_2 molecules into the semichannels down to the second layer. Stronger screening in these deeper regions is expected, resulting in an extreme weakening of the intramolecular binding forces. Consequently, dissociation with nearly zero kinetic energy release according to Eq. 3.1 takes place. The energetic distribution of these 'softly dissociated' fragments forms the narrow peak as observed experimentally.

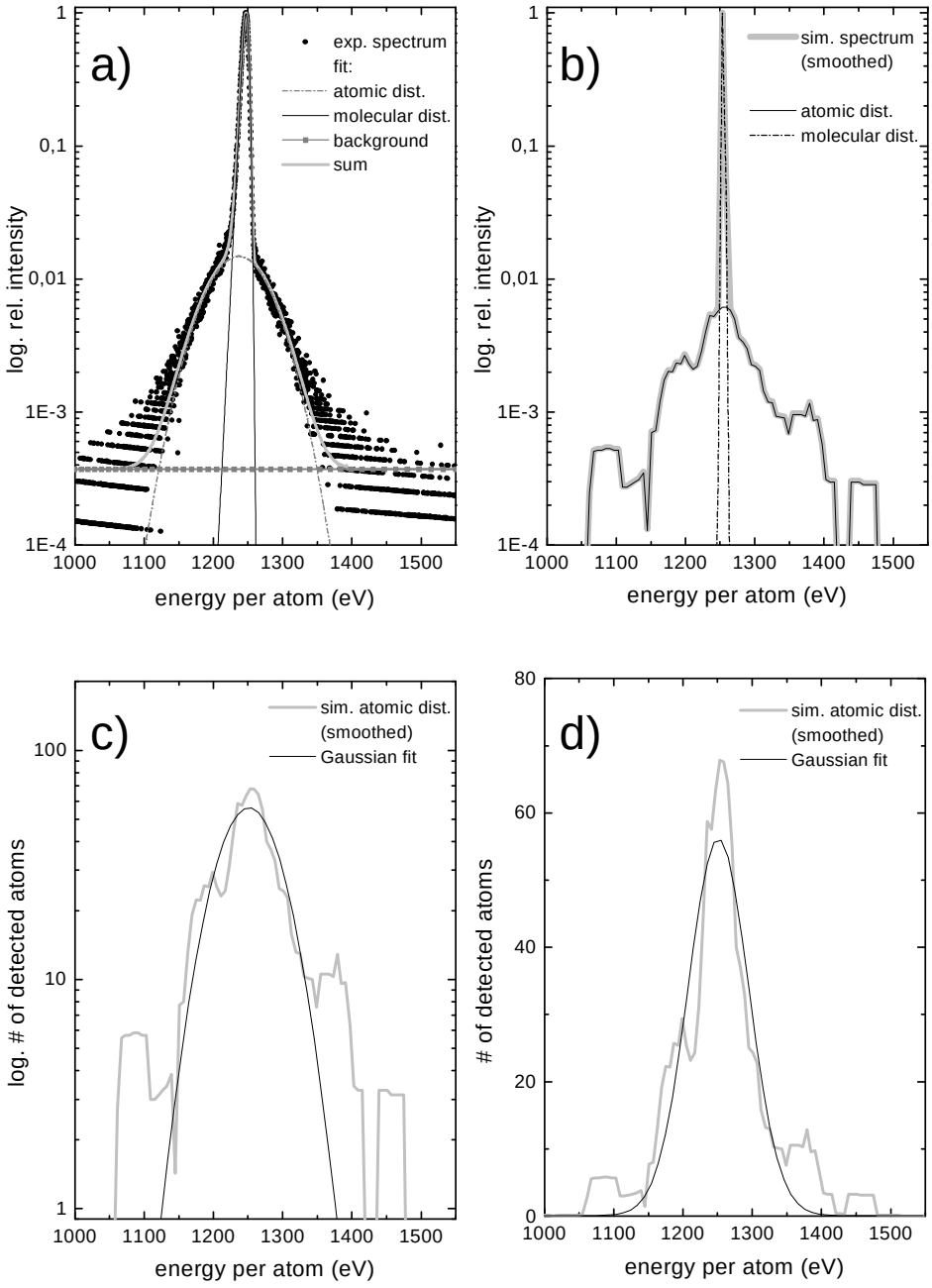

Figure 5.7: Experimental (a) and simulated (b) energy spectrum of 2512 eV N_2 scattered off Ag(110) under high-index grazing incidence. The separation of the experimental spectrum is described in Section 3.1. The simulated spectrum is separated by the software. The molecular and atomic distributions follow a Gaussian shape (see text), as demonstrated for the latter in logarithmic (c) and linear scale (d).

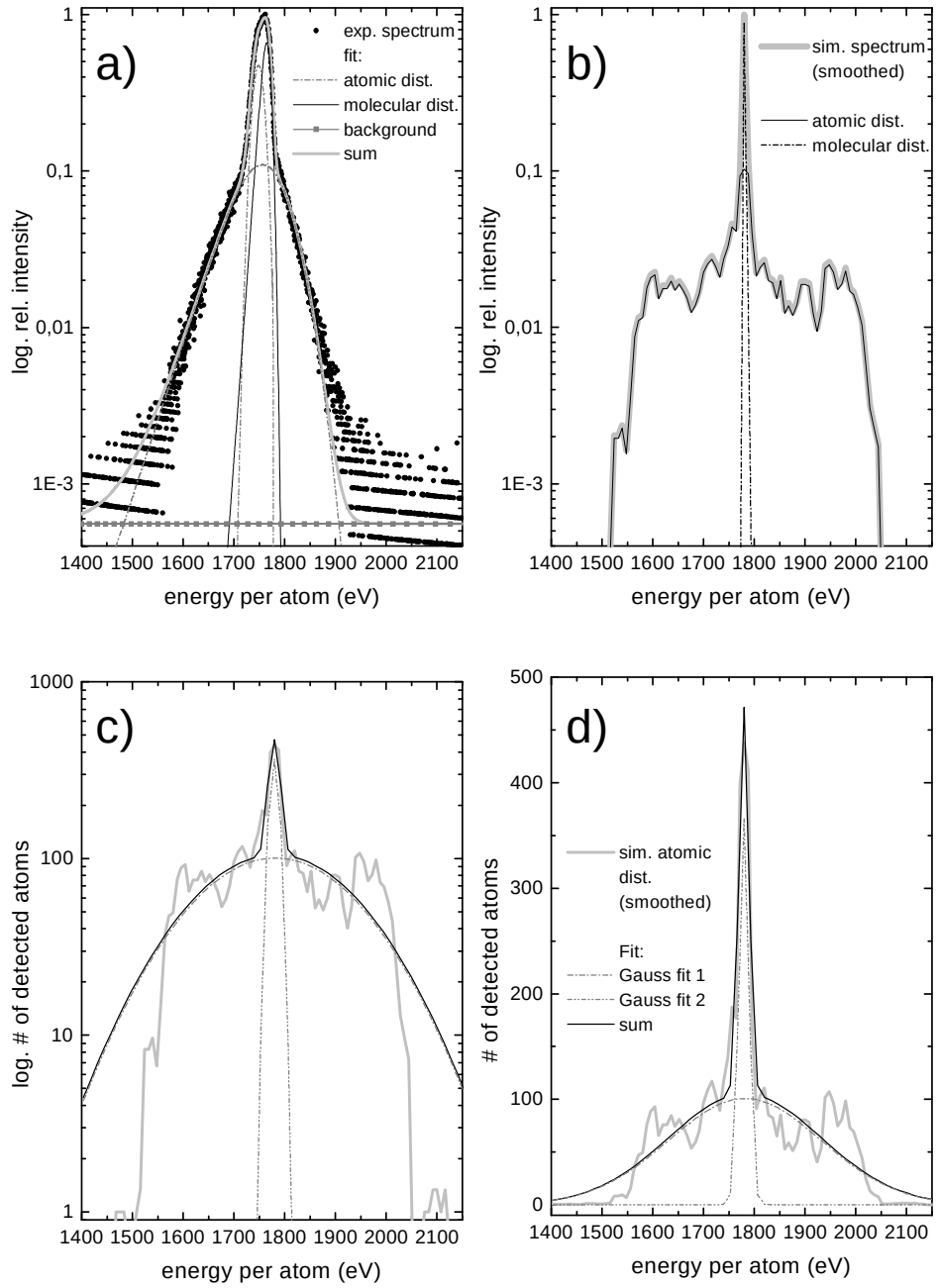

Figure 5.8: Experimental (a) and simulated (b) energy spectrum of 3566 eV N_2 scattered off Ag(110) under low-index grazing incidence. The experimental spectrum (same plot as in Fig. 3.2b) shows three components: one molecular and two atomic distributions. This feature is also reflected by the simulation: the atomic distribution consists of a 'normal' broad peak and a surprisingly narrow one (c and d). The latter is mainly formed by molecules which dissociate deep inside the channels under strong influence of the softening.

Compared to the molecular one, this peak is slightly shifted towards lower energies (cf. Fig. 5.8a), since the surviving molecules do not experience such long and deep trajectories and hence lose less energy. This shift however is not reproduced by the simulations because inelastic losses are not taken into account in the underlying model.

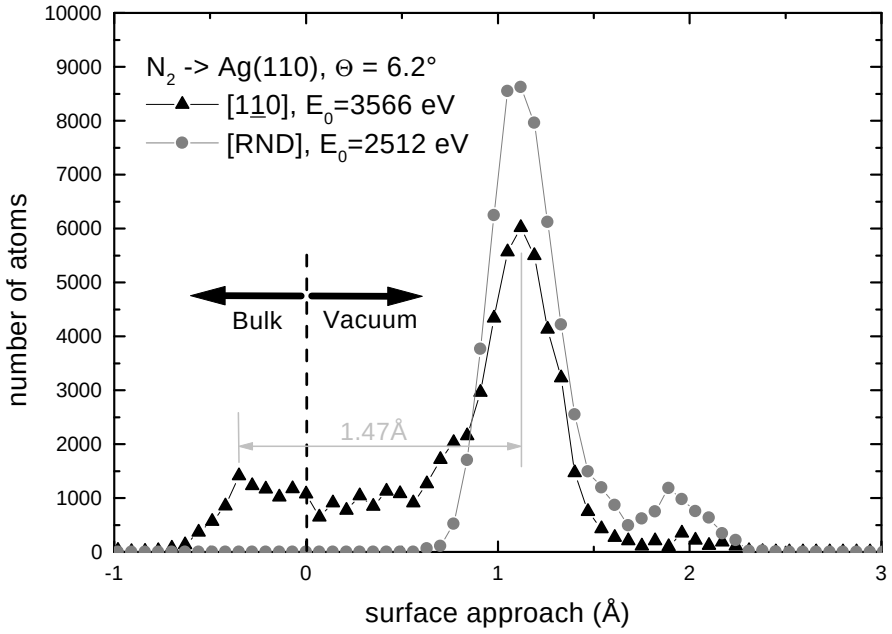

Figure 5.9: Distance of the closest (minimum) surface approach with respect to the top atom layer of nitrogen projectiles scattered off Ag(110) (for the spectra from Figs. 5.7 and 5.8). All N atoms are evaluated, either dissociated or bound in a molecule. No penetration below the first layer is observed for the high-indexed incidence, whereas for low-indexed scattering, a considerable fraction reaches the second atom layer which is displaced Δz=1.47 Å below the top layer in the simulations (unrelaxed case).

Figure 5.9 shows quantitatively the difference in the surface penetration depths for high- and low-index scattering of N_2 from Ag(110)(1×1), as obtained from the calculations that led to Figs. 5.7 and 5.8, respectively. It is clearly visible that in case of $[1\bar{1}0]$-incidence, a considerable part of atoms is reflected from a depth of up to exactly one interlayer-distance deeper. These particles arise from channeling trajectories of type (2) in Fig. 5.3b.

It is now a straightforward and interesting approach to take a closer look on the statistical distribution of the relative energies of the dissociation products in the two cases of azimuthal orientation. Coming back to Fig. 5.1, i.e., the phase space which is spanned by the squared angular momentum and the relative energy in the C.O.M. system, a

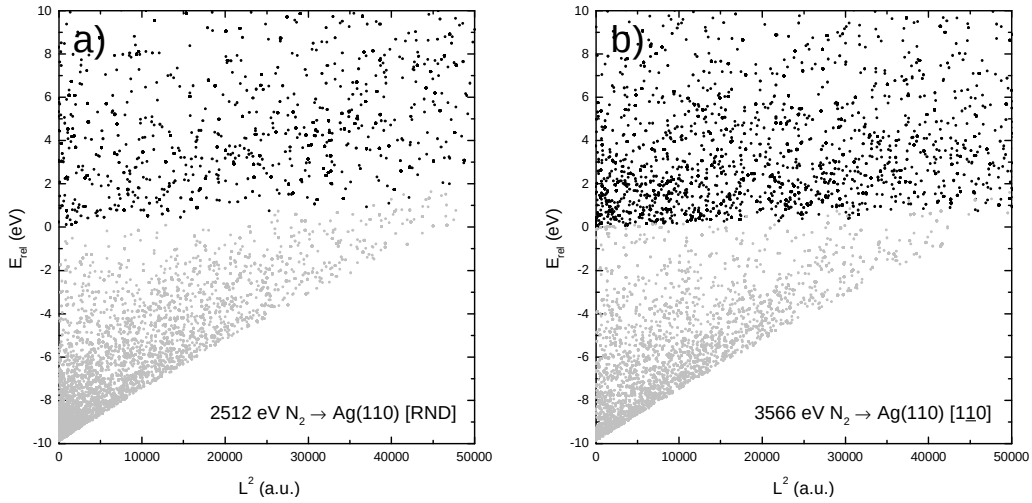

Figure 5.10: Density of events in the phase space spanned by L^2 and E_{rel}. This representation shows an enlargement of the region around $E_{\mathrm{rel}} = 0$ in Fig. 5.1. The azimuthal orientation of the target is a) high-indexed and b) low-indexed with respect to the incident beam. Molecules which survive the scattering occupy the area formed by the gray dots (note, that only 50% are plotted) and the cracked ones are represented by black dots.

zoom into the region around $E_{\mathrm{rel}} = 0$ is shown in Fig. 5.10.
The two plots show clearly how different the interaction in the two azimuthal directions is. While for scattering along the high-indexed direction (Fig. 5.10a) the region around $E_{\mathrm{rel}} = 0$ is sparsely occupied, there is obviously a high concentration of dissociative events at low relative kinetic energies for incidence along $[1\bar{1}0]$ (Fig. 5.10b). This confirms the finding of the 'soft dissociation' which occurs under channeling conditions, where a part of the molecules is subject to a strong screening by free metal electrons in between the semichannels and thus can dissolve with extraordinarily low relative kinetic energies.

From the experiments reported at the end of Section 3.2, one can conclude that not only the energetic, but also the azimuthal distribution of those atoms in the exit trajectory which form the sharp peak is limited. The 'channel peak' only appears in the central spot region of the specularly reflected beam. It disappears at other azimuthal detector positions and the remaining slim distribution is due to surviving molecules only. Again, these experimental findings are examined with the help of simulations:
Fig. 5.11 demonstrates the two cases of different azimuthal TOF-detector positions (0° and 3.3° with respect to the direction of the specularly reflected beam) referring to Figs. 3.6b and c. The principal characteristics of the experimental results are reproduced: The sharp energetic peak of the 'softly dissociated' atoms only appears in the specular geometry (Fig. 5.11a). The remaining 'hat' in the spectrum obtained for the off-centered detector position at $\vartheta = 3.3°$ merely consists of surviving molecules.

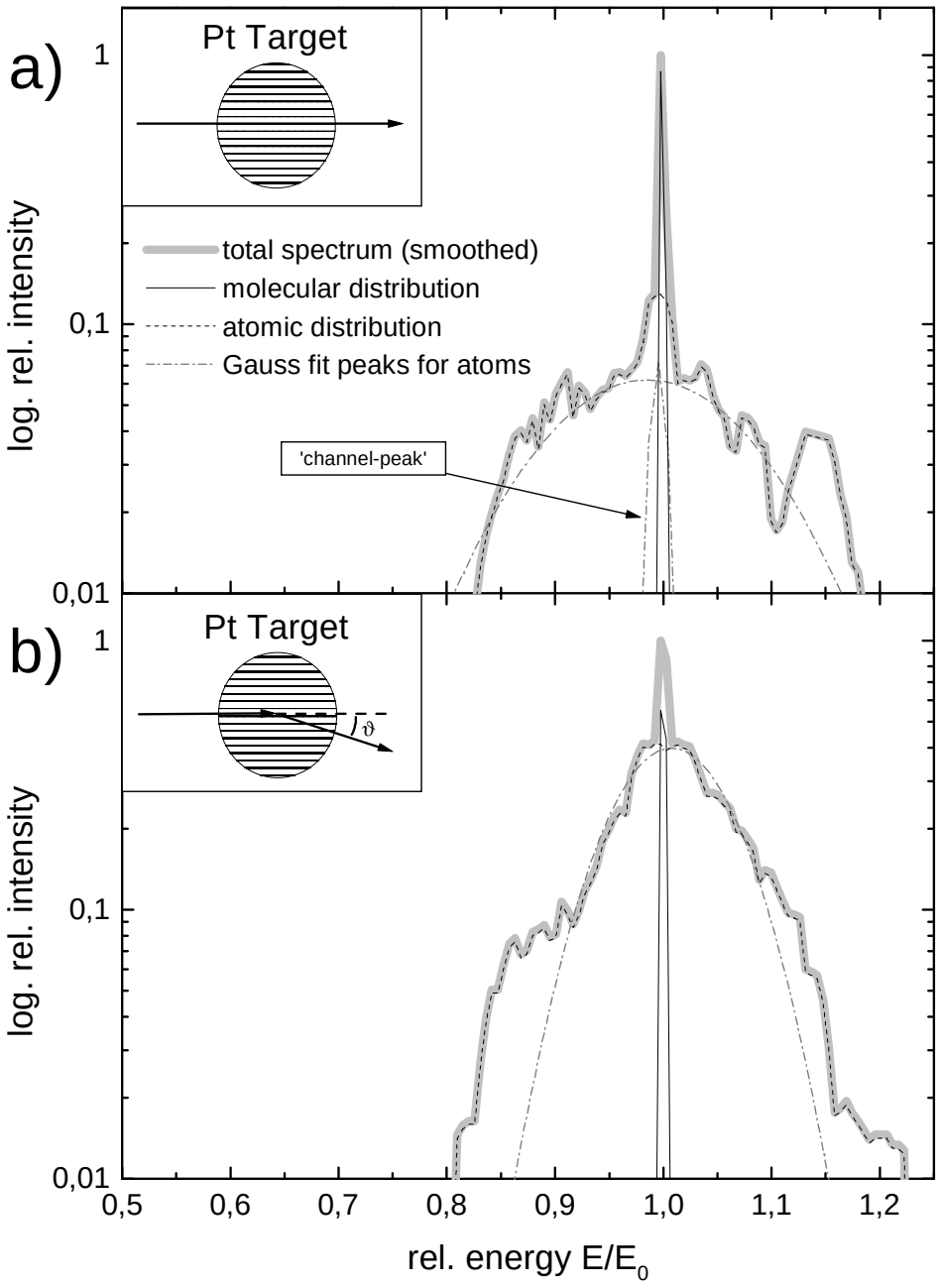

Figure 5.11: Simulated energy spectra of 2050 eV N_2 scattered off the 1×2-reconstructed Pt(110) under low-index incidence along the $[1\bar{1}0]$ semichannels ($\varphi = 0°$), calculated for two different azimuthal detector positions ϑ. The underlying geometries are indicated in the insets. Analysis of both spectra shows qualitative agreement with the experiment (cf. Fig 3.6): In the center spot $\vartheta = 0°$ (a), the fraction of softly dissociated and channeled atoms gives rise to an additional narrow peak which vanishes in the off-centered position $\vartheta = 3.3°$ (b).

5.3 H_2^+

Unlike the case of N_2^+, charge transfer processes play an important role for the dissociative scattering of H_2^+. Therefore, the simulations presented in Chapter 4 cannot be applied to this system, since electron transition processes are not yet implemented in the current version of ScaDiM.
In the majority of investigations of this system [16, 17, 41, 116, 117] it is concluded that the main mechanism leading to dissociation of H_2^+ molecules is resonant electron capture from the metal conduction band into an antibonding state of the molecule. This process is called dissociative neutralization (cf. Sec. 1.1.2).

The molecular survival rates obtained for metal surfaces in this work (Fig. 3.9) show a remarkably small fraction of molecules surviving the scattering process. In particular, the molecular yield reaches maximal values of up to 35% only for the Ag(110) surface under high-indexed incidence. For the other configurations, the yield does not exceed 10%.
An interesting feature is the fact that in the low energy region, the molecular yield tends to initially increase with the kinetic energy. This is further evidence for the fact that the inelastic interactions are dominant in the dissociation process at these energies. Furthermore, comparison to scattering from insulator surfaces (Fig. 3.10) confirms the

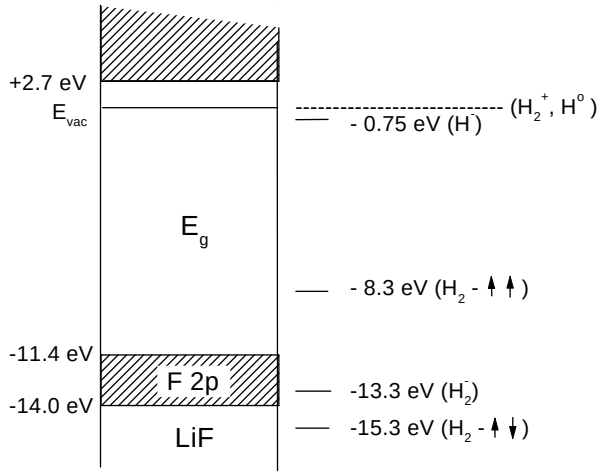

Figure 5.12: Energy level diagram of LiF and the important energy levels of H_2 and H. (Note that due to the antibonding nature of the $H_2^*(b^3\Sigma_u^+)$ state, the value of -8.3 eV is only valid for Franck-Condon transitions from the H_2^+ ground state.) From: [95].

theory of the dissociative resonant neutralization into the $H_2^*(b^3\Sigma_u^+)$ state at metal surfaces. The electron capture into the antibonding triplet state is very unlikely for a wide band-gap insulator such as LiF [95]. Fig. 5.12 illustrates a schematic energy level diagram of LiF and the hydrogen system. Since the $H_2(X^1\Sigma_g^+)$ ground state is shifted up by the image potential (cf. Sec. 1.1.2), it happens to be in perfect resonance with

the F 2p valence band of LiF. In contrast, there are neither electrons in resonance with the $b^3\Sigma_u^+$ state nor any Auger type processes possible. Thus, the purely electronic dissociation channel is in this case switched off, explaining the high molecular survival fraction at low energies in Fig. 3.10. Its decrease with higher energies can be ascribed to the mechanical interaction with surface atoms like in the above studied case of nitrogen on metal surfaces.

Regarding metals, the initially increasing molecular yields and the maximum at medium energies as experimentally observed in Fig. 3.9 still require further discussion. A model based on resonant neutralization into the $H_2^*(b^3\Sigma_u^+)$ state and subsequent (partial) Auger de-excitation via negative ion resonance as reported in Sec. 1.1.2 offers a possible explanation of this observed behavior:

The transition rates for both, the resonant and the Auger capture process strongly depend on the molecule-surface distance. Since the resonant neutralization into the dissociative b state is very efficient – compared to the Auger neutralization – it can be assumed that most molecular ions are transformed into the corresponding excited state already during the initial part of the scattering trajectory, i.e., before the alternative non-resonant process becomes efficient [42]. In particular, the contribution of mechanical molecule-surface interaction and the effect of the (dynamic) screening are still low at this comparably high distance from the surface. From that moment on, the neutralized H_2^* dissociates along the potential curve of the $b^3\Sigma_u^+$ state (cf. Fig. 1.5), i.e., it stretches due to the repulsive nature of the state. While this excited molecule continues approaching the surface, the Auger process described by Eq. 1.7, which is necessary to de-excite the dissociating molecule, becomes more efficient. The motion associated with the stretching is rather fast, pushing towards the limit beyond which dissociation happens for certain. If the Auger de-excitation stops this process within the critical time, the molecule can survive after being transformed into the $X^1\Sigma_g^+$ ground state.

If a molecular ion once is neutralized into the repulsive b state, the probability that it de-excites before the dissociation is inevitable increases with v_{proj} and therefore with E_0. Growing survival rates as found in the low energy region in Fig. 3.9 could be explained by this fact.
On the other side, with increasing energy, the impact of the elastic processes grows and contributes to the fragmentation, as well as the increasing screening due to the closer surface approach of the projectile trajectories. Depending on the given structural and geometrical properties of the surface, the molecular yield is thus efficiently reduced in the high energy region. The strong differences between the curves for the two metals can be ascribed to structural effects, i.e., dissociation for scattering off Pt(110) along high-indexed directions is generally enhanced due to the rugged corrugation of the missing-row structure.

The composition of the complete H_2^+ TOF-spectra is, due to the additional contribution of the electronically induced dissociation process, too complicated for a simulational analysis as done for the scattering of N_2^+. However, essential information on dissociation mechanisms is contained in the high energy part of the distributions of the scattered molecular fragments.
The spectra of atoms scattered from a solid surface under molecular ion bombardment are broadened in comparison to those under atomic ion bombardment and have extended high energy parts reaching into the region $E > E_0$ (cf. Sec. 3.1). The high energy tails result from either the re-distribution of the energy of the fragments colliding with each other after dissociation or from the internal energy ε acquired by the atoms in the dissociation process (cf. Fig. 1.5). The former possibility is considered in Refs. [118, 119], where it has been shown that this channel is effective for heavy particles and large glancing angles. Therefore, for grazing scattering, the high energy tails are characterized by the released kinetic energy ε, which depends on the electron structure of the molecule as well as on its excitation at the moment of decay.

Generally, the spectrum of released relative energies ε can be described by a corresponding distribution function $f(\varepsilon)$. The determination of the form of this function, which is closely connected with the dissociation mechanism, is important for the latter to be identified. The best part of the energy spectra to use for deconvoluting $f(\varepsilon)$ is the high energy tail, since the low energy one is more blurred by inelastic losses and energy loss straggling.
In order to solve the problem, one needs to calculate the energy distributions dN/dE of H atoms scattered off a solid surface under bombardment with molecular ions H_2^+.

Let a H_2^+ molecule with the energy E_0 dissociate as a result of any process at a time t along the scattering trajectory. After that, each of the atomic fragments has an energy E_{lab} according to Eq. 3.1 in the laboratory system. In general, E_{lab} is subject to:

- elastic and inelastic energy losses by the molecule before its decay on which both, E_i and in principal ε depend;
- the form of the distribution function $f(\varepsilon)$ unambiguously connected with the dissociation mechanism;
- the molecule axis orientation with respect to the direction of its center-of-mass movement.

Further, for the final calculation of dN/dE, one needs both to average the distribution dN/dE_{lab} over the time t, taking into account the dissociation probability for a given mechanism, and to consider elastic and inelastic energy losses by the atoms after dissociation.

Such a task can be solved via molecular dynamics simulations of the scattering trajectories, as e.g. done in Chapter 4, but further considering the probabilities of the different decay processes and the stopping powers for both H_2^+ and H. However, aiming at the calculation of the high energy parts of the energy spectra for $E/E_0 > 1$, i.e., for the energy region inaccessible to atomic scattering, such complex tasks can be essentially simplified, as described in the following.

The experimental data obtained for H_2^+ in this work as well as published in [17, 116, 117] and theoretical studies [36, 41, 117] all indicate a dominating role of the dissociative neutralization process for the energies and angles under study. All these investigations further allow the conclusion that the rate of the dissociative neutralization is high (cf. also Sec. 1.1.2), which means that the fragmentation of the molecules already occurs in the initial part of the scattering trajectory, including only a few collisions with surface atoms [14].

In terms of that mechanism, the kinetic energy ε released in the dissociation process is determined by the internuclear distance R at the moment of the electron transition occuring at a fixed nuclei position, the function $f(\varepsilon)$ reading:

$$f(\varepsilon) = \left.\frac{dN}{dR}\right|_{R=R(\varepsilon)} \frac{dR(\varepsilon)}{d\varepsilon} \quad , \tag{5.1}$$

where $R(\varepsilon)$ describes the form of the repulsive potential curve which for the $b^3\Sigma_g^+$ state of H_2 is well approximated by an exponential function

$$U(R) = Ae^{-\alpha R} \quad . \tag{5.2}$$

dN/dR is calculated within the harmonic oscillator approximation. Aside from a constant factor, the function $f(\varepsilon)$ reads [120]:

$$f(\varepsilon) = \frac{1}{\varepsilon} \exp\left[-\frac{m\omega}{\hbar\alpha^2}\left(\ln\frac{\varepsilon}{A} + R_0\alpha\right)^2 \tanh\left(\frac{\omega\hbar}{2kT_v}\right)\right] \quad , \tag{5.3}$$

where m, ω, R_0, $\hbar$, and k are the atom mass, the vibrational frequency, the equilibrium distance between the molecule's nuclei, and the constants of Planck and Boltzmann, respectively. A and α are the parameters of the potential energy curve, T_v is the vibrational temperature.

Since the high energy tail of a spectrum $E/E_0 > 1$ cannot be formed by molecules and atoms penetrating into the solid where both, inelastic energy losses and energy loss straggling, are relatively high, an effect of straggling on the form of that part of the spectra may be neglected. The inelastic energy losses determined by the dependency

$\Delta E \sim E_0$ (cf. Sec. 1.1.3 and [121, 122, 123]) can be simply considered by the corresponding shift of the spectra.

The above considerations justify the simplification to set $E_i \approx E_0$ in Eq. 3.1. This means, that the molecular constituents from the high energy part of the spectrum lose most of their energy after dissociation, not before. So, the whole prehistory of the molecule, i.e., before its decay, is described with T_v, being the only model parameter.

Therefore, the high energy tails can be estimated by the formula:

$$\frac{dN}{dE} \sim \int\int\int \delta\left[E - E_{lab}(\varepsilon, \psi, \phi)\right] f(\varepsilon) d\Omega \tag{5.4}$$

where $\delta(x)$ is the Dirac delta function. As the electron transition into the antibonding state mainly occurs on the initial part of the trajectory, all molecular axis orientations are supposed to be equally distributed.

Comparison with the Experiment

Equation 5.4 can now be used for the calculation of the high energy tails of the energy distributions under the conditions of the experiment, i.e., for fragmented hydrogen atoms produced by scattering H_2^+ ($E_0 = 300 \ldots 1300$ eV) from the surfaces Ag(110) and Pt(110) at grazing incidence ($\Psi = 3.1°$) [124]. The function $P(E)$ of the detector sensitivity (s. Sec. 2.2.3) is taken into consideration and the integration over the angular variables in Eq. 5.4 is performed within the angle of acceptance of the detector (s. Sec. 2.2).

In Figs. 5.13a-d, the high energy tails of scattered H atoms, calculated taking the inelastic energy losses to be $\Delta E \sim E_0$ (cf. Sec. 1.1.3) for three initial energies of H_2^+ molecules impinging onto the (110)-surfaces of Ag and Pt along the low-indexed $[1\bar{1}0]$ channel- and high-indexed 'random' directions, are shown in comparison with the experiment. The adjustable parameter T_v is chosen to obtain a best fit with the experiment. It is seen that a good agreement between theory and experiment can be achieved by varying the only free parameter. The values of T_v obtained by this fitting procedure have the physical meaning of the vibrational temperature of a molecule at the moment of dissociation.

In the general case, the value of T_v at the moment of dissociation of the molecule depends on many factors. After leaving the ion source, the beam of bombarding molecules has a certain temperature resulting from both, the type of the beam source and the processes of ionization occurring in there [125]. In particular, however, a part of the translational energy of the molecules is transferred into their internal degrees of freedom as a result of multiple collisions of the molecular atoms with solid surface atoms [4].

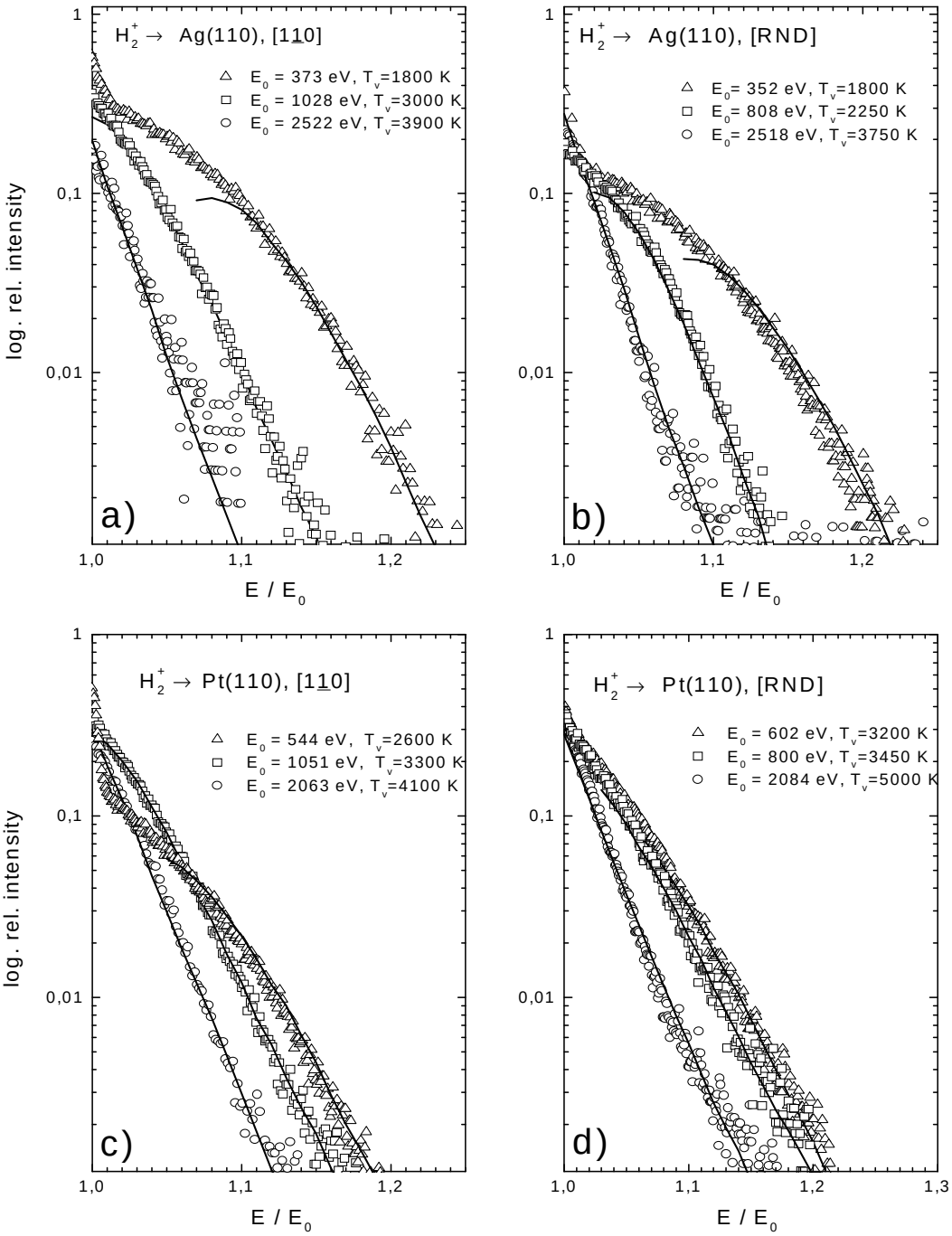

Figure 5.13: The high energy tails ($E > E_0$) of the distributions of dissociated hydrogen atoms obtained from scattering H_2^+ molecules off Ag(110) and Pt(110). Symbols are experimental values (Sec. 3.3), lines are the fitted results from the calculations.

The internal energy that is accumulated that way up to the moment of decay depends on the actual form of the scattering trajectory: E_0, Ψ, the direction of incidence, the atomic structure of the target surface, and the electronic structure of the subsurface region determining the probability of the dissociation, i.e., roughly speaking, on the position of the point of decay on the trajectory.
It is not ruled out however that the vibrational temperature can be changed by electronic processes that are not directly connected with the dissociation, e.g. by the dynamic screening and the appropriate dependence of the equilibrium distance between the nuclei on the electron density near the surface [126].

So it is interesting to analyze the dependence of T_v on such experimental parameters as the initial energy, the type of the target surface and to consider the orientational sensitivity of T_v.
The dependence of T_v on E_0, giving the best fit between the calculated and experimental high energy tails of H atoms scattered from Ag(110) and Pt(110) surfaces under bombardment with H_2^+ along a high-indexed ('random') and the $[1\bar{1}0]$-direction are shown in Figs. 5.14a and b. By comparing these plots, it is obvious that $T_v(\mathrm{Pt}) > T_v(\mathrm{Ag})$ for all values of E_0. This can be explained by the fact that the Pt(110) surface is more corrugated due to the 1×2-missing-row structure, in accordance with the observation of higher fragmentation for scattered nitrogen molecules as found in Chapters 3 and 4.

It is also seen from Fig. 5.14, that the maximal value of T_v reached in the energy range under study is about 5000 K, i.e., the vibrational energy is small (∼10%) with respect to the dissociation energy of the molecule. As a conclusion, the molecule cannot dissociate from vibrational excitation alone at these energies.

Another feature seen from the two plots is that the temperatures for scattering off Pt along the 'random' direction are higher than for the $[1\bar{1}0]$-direction, in contrast to the Ag case. A possible reason is that for high-indexed incidence, the molecule moving along its trajectory experiences a more corrugated surface than for the low-indexed direction, where it is subject to mainly rotational excitation. The difference in the temperatures is not so substantial for the scattering off Ag, especially for low initial energies. It seems to be connected with an approximately comparable corrugation for both directions. Thus the process of vibrational excitation of the molecule results from the collisions of the molecular constituents with the target atoms.

Supposing that the collisions occur independently for the molecular constituents with the energy $E_i/2$, the energy of each atom after the next collision will be proportional to E_i. Therefore, their relative energy determining the vibrational excitation of the molecule must also be proportional to E_i. The dependence $T_v \sim E_0$ is actually seen clearly for the 'random' directions for both Ag and Pt targets. The non-linear behavior of the temperature with increasing E_0 for the channel-direction might be due to the ad-

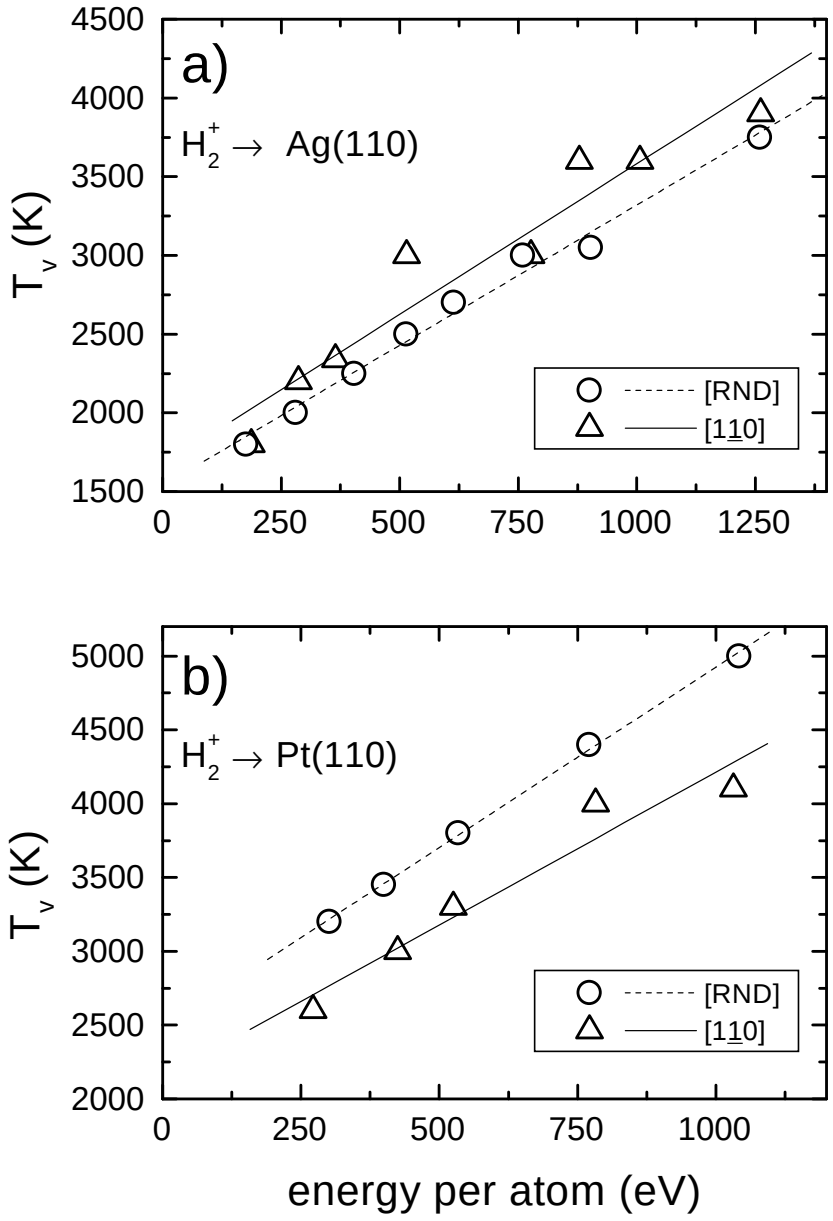

Figure 5.14: The dependence of the vibrational temperature T_v on initial molecule energy for H_2^+ scattered off Ag(110) (a) and Pt(110) (b). The lines are linear function fits to the results for the high-indexed (◯) and the [1$\bar{1}$0]-direction (△).

ditional contribution of rotational excitation and the growing influence of the softening of the intramolecular binding forces, caused by the metal electrons, to the dissociation of H_2^+ molecules. In that case, the function $f(\varepsilon)$ may differ from Eq. 5.3.

The calculations show that the observed form of the high energy tails of the spectra of H atoms scattered from Pt and Ag under H_2^+-bombardment can be described quite

naturally, supposing the resonant neutralization process to be the main mechanism leading to dissociation of the molecules.

Summary

In this work, the interaction of simple molecular ions, namely H_2^+ and N_2^+, with metal surfaces is studied under grazing scattering. The main attention is drawn towards the dissociation probability as a function of the projectile kinetic energy and the angular scattering geometry. The azimuthal orientation of the surface with respect to the direction of the beam incidence as well as the total scattering angle are important parameters for the survival probabilities of the molecules.

For the first time, an analytic function is used to describe the energy distribution of the scattering products and in particular to separate fragments from surviving molecules. The spectral shape can be accurately described that way and leads to atomic and molecular contributions which are discussed in detail and compared to appropriate theoretical models.

Clear differences are found for the scattering of nitrogen and hydrogen when comparing the spectra and the appropriate molecular survival probabilities. These differences are due to the initial neutralization process which opens for hydrogen a very efficient channel for dissociation that is not accessible for nitrogen. In this neutralization process, almost exclusively the repulsive $H_2(b^3\Sigma_u^+)$ state is occupied via resonant electron capture, initiating the decay process. A recently developed model is discussed in which a subsequent Auger de-excitation stops the dissociation process via triplet to singlet conversion into the stable ground state of the molecule. This model is able to explain the dissociative behavior observed in the experiments.

An analysis of the high energy tails of the energy distributions of the scattered hydrogen molecule constituents confirms the predominance of the dissociative neutralization process for this system. The values of vibrational temperatures of the molecules at the moment of dissociation, as derived from these high energy tails, are connected with the degree of vibrational excitation of the molecules as well as with the different probabilities of the dissociative neutralization at different surfaces. Since the resonant process

takes place early in the incoming part of the scattering trajectory, the rovibrational excitations due to mechanical interaction with surface atoms as well as the contributions of dynamic screening through metal electrons are still low at this stage. Nevertheless, these processes constitute a second hurdle for molecules which survive the neutralization process. For increasing energies, these 'mechanical' processes become more and more important.

In case of nitrogen, for which the neutralization does not provide a channel contributing to the dissociation of the molecule, the results are compared to classical trajectory calculations. A purely classical description however does not achieve satisfying agreement to experimentally obtained fragmentation yields. Obviously, the screening of the mutually bound molecular constituents that is induced by the presence of the conduction band electrons of the metal plays a sizeable role for the dissociation process.

Therefore, the underlying model in the molecular dynamics calculations is extended by an appropriate N-N bond weakening, implemented as an explicit z-dependence of the regular N-N potential. Even a static model – independent of the projectile velocity v_{proj} – leads to an obvious improvement. Within the model, the parameter D_{soft} reflects the bond dissolution and is determined by comparing experiment and simulation. From the comparison, one can conclude that screening plays a crucial role in the dissociative scattering of N_2 from metal surfaces, although not in a dynamical way. For this system, a rather static screening is observed. However, the elastic interaction of the molecular constituents with surface atoms acts as a 'trigger' for the fragmentation, since a higher amount of rotational excitation and hence more dissociation arises from low-index scattering in comparison to impact along high-indexed directions.

A further interesting result from this study is the identification of a new class of fragments overlapping energetically with the spectrum of scattered intact molecules: under the conditions of axial surface channeling, a large number of molecules penetrate deep into the semichannels and experience an extraordinary influence of the screening prior to the elastic interaction. This leads to 'soft dissociation' with minimal kinetic energy release, as confirmed by the calculations. In the energy spectra, these particles form a sharp peak which is very similar to the molecular one.

With regard to the obtained findings, it would be interesting to extend the investigations in case of hydrogen to appropriate molecular dynamics simulations. In addition to the model which is used in this work for the scattering of nitrogen, this task requires further theoretical and experimental input for a quantitative consideration of the involved charge exchange effects. A theoretical model predicting the corresponding transition rates could be cross-checked e.g. by scattering experiments using neutral H_2 projectiles [32] in the energy range $E_0 \lesssim 500$ eV. Even more access to the quantitative importance of the respective competing charge transfer processes could be gained as well from

experiments with magnetic surfaces. In contrast to the unmagnetized target, the initial resonant neutralization then leads to a spin-polarization of the dissociative triplet state in such a way that the subsequent Auger de-excitation process (Eq. 1.7) should be inhibited. Consequently, one would expect to observe corresponding changes in the molecular yield.

Bibliography

[1] J. T. Hogan and J. F. Clarke, J. Nucl. Mater. **53**, 1 (1974).

[2] A. Amirav, Comments At. Mol. Phys. **24**, 187 (1990).

[3] W. Heiland, in *Low Energy Ion-Surface Interactions*, edited by J. W. Rabalais (Wiley, New York, 1994), p. 313.

[4] I. S. Bitensky and E. S. Parilis, Nucl. Instrum. Methods Phys. Res. B **2**, 364 (1984).

[5] H. Akazawa and Y. Murata, Surf. Sci. **107**, L971 (1989).

[6] T. Schlathölter, T. Schlathölter, M. Vicanek, and W. Heiland, Surf. Sci. **352–354**, 195 (1996).

[7] C. S. Sass and J. W. Rabalais, J. Chem. Phys. **89**, 3870 (1988).

[8] A. Gross, S. Wilke, and M. Scheffler, Phys. Rev. Lett. **75**, 2718 (1995).

[9] M. Beutl, M. Riedler, and K. D. Rendulic, Chem. Phys. Lett. **247**, 249 (1995).

[10] U. Heinzmann, S. Holloway, A. W. Kleyn, R. E. Palmer, and K. J. Snowdon, J. Phys.: Condens. Matter **8**, 3245 (1996).

[11] T. Schlathölter, T. Schlathölter, M. Vicanek, and W. Heiland, J. Chem. Phys. **106**, 4723 (1997).

[12] K. Brüning, Master's thesis, Universität Osnabrück, Germany, 1996.

[13] K. Brüning, J. Granow, M. Reiniger, W. Heiland, M. Vicanek, and T. Schlathölter, Surf. Sci. **402–404**, 215 (1998).

[14] I. A. Wojciechowski, M. V. Medvedeva, V. K. Ferleger, K. Brüning, and W. Heiland, Nucl. Instrum. Methods Phys. Res. B **143**, 473 (1998).

[15] U. Imke, J. H. Rechtien, and P. H. F. Reijnen, Surf. Sci. **221**, 454 (1989).

[16] T. Schlathölter, Ph.D. thesis, Universität Osnabrück, Germany, 1996.

[17] W. Tappe, A. Niehof, K. Schmidt, and W. Heiland, Europhys. Lett. **15**, 406 (1991).

[18] K. Schmidt, T. Schlathölter, A. Närmann, and W. Heiland, Chem. Phys. Lett. **200**, 465 (1992).

[19] J. K. Nørskov, Phys. Rev. B **20**, 446 (1979).

[20] W. Heiland and E. Taglauer, Nucl. Instrum. Methods Phys. Res. B **132**, 535 (1976).

[21] R. J. MacDonald, W. Heiland, and E. Taglauer, Appl. Phys. Lett. **33**, 576 (1978).

[22] W. Heiland and E. Taglauer, in *Methods in Experimental Physics*, edited by R. L. Park and M. G. Lagally (Academic Press, New York, 1985), p. 299.

[23] P. J. Schneider, W. Eckstein, and H. Verbeek, Nucl. Instrum. Methods Phys. Res. B **218**, 713 (1983).

[24] T. Hashimoto, J. Murakami, and I. Kusunoki, Surf. Sci. **319**, 353 (1994).

[25] L. Pedemonte, R. Tatarek, M. Aschoff, K. Brüning, and W. Heiland, Nucl. Instrum. Methods Phys. Res. B **164–165**, 645 (2000).

[26] K. Schmidt, Master's thesis, Universität Osnabrück, Germany, 1989.

[27] C. Höfner, Ph.D. thesis, Universität Osnabrück, Germany, 1995.

[28] I. S. Bitensky and E. S. Parilis, Surf. Sci. **161**, L565 (1985).

[29] U. Imke, K. J. Snowdon, and W. Heiland, Phys. Rev. B **34**, 48 (1986).

[30] S. Schubert, Master's thesis, Universität Osnabrück, Germany, 1986.

[31] J. Los and J. J. C. Geerlings, Phys. Rep. **190**, 133 (1990).

[32] K. Schmidt, Ph.D. thesis, Universität Osnabrück, Germany, 1993.

[33] J. W. Gadzuk, Surf. Sci. **6**, 133 (1967).

[34] A. G. Borisov, D. Teillet-Billy, and J. P. Gauyacq, Phys. Rev. Lett. **68**, 2842 (1992).

[35] A. G. Borisov and U. Wille, Surf. Sci. **338**, L875 (1995).

[36] U. Imke, K. J. Snowdon, and W. Heiland, Phys. Rev. B **34**, 41 (1986).

[37] R. Harder, Ph.D. thesis, Universität Osnabrück, Germany, 1995.

[38] J. N. M. V. Wunnik, J. J. C. Geerlings, and J. Los, Surf. Sci. **131**, 1 (1983).

[39] H. Müller, R. Hausmann, H. Brenten, and V. Kempter, Surf. Sci. **284**, 129 (1993).

[40] H. Müller, R. Hausmann, H. Brenten, and V. Kempter, Surf. Sci. **303**, 56 (1994).

[41] N. Lorente, D. Teillet-Billy, and J. P. Gauyacq, Surf. Sci. **402–404**, 197 (1998).

[42] N. Lorente, D. Teillet-Billy, and J. P. Gauyacq (unpublished).

[43] K. Schmidt, H. Franke, T. Schlathölter, C. Höfner, A. Närmann, and W. Heiland, Surf. Sci. **301**, 326 (1994).

[44] N. Lorente, D. Teillet-Billy, and J. P. Gauyacq, Nucl. Instrum. Methods Phys. Res. B **157**, 1 (1999).

[45] R. Hemmen and H. Conrad, Phys. Rev. Lett. **67**, 1314 (1991).

[46] A. G. Borisov, D. Teillet-Billy, and J. P.Gauyacq, Surf. Sci. **325**, 323 (1995).

[47] T. E. Sharp, At. Data **2**, 119 (1971).

[48] M. Kato and Y. H. Ohtsuki, Phys. Stat. Sol. B **133**, 267 (1986).

[49] M. Kato, J. Phys. Soc. Jpn. **55**, 1011 (1986).

[50] M. Peñalba, A. Arnau, P. M. Echenique, F. Flores, and R. H. Ritchie, Europhys. Let. **19**, 45 (1992).

[51] S. Hausmann, Master's thesis, Universität Osnabrück, Germany, 1995.

[52] A. Närmann, *Fundamental Aspects of the Interaction of Particles with Matter* (Habilitation, Universität Osnabrück, Germany, 1995).

[53] C. Höfner, A. Närmann, and W. Heiland, Nucl. Instrum. Methods Phys. Res. B **72**, 227 (1992).

[54] A. Närmann, Ph.D. thesis, Universität Osnabrück, Germany, 1989.

[55] C. Höfner, Master's thesis, Universität Osnabrück, Germany, 1990.

[56] L. H. Thomas, Proc. Cambridge Philos. Soc. **23**, 73 (1928).

[57] E. Fermi, Zeitsch. f. Physik **48**, 73 (1929).

[58] J. F. Ziegler, J. P. Biersack, and U. Littmark, in *Stopping powers and ranges of ions in matter*, edited by J. F. Ziegler (Pergamon Press, New York, 1985), p. 1.

[59] K. P. Huber and G. Herzberg, *Molecular Spectra and Molecular Structure: IV. Constants of Diatomic Molecules* (Van Nostrand-Reinhold, New York, 1979).

[60] N. E. Henriksen, G. D. Billing, and F. Y. Hansen, Surf. Sci. **227**, 224 (1990).

[61] M. Asscher, O. M. Becker, G. Haase, and R. Kosloff, Surf. Sci. **206**, L880 (1988).

[62] G. Haase, M. Asscher, and R. Kosloff, J. Chem. Phys. **90**, 3346 (1989).

[63] O. B. Christensen, P. D. Ditlevsen, K. W. Jacobsen, P. Stoltze, O. H. Nielsen, and J. K. Nørskov, Phys. Rev. B **40**, 1993 (1989).

[64] P. M. Echenique, F. Flores, and R. H. Ritchie, Nucl. Instrum. Methods Phys. Res. B **33**, 91 (1988).

[65] P. M. Echenique, I. Nagy, and A. Arnau, Int. J. Quantum Chem. **23**, 521 (1989).

[66] A. Närmann, H. Franke, K. Schmidt, A. Arnau, and W. Heiland, Nucl. Instrum. Methods Phys. Res. B **69**, 158 (1992).

[67] H. P. Bonzel and R. Ku, J. Vac. Sci. Technol. **9**, 663 (1972).

[68] A. Niehof, A. Närmann, W. Hetterich, and W. Heiland, in *Proc. Symp. Surf. Sci.*, edited by M. Alnot, J. J. Ehrhardt, C. Launois, B. Mutaftschiev, and M. R. Tempére (P. Varga, Institut f. Allgemeine Physik, TU Wien, Obertraun, 1991), p. 245.

[69] A. Niehof, A. Närmann, W. Hetterich, and W. Heiland, in *Proc. of the National Conference "Ion-Surface Interaction"* (Yu. A. Ryzhov, Moscow, 1991).

[70] M. Vicanek, T. Schlathölter, and W. Heiland, Nucl. Instrum. Methods Phys. Res. B **115**, 206 (1996).

[71] C. Kittel, *Introduction to solid state physics* (John Wiley and Sons, New York, 1986).

[72] K. Wandelt, J. Vac. Sci. Techn. **2**, 802 (1984).

[73] V. L. Moruzzi, J. F. Janak, and A. R. Williams, *Calculated Electronic Properties of Metals* (Pergamon Press, New York, 1978).

[74] A. Robin, Master's thesis, Universität Osnabrück, Germany, 1999.

[75] B. Willerding, H. Steininger, K. J. Snowdon, and W. Heiland, Nucl. Instrum. Methods Phys. Res. B **2**, 453 (1984).

[76] B. Willerding, Ph.D. thesis, Universität Osnabrück, Germany, 1984.

[77] C. N. Burrous, A. J. Lieber, and V. T. Zaviantseff, Rev. Sci. Instr. **38**, 1477 (1967).

[78] E. W. Kuipers and A. L. Boers, Nucl. Instrum. Methods Phys. Res. B **29**, 567 (1987).

[79] T. Schlathölter, Master's thesis, Universität Osnabrück, Germany, 1993.

[80] C. J. Davisson and L. H. Germer, Phys. Rev. **30**, 705 (1927).

[81] J. B. Pendry, *Low energy electron diffraction* (Academic Press, London, 1974).

[82] M. A. V. Hove, W. H. Weinberg, and C. M. Chan, *Low-Energy Electron Diffraction* (Springer Verlag, Berlin, 1986).

[83] R. Sizmann and C. Varelas, Festkörperprobleme **XVII**, 261 (1977).

[84] W. Heiland, T. Schlathölter, and M. Vicanek, Phys. Stat. Sol. (b) **192**, 301 (1995).

[85] A. Niehof and W. Heiland, Nucl. Instrum. Methods Phys. Res. B **48**, 306 (1990).

[86] M. Schleberger, Ph.D. thesis, Universität Osnabrück, Germany, 1993.

[87] M. Schleberger, S. Speller, C. Höfner, and W. Heiland, Nucl. Instrum. Methods Phys. Res. B **90**, 274 (1994).

[88] A. Närmann, H. Derks, W. Heiland, R. Monreal, E. Goldberg, and F. Flores, Surf. Sci. **217**, 255 (1989).

[89] A. Närmann, R. Monreal, P. M. Echenique, F. Flores, W. Heiland, and S. Schubert, Phys. Rev. Lett. **64**, 1601 (1990).

[90] A. Närmann, K. Schmidt, W. Heiland, R. Monreal, F. Flores, and P. M. Echenique, Nucl. Instrum. Methods Phys. Res. B **48**, 378 (1990).

[91] *PeakFit* (Jandel Scientific Software, AISN Software Inc., San Rafael, CA).

[92] V. S. Remizovich, M. I. Ryazanov, and I. S. Tilinin, Sov. Phys. JETP **79**, 448 (1980).

[93] T. Schlathölter and W. Heiland, Surf. Sci. **323**, 207 (1995).

[94] J. Granow, Master's thesis, Universität Osnabrück, Germany, 1997.

[95] K. Sekar, J. Scheer, K. Brüning, I. A. Wojciechowski, and V. K. Ferleger, Phys. Rev. B (submitted).

[96] T. Fröhlich, Master's thesis, University of Berne, Switzerland, 1999.

[97] J. Scheer, K. Brüning, T. Fröhlich, P. Wurz, and W. Heiland, Nucl. Instrum. Methods Phys. Res. B **157**, 208 (1999).

[98] J. Scheer, Master's thesis, Universität Osnabrück, Germany, 1999.

[99] M. Wieser, Master's thesis, University of Berne, Switzerland, 2001.

[100] J. P. Biersack and L. G. Haggmark, Nucl. Instrum. and Meth. **174**, 257 (1980).

[101] M. T. Robinson and I. M. Torrens, Phys. Rev. B **9**, 5008 (1974).

[102] D. P. Jackson, Surf. Sci. **43**, 431 (1974).

[103] A. Rahman, Phys. Rev. **138**, 405 (1964).

[104] L. Verlet, Phys. Rev. **159**, 98 (1967).

[105] D. Beeman, J. Comp. Phys. **20**, 130 (1976).

[106] S. Valkealahti and R. M. Nieminen, Nucl. Instrum. Methods Phys. Res. B **18**, 365 (1987).

[107] J. E. Lennard-Jones, Trans. Faraday. Soc. **28**, 333 (1932).

[108] G. Wedler, *Adsorption* (Verlag Chemie, Weinheim/Bergstrasse, 1970).

[109] *DMol* (Biosym Technologies, San Diego, CA).

[110] T. N. Rhodin and G. Ertl, *The nature of the surface chemical bond* (North–Holland, Amsterdam, 1979).

[111] W. T. Lee, L. Ford, P. Blowers, H. L. Nigg, and R. I. Masel, Surf. Sci. **416**, 141 (1998).

[112] P. Hohenberg and W. Kohn, Phys. Rev. **136**, 864 (1964).

[113] T. Brunner and W. Brenig, Surf. Sci. **261**, 284 (1992).

[114] R. A. Shigeishi and D. A. King, Surf. Sci. **62**, 379 (1977).

[115] T. Schlathölter, H. Franke, M. Vicanek, and W. Heiland, Surf. Sci. **363**, 79 (1996).

[116] B. Willerding, W. Heiland, and K. J. Snowdon, Phys. Rev. Lett. **53**, 2031 (1984).

[117] J. M. Schins, R. B. Vrijen, W. J. van der Zande, and J. Los, Surf. Sci. **280**, 145 (1993).

[118] I. S. Bitensky, Y. S. Gilenko, and E. S. Parilis, Sov. Phys. JETP **67**, 470 (1988).

[119] I. S. Bitensky, E. S. Parilis, and I. A. Wojciechowski, Nucl. Instrum. Methods Phys. Res. B **67**, 359 (1992).

[120] L. D. Landau and E. M. Lifshits, *Statistical physics* (Pergamon Press, Oxford, 1958), Vol. 5.

[121] S. Hausmann, C. Höfner, T. Schlathölter, H. Franke, A. Närmann, and W. Heiland, Nucl. Instrum. Methods Phys. Res. B **115**, 31 (1996).

[122] C. Höfner, A. Närmann, and W. Heiland, Nucl. Instrum. Methods Phys. Res. B **93**, 113 (1994).

[123] B. E. Baklitzky and I. S. Bitensky, Nucl. Instrum. Methods Phys. Res. B **83**, 462 (1993).

[124] I. A. Wojciechowski, M. V. Medvedeva, V. K. Ferleger, K. Brüning, and W. Heiland, Nucl. Instrum. Methods Phys. Res. B **164–165**, 626 (2000).

[125] M. Vicanek, T. Schlathölter, and W. Heiland, Nucl. Instrum. Methods Phys. Res. B **125**, 194 (1997).

[126] I. S. Bitensky, V. K. Ferleger, and I. A. Wojciechowski, Nucl. Instrum. Methods Phys. Res. B **125**, 201 (1997).

Danksagung

Diese Arbeit entstand in der Arbeitsgruppe der Oberflächenphysik an der Universität Osnabrück. Ich möchte mich hier bei all denen, die mich dabei in jeglicher Weise unterstützt haben, ganz herzlich bedanken. Dies sind insbesondere:

Prof. Dr. Werner Heiland, der mir diese Arbeit überhaupt erst ermöglichte und mir bei fachlichen und organisatorischen Fragen stets weiterhalf.
Jürgen Guth, ohne dessen handwerkliche Fähigkeiten und Hilfsbereitschaft nicht nur in dieser Arbeit ein großer Teil der Experimente erschwert oder gar undurchführbar gewesen wäre.
Dr. Thomas Schlathölter und Priv. Doz. Dr. Andreas Närmann, die mir sowohl über kleine als auch große Distanzen stets kompetente Antworten auf unzählige Fragen gaben und darüberhinaus auch mit wichtigen Ideen und Denkanstößen zur Arbeit beitrugen.
Priv. Doz. Dr. Marika Schleberger und Dr. Sylvia Speller, die ebenfalls für Fragen jeglicher Art offen waren und insbesondere bei der Literaturrecherche und bei Problemen mit TEX eine große Hilfe waren.
Unsere usbekischen Projektpartner, Prof. Dr. Vladimir Ferleger, Dr. Igor Wojciechowski und Dr. Marina Medvedeva, die zu einem großen Teil zu den theoretischen Überlegungen dieser Arbeit beitrugen und nicht zuletzt auch die 'high energy tail'-Rechnungen durchgeführt haben. Außerdem möchte ich mich für die vorzügliche Gastfreundschaft im fernen orientalischen Tashkent, insbesondere auch bei Boris Krakov, bedanken.
Dr. Philippe Roncin, der mir gleichermaßen mit Gastfreundschaft am LCAM in Orsay einen interessanten Einblick in die Oberflächenphysik ermöglichte.
Dr. Thorsten Schlathölter, der mir geduldsam die Applikation DMol erklärte und Dr. Martin Vicanek, der in Verbindung mit ScaDiM aushalf.
Nicht unerwähnt bleiben dürfen die Mitarbeiter des Rechenzentrums, insbesondere Herr Werner Nienhüser, und die Mitarbeiter der Elektronik- und Feinmechanik-Werkstätten.
Dr. Laura Pedemonte, Dr. K. Sekar, Dr. Norbert Hatke, Dipl. Phys. Abel Robin, Dipl. Phys. Jürgen Scheer und Jens Granow für die diskussionsreiche und angenehme Zusammenarbeit in Labor und Büro, sowie der Rest der Arbeitsgruppe.

Publication List

- K. Brüning, J. Granow, M. Reiniger, W. Heiland, M. Vicanek, and T. Schlathölter. Dissociation of fast N_2 molecules at a Pd(110) surface. *Surf. Sci.* **402–404** 215–218 (1998)
- K. Brüning, J. Granow, T. Schlathölter, and W. Heiland. Surface channeling and dissociation of small molecules. *Proceedings of 3S'98 (Symposium of Surface Science), Park City, Utah, USA* Th8–Th9 (1998)
- I. A. Wojciechowski, M. V. Medvedeva, V. Kh. Ferleger, M. Vicanek, K. Brüning, and W. Heiland. Electronic processes in molecule-surface scattering. *Nucl. Instr. Meth. B* **140** 265–272 (1998)
- W. Heiland, K. Brüning, and M. Aschoff. Surface analysis using low energy ion beams. *Proceedings of the 8th International Workshop on Ion Beam Surface Diagnostics), Uzhgorod, Ukraine* 5–8 (1998)
- I. A. Wojciechowski, M. V. Medvedeva, V. Kh. Ferleger, K. Brüning, and W. Heiland. The broadening of energy spectra of atoms scattered by a solid surface under molecular ion bombardment. *Nucl. Instr. Meth. B* **143** 473–478 (1998)
- P. Wurz, T. Fröhlich, K. Brüning, J. Scheer, W. Heiland, E. Herzberg, and S. Fuselier. Formation of negative ions by scattering from a diamond (111) surface. *Proc. Week of Postdoc. Students 1998), Charles University Prague, Czech Republic* 257–262 (1998)
- J. Scheer, K. Brüning, T. Fröhlich, P. Wurz, and W. Heiland. Scattering of small molecules from a diamond surface. *Nucl. Instr. Meth. B* **157** 208–213 (1999)
- I. A. Wojciechowski, M. V. Medvedeva, V. Kh. Ferleger, K. Brüning, and W. Heiland. Dissociative grazing scattering of H_2^+ on metal surfaces: Analysis of the high-energy parts of the spectra of the scattered molecule constituents. *Nucl. Instr. Meth. B* **164–165** 626–632 (2000)
- L. Pedemonte, R. Tatarek, M. Aschoff, K. Brüning, and W. Heiland. Surface structure and dynamics of the Ag(110) surface studied by low energy ion scattering. *Nucl. Instr. Meth. B* **164–165** 645–649 (2000)
- S. Jans, P. Wurz, R. Schletti, K. Brüning, K. Sekar, W. Heiland, J. Quinn, and R. E. Leuchtner. Scattering of atoms and molecules off a barium zirconate surface. *Submitted to Nucl. Instr. Meth. B* (2000)
- K. Sekar, J. Scheer, K. Brüning and W. Heiland. Interaction of molecular hydrogen with LiF(110) surfaces. *Submitted to Phys. Rev. B*
- K. Brüning, W. Heiland, T. Schlathölter, I. A. Wojciechowski, M. V. Medvedeva, and V. Kh. Ferleger. Dissociation of fast N_2 molecules scattered from different fcc(110)-surfaces. *J. Chem. Phys.* **113** (6) 2456-2469 (2000)

Erklärung

gemäß §3 Abs. 2a der Promotionsordnung:

Hiermit erkläre ich, dass ich diese Arbeit selbständig erstellt und nur die angegebenen Quellen und Hilfsmittel verwandt habe.

Osnabrück, im Juni 2000 Karsten Brüning